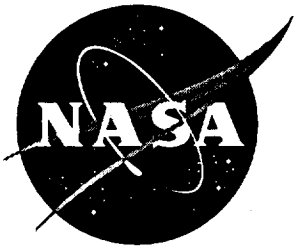NASA Technical Memorandum 110279

Comparison of System Identification Techniques for the Hydraulic Manipulator Test Bed (HMTB)

A. Terry Morris

Langley Research Center, Hampton, Virginia

September 1996

Table of Contents

ii

List of Tables

List of Figures

Symbols and Acronyms

Symbols

$C_{xy}(\tau)$	covariance function
ξ	damping ratio
$\mathcal{E}(k)$	residuals (equation errors)
$e(t)$	white noise
$E[\ ]$	expectation operator
f	frequency
$G(q), H(z)$	transfer function
$H(k)$	Hankel matrix
$H(q)$	disturbance dynamics
K	Kalman filter gain
μ	mean
θ	parameter vector
ϕ	phase
$R_u(n)$	autocorrelation matrix
$R_{xy}(\tau)$	cross-correlation function
$\Phi(w)$	spectral density function
$u(t)$	input signal
$v(k)$	input vector
$v(t)$	disturbances
$V(\theta)$	loss function
w	radian frequency
$w(t)$	simulated white noise process
$x(k)$	state vector
$\hat{x}(k)$	estimate of state vector
$\hat{y}(k)$	estimated measurement
$y(t)$	measured output
$\hat{y}(t)$	predicted output
Y	system Markov parameters
$\overline{Y}$	observer Markov parameters

Acronyms

AFD	Aft Flight Deck
ARMAX	Autoregressive Moving Average with Exogenous Variables
ARX	Autoregressive with Exogenous Variables
BRP	Bipolar Ramping Pulse
BW	Bandwidth
CSA	Canadian Space Agency
DOF	Degree of Freedom
DOSS	Dexterous Orbital Servicing System
ERA	Eigensystem Realization Algorithm
ESA	European Space Agency

ESD	Emergency Shutdown
EVA	Extravehicular Activity
FFT	Fast Fourier Transform
FTS	Flight Telerobotic Servicer
GND	Ground
HC	Hand Controller
HMTB	Hydraulic Manipulator Test Bed
IBM	International Business Machines
IV4	Four Stage Instrument Variable
JEM	Japanese Experiment Module
LaRC	Langley Research Center
LSE	Least Squares Estimate
MEM	Maximum Entropy Method
MIMO	Multi-Input, Multi-Output
MIO	Multi Input/Output
MMAG	Martin Marietta Astronautics Group
MPESS	Multi-purpose Experiment Support Structure
MSS	Mobile Servicing System
NASA	National Aeronautics and Space Administration
OE	Output Error
OKID	Observer/Kalman Filter Identification
ORU	Orbital Replacement Unit
PC	Personal Computer
PE	Persistently Exciting
PEM	Prediction Error Method
PRBS	Pseudorandom Binary Sequence
PSD	Power Spectral Density
RPCM	Remote Power Controller Module
SISO	Single-Input, Single-Output
SOCIT	System/Observer/Controller Identification Toolbox
SPDM	Special Purpose Dexterous Manipulator
SSF	Space Station Freedom
SSRMS	Space Station Remote Manipulator System
STS	Space Transportation System
SysID	System Identification
WSM	Western Space and Marine

I. Introduction

The main objective of this thesis is to identify dynamical models of the Hydraulic Manipulator Test Bed (HMTB). In particular, system identification techniques will be used to identify the joint dynamics and to validate the correctness of the HMTB models. Though dynamic model verification has been studied and performed for the DOSS flight manipulator, dynamic system identification for the hydraulic kinematically-equivalent ground-based DOSS manipulator located in the hydraulic manipulator test bed (HMTB) facility at the NASA Langley Research Center has not been studied in detail. This thesis will describe, apply, and compare system identification techniques for three joints (shoulder yaw, shoulder pitch, and elbow pitch) of the seven DOF hydraulic manipulator for the purpose of obtaining an adequate dynamic model of HMTB during insertion of the remote power controller module ORU.

To perform the identification, a series of single-input, single-output (SISO) and multi-input, multi-output (MIMO) experiments will be performed. Nonparametric and parametric identification techniques will be explored in order to develop representative models of the selected joints. The identified SISO model estimates will be validated. The best performing models will be used for a decoupled multivariable state-space model. It should be noted that each identified model represents an open-loop representation of the closed-loop implementation for each joint. It is not the purpose of this thesis to determine the effective inertia or the effective damping coefficients for the HMTB links. The manipulator is localized about a representative space station orbital replacement unit (ORU) exchange task allowing the use of linear system identification methods. The parametric models will be compared to determine the best dynamic model for performing the ORU task.

System identification techniques have been applied in many different fields. The purpose of the identified models in this thesis is to use them in a control application. The thesis concludes by proposing a model reference control system to aid in astronaut ground tests. This approach would allow the identified models to mimic on-orbit dynamic characteristics of the actual flight manipulator thus providing astronauts with realistic on-orbit responses to perform space station tasks in a ground-based environment.

The process of system identification starts by performing an identification experiment, that is, exciting the system using some sort of input signal and observing the output over a time interval [9]. Once the experimental data is recorded, parametric or nonparametric analysis can be performed. In nonparametric analysis, a system's transfer function, impulse response, or step response is extracted from the experimental data in order to determine transient or frequency response characteristics of the system. This method, however, is often sensitive to noise and usually does not give very accurate results [9]. In parametric analysis, the recorded input and output sequences are fitted to a parametric model. This process begins by determining an appropriate model form. Next, some statistically based method is used to estimate the unknown parameters of the model. The model is then tested or validated to determine if it appropriately represents the dynamic system.

The remainder of this chapter provides historical background of the DOSS manipulator, the Hydraulic Manipulator Test Bed (HMTB) housed at the NASA Langley

Research Center, and the orbital replacement unit hardware used by the manipulator. Most of this information has not been published before. The chapter concludes by providing a literature search on system identification techniques used in this thesis.

Chapter II will describe the overall experiment design process developed specifically for the hydraulic manipulator test bed (HMTB). As a precursor to parametric identification, Chapter III will describe the application of nonparametric methods used to extract characteristics of the unknown joints. Parametric model estimation techniques primarily used for control system identification will be applied in Chapter IV. In this technique, transfer function models describing each joint and its associated disturbances are analyzed to yield an adequate state-space model approximation. The second parametric technique, used primarily in modal system identification, will be employed in Chapter V. This technique uses a minimum realization algorithm to determine a model with the smallest state-space dimension among all realizable systems. Comparisons of the parametric models will be shown in Chapter VI. Chapter VII concludes the thesis by providing suggestions for future work. A model reference control system is proposed to provide astronauts with realistic on-orbit responses to perform space station tasks on the ground.

Matlab menu-driven system identification software programs were developed for this project. One of the programs, a menu-driven script written for nonparametric and parametric evaluation of the input/output data using functions from the *MATLAB System Identification Toolbox*. Another menu-driven program was used to identify models using the Observer/Kalman Filter Identification (OKID) technique, provided in the *System/Observer/Controller Identification Toolbox (SOCIT)*. This last program script used several toolboxes to perform MIMO comparisons for identified models.

1.   Dexterous Orbital Servicing System (DOSS) Background

In 1984 President Reagan directed the National Aeronautics and Space Administration (NASA) to build a space station. He invited allies of the United States to join in the challenge of creating a machine that could be manned and operated beyond the year 2000 [1]. Space Station Freedom shown in Figure 1 was the first major co-operative program of the governments of the U.S., Japan, the 10 nations of the European Space Agency (ESA), and Canada for the utilization and operation of a microgravity laboratory environment in space. Each government was responsible for furnishing specific user elements of Space Station Freedom. The United States through the direction of the National Aeronautics and Space Administration (NASA) was responsible for the design, development, and construction of the truss assembly infrastructure, the crew living quarters (US Habitat Module), and the US Laboratory Module. Japan would develop and assemble the Japanese Experiment Module (JEM). The European Space Agency (ESA) and its member states would develop their own Free-Flying Laboratory named Columbus and a polar platform. Canada's responsibility involved providing the Mobile Servicing System (MSS), a complex robotic machine used to assemble, service, and maintain most of the station. The MSS's major robotic components are the Space Station Remote Manipulator System (SSRMS) and the Special Purpose Dexterous Manipulator (SPDM) shown in Figure 2.
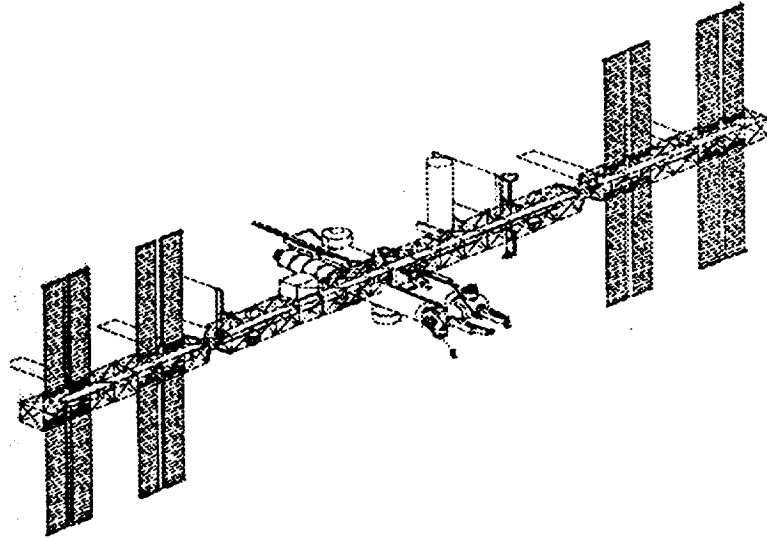
Figure 1. Space Station Freedom
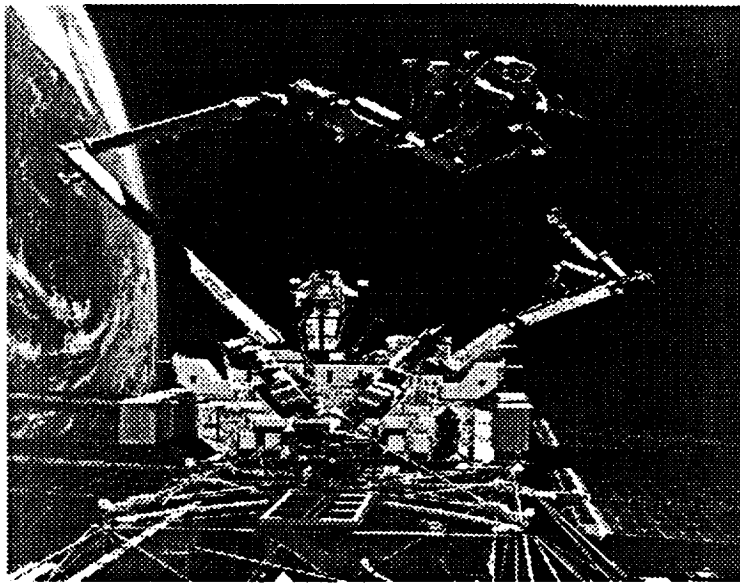
Figure 2. Canada's SSRMS and SPDM working on Freedom's truss.

The U.S. Congress also appropriated a portion of space station money for U.S. supported space station robotics [17]. With these funds, NASA started development of the Flight Telerobotic Servicer (FTS), a dexterous manipulator shown in Figure 3, for use on both the Space Transportation System (STS) and the space station. After determining the requirements for the space servicing manipulator, NASA awarded Martin Marietta Astronautics Group (MMAG) a contract to design, construct, and test a flight deliverable FTS system.

3
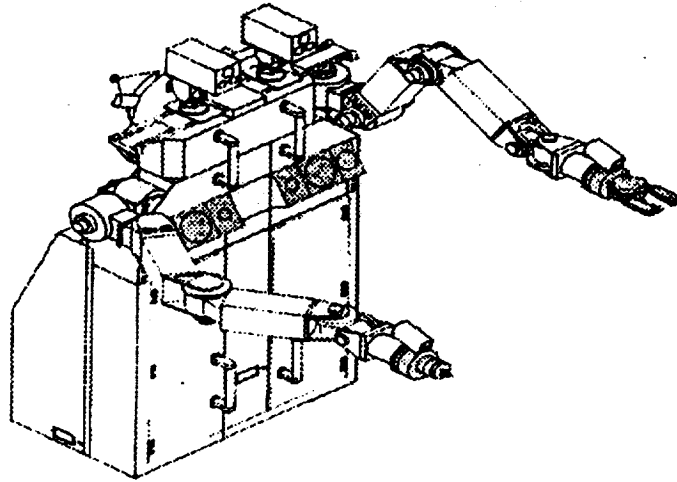
Figure 3. NASA's Flight Telerobotic Servicer (FTS).

When the Advisory Committee on the Future of the U.S. Space Program convened by Vice President Dan Quayle issued a report in December 1990, NASA's goals, programs and practices were altered [2]. The NASA program that suffered the most devastating blow was Space Station Freedom. The report recommended that Space Station Freedom be utterly recast, reduced in both scale and complexity, which was a decree previously urged by Congress [3]. Freedom's new primary mission was in the life sciences, specifically the psychological and physiological effects of microgravity on humans. In the space station redesign process, many services and capabilities were reduced while others were halted indefinitely such as NASA's Flight Telerobotic Servicer (FTS) project. With over 270 million dollars already invested in the development and fabrication of FTS robotic technologies, NASA initiated a project apart from the space station to capture the newly developed FTS technologies.

When Canadian politicians pushed to withdraw from the leaner, redesigned space station, NASA and the Canadian Space Agency (CSA) began talks in March 1994 to develop a plan which would reduce Canadian space station costs and bolster space science cooperation [4]. In the new plan, Canada would defer the Special Purpose Dexterous Manipulator (SPDM) which is a significant portion of Canada's robotic contribution to the space station. With SPDM, the space station's primary robotic resource, deferred, NASA decided to continue a stunted version of its robotic program using existing FTS technology to provide a robotic presence on the shuttle and the space station in the interim.

The new robotic thrust called the Dexterous Orbiter Servicing System was based on the previous FTS designed by Martin Marietta. Initially, the new system was to provide robotic capabilities to space shuttle astronauts. Mission specialists would utilize and test the system in the shuttle cargo bay as a precursor to space station related tasks and procedures. The project was later termed the Dexterous Orbital Servicing System (DOSS) to service both the space shuttle and the redesigned space station.

A ground based trainer system composed of a shuttle aft flight deck (AFD) mockup and one seven-degree-of-freedom hydraulic manipulator mounted on a multi-

purpose experiment support structure (MPESS) was designed as a form, fit, and functional laboratory version of the flight system [5]. The kinematically equivalent hydraulic manipulator was developed by Western Space and Marine (WSM). The ground based trainer system is referred to as the Hydraulic Manipulator Test Bed (HMTB).

2. Hydraulic Manipulator Test Bed (HMTB)

The DOSS trainer built by Western Space and Marine was first located at Martin Marietta and then transferred to NASA's Langley Research Center (LaRC). The trainer was placed in the Hydraulic Manipulator Test Bed (HMTB) facility shown in Figure 4. The HMTB facility includes a ground test dexterous manipulator driven by Ada flight prototype software and a shuttle aft flight deck (AFD) mockup.
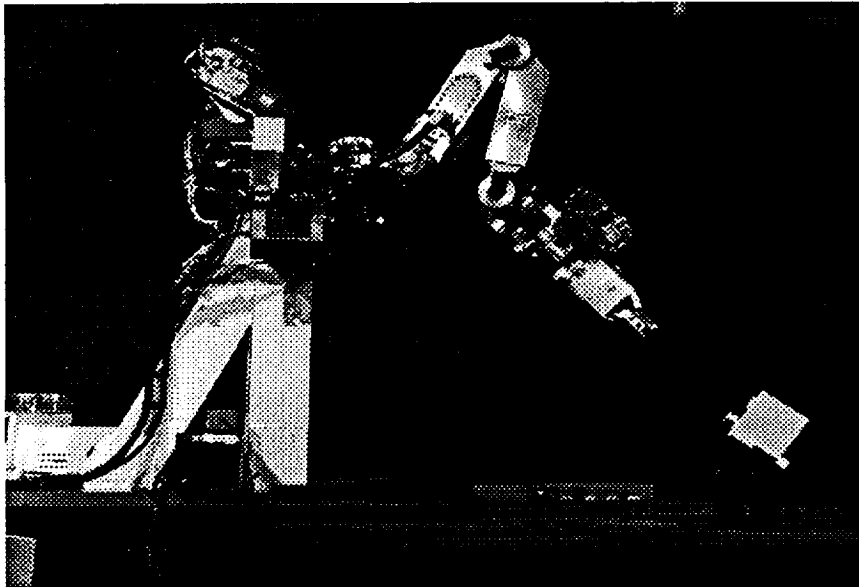
Figure 4. LaRC's Hydraulic Manipulator Test Bed (HMTB).

Specifications were developed to train the flight crew to operate the trainer system in accomplishing mission tasks, to operate in a 1-G environment, and to develop mission operation timelines. Layout of the trainer system in the HMTB facility, shown in Figure 5, was configured to provide the flight crew the same geometry, camera views, and lighting conditions that would exist during the actual flight for completion of space related tasks. Mission tasks include the installation and removal of space station truss members, the exchange of space station orbital replacement units (ORU), mating thermal utility connectors, and performing inspection tasks.

The trainer manipulator consists of seven hydraulic rack and pinion actuators and their controlling valves integrated with structure to provide a seven degree of freedom (DOF) hydraulic manipulator [6] as shown in Figure 6. The hydraulic manipulator provides the same kinematics as the flight manipulator, that is, six controllable degrees of freedom (shoulder yaw and pitch, wrist pitch, yaw and roll, and elbow pitch) with a single indexed roll DOF at the shoulder.
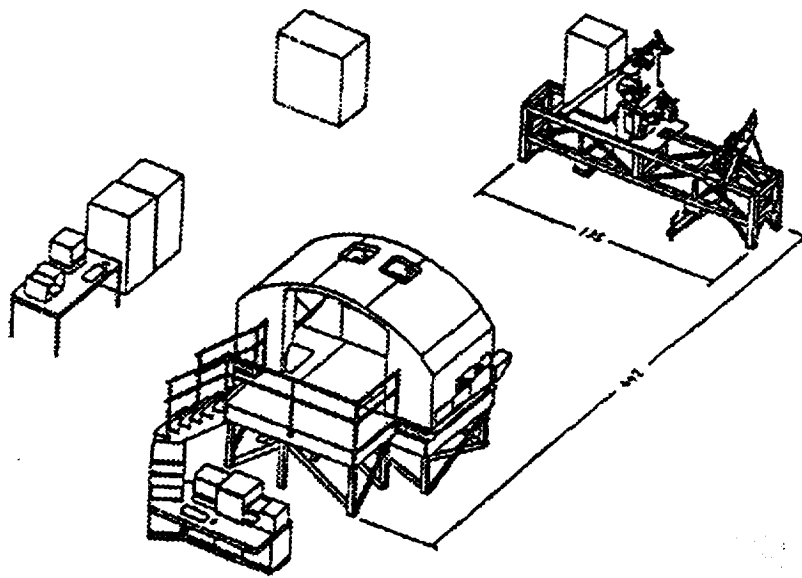
Figure 5. The Hydraulic Manipulator Test Bed Setup.
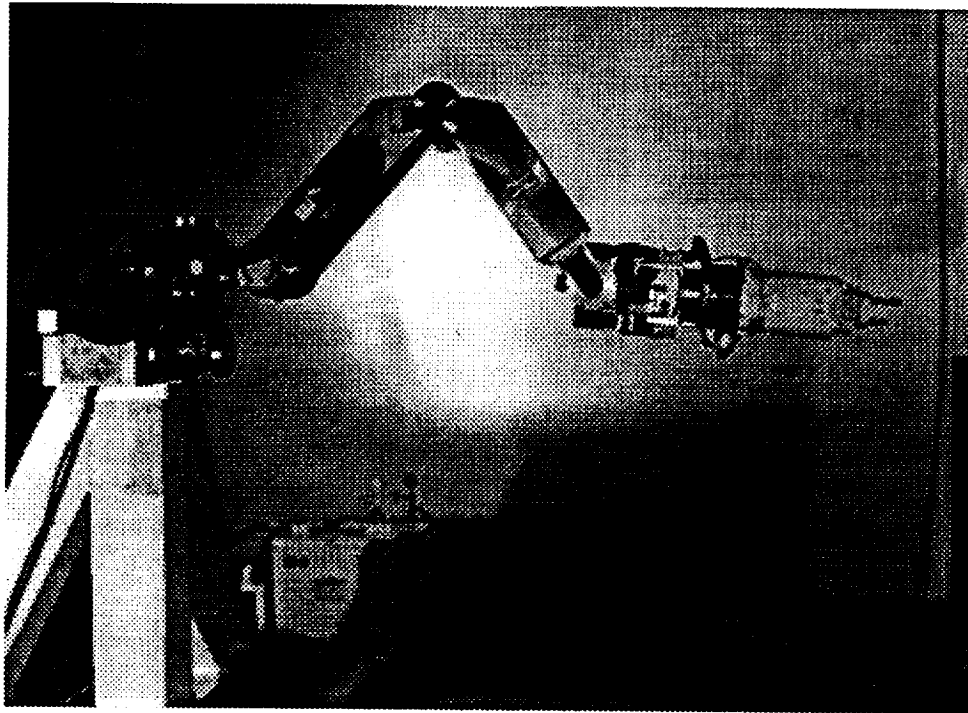
Figure 6. The HMTB Hydraulic Manipulator.

The aft flight deck (AFD) mockup, shown in Figure 8, is a replica of the actual AFD (depicted in Figure 7) and provides some of its functions. It provides the crew with an interface to control telerobot tasks and operations with or without a direct view of the worksite. Additional devices within the AFD mockup include a 2x3 DOF hand controller to teleoperate the trainer arm, closed circuit television monitors to display views of the hydraulic trainer, and an emergency shutdown (ESD) switch to turn off power to each arm servo while maintaining power to the trainer's control computer. Figure 8 displays an internal view of the AFD mockup.
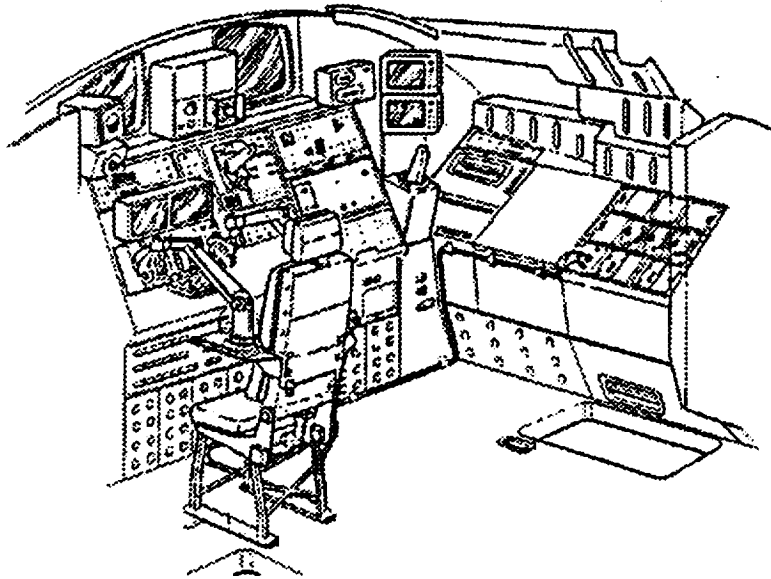
Figure 7. The Aft Flight Deck (AFD).
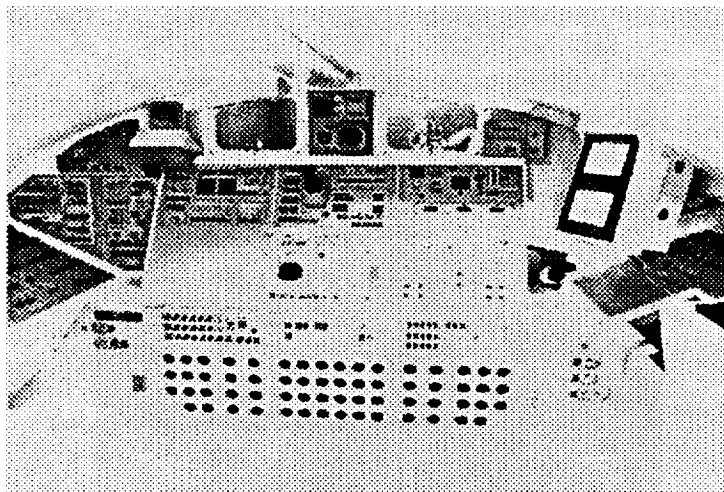
Figure 8. Internal View AFD mockup.

The trainer control station is comprised of a trainer control station computer, power control panels, a 1553B bus interface, and various other communication devices.

The trainer control station computer provides software for control of training, and setting up training conditions. The 1553B bus monitors commands and responses between the control computer, the joint controllers, and the 2x3 DOF hand controller.

According to FTS trainer specifications, the HMTB facility at NASA LaRC is an adequate, ground based version of the system to be used by shuttle flight crew members in accomplishing mission tasks. HMTB configuration provides the crew with the same geometry, similar camera views, identical manipulator kinematic configuration, the same software control, and lighting conditions that would exist during an actual space shuttle flight.

3. Remote Power Controller Module

One of the primary mission tasks on the space station will be the maintenance of orbital replacement units (ORUs). With approximately 70 remote power controller module (RPCM) ORUs located on various port and starboard clusters of the space station, extravehicular activities (EVA) performed by the space station crew members would be difficult, impractical, and potentially hazardous [7]. Robotic servicing of the RPCM by the DOSS system would minimize the EVA crew time and significantly increase crew safety.

There are six types of RPCMs each varying in power capacity while maintaining identical physical dimensions. Each RPCM, (mockup shown in Figure 9), is responsible for regulating and distributing secondary power to critical space station components. Therefore, replacement of failed RPCMs by a dexterous manipulator would provide a crucial space station maintenance service. Successful completion of an RPCM exchange procedure lies in the ability of the dexterous manipulator to extract the failed ORU, to exchange the failed ORU with a new one, and to carefully insert the new ORU. For the purpose of this thesis, data from the RPCM ORU exchange task will be used to validate different dynamical models for the HMTB joints.
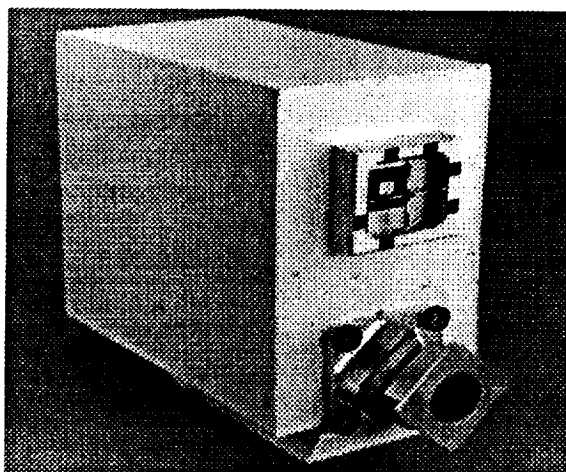
Figure 9. Remote Power Controller Module (RPCM) ORU Mockup.

8

4. System Identification Techniques

With a myriad of interrelated approaches, perspectives, methods, techniques and specializations, the field of system identification has widespread application in many areas such as communications, geophysical engineering, fault detection, pattern recognition, adaptive filtering, linear prediction, electric circuits and robotics. With this in mind, the literature search has been limited to system identification techniques for control purposes.

For thirty years system identification has been an important discipline within the area of controls. With modern control methods requiring specific accuracies for mathematical models, the system identification benefit of improving an analytical model is of noted significance. Two complementary aspects of system identification are frequency domain and time domain identification.

Frequency domain identification historically dominated system identification practice in control engineering prior to the 1960s [11]. Frequency domain identification emphasizing nonparametric identification methods has been used for stability, design and control purposes. In this thesis, transfer function, correlation, and spectral analysis techniques will be used for nonparametric identification of the HMTB joints.

Time domain approaches emphasize parametric identification techniques for the system identification problem. The last two decades have seen a tremendous increase in the use of parametric time domain identification methods. This has been partly due to stricter accuracy requirements for mathematical control models as well as the increased availability of digital computers that can estimate system characteristics much faster than conventional frequency domain methods. The first parametric identification technique employed in this thesis will use various black-box transfer function model structures to determine parametric model estimates for the HMTB joints [10]. The transfer function models, found within the *MATLAB System Identification Toolbox* by Lennart Ljung [10], use a prediction error method (PEM) to determine parameters for each black-box model. The PEM is a modification of the least squares (LS) method.

The field of structures has used parameter identification techniques based on system realization theory. One such technique, Observer/Kalman Filter identification (OKID), will also be used to identify parametric models for the HMTB joints. This minimum realization approach to time domain system identification yields a model with the smallest state space dimension among a set of models having the same input-output relationship. Ho and Kalman [12] both developed minimum realization theory using Markov parameters which are simply pulse response functions.

In this thesis, both frequency and time domain techniques will be used to extract and identify dynamic characteristics of the HMTB manipulator. The particular techniques used in this thesis will be discussed in more detail after the following chapter which will describe the experiment design process and setup.

9

II. Experiment Design

This chapter will describe the overall experiment design process developed specifically for the hydraulic manipulator test bed (HMTB) at the NASA Langley Research Center. The experiment design has been modularly configured and developed within physical hardware limitations and temporal constraints.

1. Overall Design Process

The steps of identifying dynamic models of the manipulator joints involve designing an experiment, selecting a model structure, choosing a criterion to fit, and devising a procedure to validate the chosen model. With the goal of obtaining a 'good and reliable' model estimate, Ljung [10] emphasizes the importance of the experiment design and the selection of its associated variables. Since a good model is not likely to be obtained from bad experiments, identification experiments should be selected to effectively characterize all the important modes of the system. This involves selecting persistently exciting (pe) input signals, that is, input signals which have strictly positive spectral density functions for all frequencies in the frequency band which is of interest for the intended application of the model.

Figure 10 displays a pictorial representation of the experiment design segments starting from the generation of excitation signals to the extraction of useful joint space data for system identification and parameter estimation. Several physical devices and software applications were used in the experiment design process. Generation of the various waveform signals was performed on an IBM compatible 486 personal computer (PC).

486	386		486

| Waveform Generation | Excitation Control | HMTB Manipulator | Data Conversion |
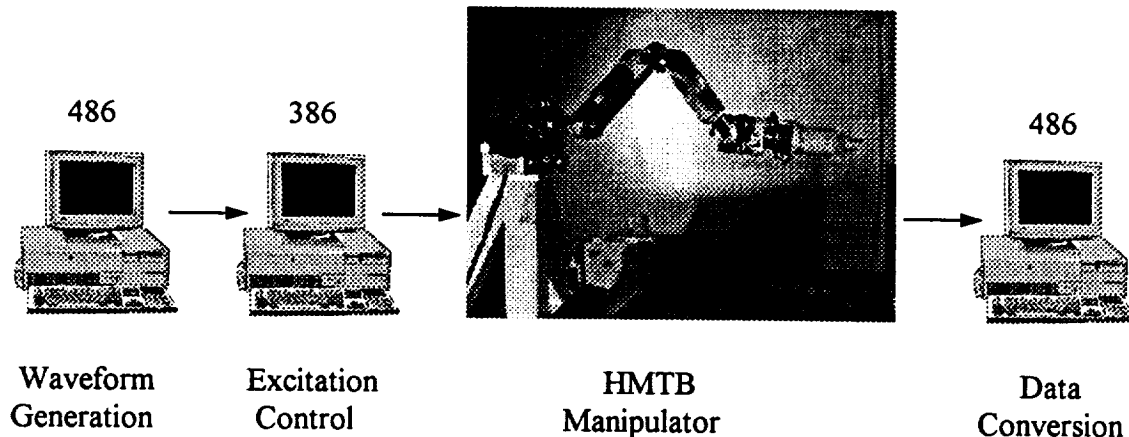
Figure 10. Overall Experiment Design.

A MATLAB waveform generation software program was developed and used to produce discrete-time versions of selected continuous-time input signals to serve as input excitations. The input excitations were then transferred to an IBM compatible 386 PC where another software algorithm written in the 'C' programming language was used to

modulate various waveform parameters and to channel the input excitations to specified joints of the HMTB manipulator. While the HMTB manipulator arm responded to the input excitations, a data acquisition program written in the Ada programming language was used to extract joint data from the 1553 bus and to record the data to the HMTB Control Computer. This data includes the actual input/output time history from each joint. The recorded 1553 data file was then converted to an ASCII flat file format using an additional algorithm developed using the Matlab language. The ASCII flat file containing input/output time histories was then used for nonparametric and parametric analysis.

Prior to the identification experiments, assumptions were made as to the model form and bandwidth of the open-loop dynamics for each joint. First, a PD control model with feedforward torque was assumed for each joint. This assumption was based on analytical models of the flight arm and partial documentation for the ground-based manipulator. Because of the size of the HMTB manipulator as well as its intended purpose, the bandwidth for each joint was assumed to correspond to astronaut response times (3 to 5 Hertz). Due to this assumption, all input excitations used in this identification were limited to 10 Hertz to satisfy the Nyquist requirement. At least a second order model was expected due to proportional (P) and derivative (D) components initially assumed for each PD control loop. The following sections will provide more detail on the experiment design segments.

2. Input Excitations

According to Soderstrom and Stoica [9], the input signal used in an identification experiment can significantly influence the resulting parameter estimates. Also, certain system identification methods require special types of inputs depending on the type of identification to perform. With this in mind, various input signals (excitations) were used to identify the dynamic parameters of the hydraulic manipulator. Many of the input excitations used in the system identification experiments were considered 'normal' test signals such as simple sinusoids, sum of sinusoids, pseudorandom binary sequences, and chirp input signals. A bipolar ramping pulse test signal was also used. This signal was used as a means of determining amplitude response characteristics of the joints in question. All test signals, however, were used as input excitations in determining single-input, single-output (SISO) as well as multi-input, multi-output (MIMO) black box models of the selected hydraulic joints. All input excitations were fed through the hand controller interface. The actual input/output data used for system identification, however, were extracted from the 1553 bus which recorded the measured and commanded angles at each joint.

A. Description of Input Excitations

This section will describe the input signals used to excite the HMTB manipulator for the purpose of system identification. The rationale for selecting the signals will also be discussed along with a general declaration of properties and characteristics for each input signal.

As stated previously, several signals (input excitations) were used in determining the dynamic parameters of the dexterous orbital serving system manipulator arm. These input excitations include simple sinusoids, sum of sinusoids, pseudorandom binary

sequences, bipolar ramping pulses, and chirp signals. Each signal was used to excite three joints (shoulder yaw, shoulder pitch, and elbow pitch) of the HMTB arm. Modulation of signal parameters will be discussed later.

Good identification experiments provide informative data by which different models can be discriminated within an intended model set. To provide this informative data, persistently exciting (pe) input signals must be selected [10]. An input signal $u(n)$ is said to be pe of order m if the spectral density $\Phi(w)$ is not equal to zero for at least m points in the interval $-\pi < w < \pi$ for discrete-time systems. With the spectral density $\Phi(w)$ defined as the discrete Fourier transform of the correlation function, that is,

$$\Phi(w) \equiv \frac{1}{2\pi} \sum_{\tau=-\infty}^{\infty} R_u(\tau)e^{-w\tau}, \tag{2.1}$$

it has also been determined that $u(n)$ is pe of order m if the limit of the autocorrelation function exists, that is,

$$R_u(\tau) = \lim_{N \to \infty} \frac{1}{N} \sum_{t=1}^{N} u(t+\tau)u^T(t), \tag{2.2}$$

and the autocorrelation matrix

$$R_u(n) = \begin{bmatrix} R_u(0) & R_u(1) & .. & R_u(n-1) \\ R_u(-1) & R_u(0) & & : \\ : & & & : \\ R_u(1-n) & .. & .. & R_u(0) \end{bmatrix} \tag{2.3}$$

is nonsingular [10]. The white noise signal $e(t)$, simulated in Figure 11, is persistently exciting of all orders [9].
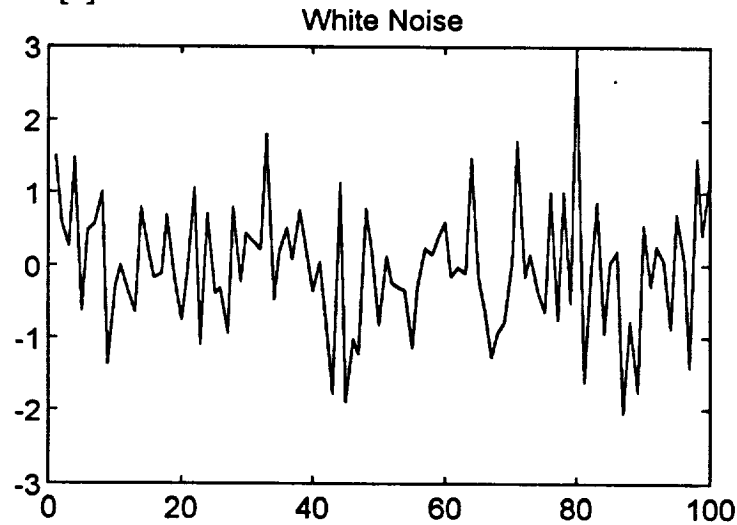
Figure 11. Simulated White Noise.

Sinusoidal Input

For the most simple input excitation, a sinusoid was selected to provide frequency response characteristics at a particular frequency and phase shift. Because of its simplicity, this signal was selected primarily for test purposes, that is, to determine if the joint in question was indeed responding to the input signal. Using a sinusoidal input

$$u(t) = a \sin(wt),\qquad(2.4)$$

the steady state output, assuming the system is linear, will become

$$y(t) = b \sin(wt + \phi)\qquad(2.5)$$

where

$$b = a \left| G(iw) \right|, \text{ and}\qquad(2.6)$$

$$\phi = \arg[G(iw)].\qquad(2.7)$$

The phase ϕ for this signal will be negative, else the system is responding with no input. It should be noted that this input excitation is rather sensitive to disturbances (noise) and could be improved by repeating the sinusoid at a number of frequencies to obtain a graphical representation of the transfer function $G(iw)$ as a function of w.

Sum of Sinusoids

A sum of sinusoids provides a slight variation from the simple sinusoid by increasing the number of sinusoidal inputs with distinct frequency components which yields a greater bandwidth (BW) in the frequency domain. This type of input is used primarily in transfer function analysis. The discrete-time sum of two sinusoids input expressed mathematically as

$$u(n) = a_1 \sin(w_1 n) + a_2 \sin(w_2 n)\qquad(2.8)$$

where

$$0 \le w_1 \le w_2 \le 2\pi\qquad(2.9)$$

was used in the identification experiments, though the number of sinusoids need not be limited to two. As a general rule, the input $u(n)$ will be pe of order $2m$ where m is the number of sinusoids in the sum [9]. Therefore, to identify a fourth order system, only two sinusoids need be summed. The power spectral density for an infinite sequence of the sum of sinusoids is

$$\Phi(w) = \frac{a_1^2}{4}[\delta(w - w_1) + \delta(w + w_1)] + \frac{a_2^2}{4}[\delta(w - w_2) + \delta(w + w_2)].\qquad(2.10)$$

13

Since there are exactly m=4 nonzero points in the interval $(-\pi, \pi]$, the actual input signal *u(n)* is said to be pe of order at least 4. Figure 12 displays a sum of two sinusoids signal where $a_1 = 1.0$, $a_2 = 1.0$, $w_1 = 0.02\pi$, and $w_2 = 0.08\pi$. Figure 13 displays a plot of the estimated power spectral density of the sum of sinusoids signal. Plots of the actual excitation signals used for system identification of the HMTB joints are shown in the next chapter along with their power spectral densities.

For notation purposes, the term 'sum of sinusoids at 10 Hertz' used in this thesis means that the highest frequency component f_2 of the given condition $f_2 = 4f_1$ for the sum of two sinusoids input will be equal to 10 Hz. This also implies that the lower frequency component f_1 is equal to 2.5 Hz. For all sum of two sinusoids experiments performed on the HMTB joints, the arbitrarily selected condition $f_2 = 4f_1$ will hold.
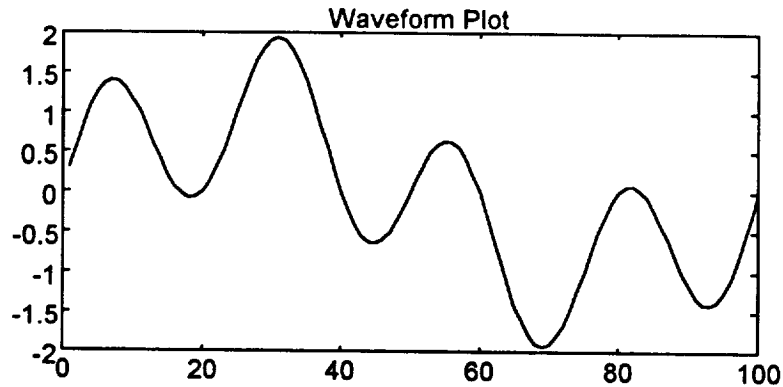
Figure 12. Sum of Sinusoids.
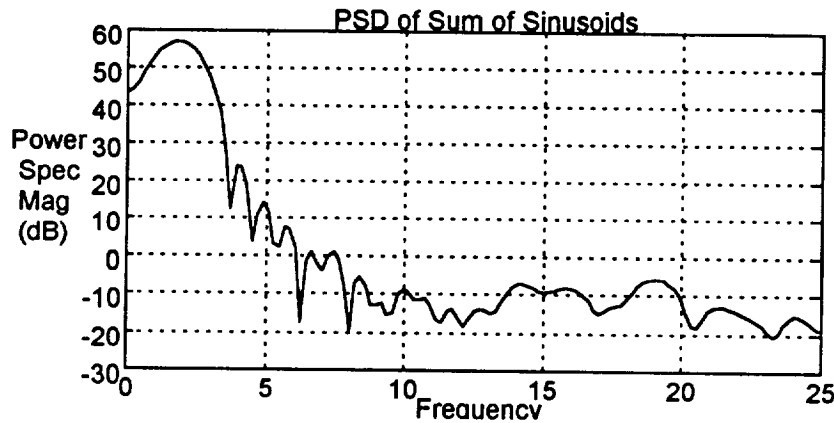
Figure 13. PSD of Sum of Sinusoids.

Pseudorandom Binary Sequences

Due to their easy generation, the pseudorandom binary sequence (PRBS) has been a convenient input signal for many identification methods. The PRBS signal shifts between two levels in a certain pattern such that its first- and second-order characteristics, the mean value μ and the correlation function $R_u(\tau)$, are very similar to those of a white noise process *e(t)* provided that the number of samples used in the PRBS calculation is large. Interpretations vary as to the actual number of samples used, but is usually

14

experiment dependent. Therefore, this type of input signal applies itself well to determine correlation effects of various system parameters. Since the PRBS is band-limited and is periodic, it differs from a true white noise process. The PRBS is said to be pe of order equal to its period. Soderstrom and Stoica [9] indicate that in most cases the period of a PRBS is chosen to be of the same order as the number of samples in the experiment, or larger. Figure 14(a) depicts the PRBS signal. Its mathematical expression can be realized as

$$u(t) = (C_1 + C_2) + (C_1 - C_2)\text{sign}(R(\tau) \ u(t-1) + w(t))$$ (2.11)

where

C_1 and C_2 are permissible binary levels,

$R(\tau)$ is the covariance function, and

$w(t)$ is a simulated white noise process.

Figure 14(b) displays the power spectral density of the PRBS input signal.
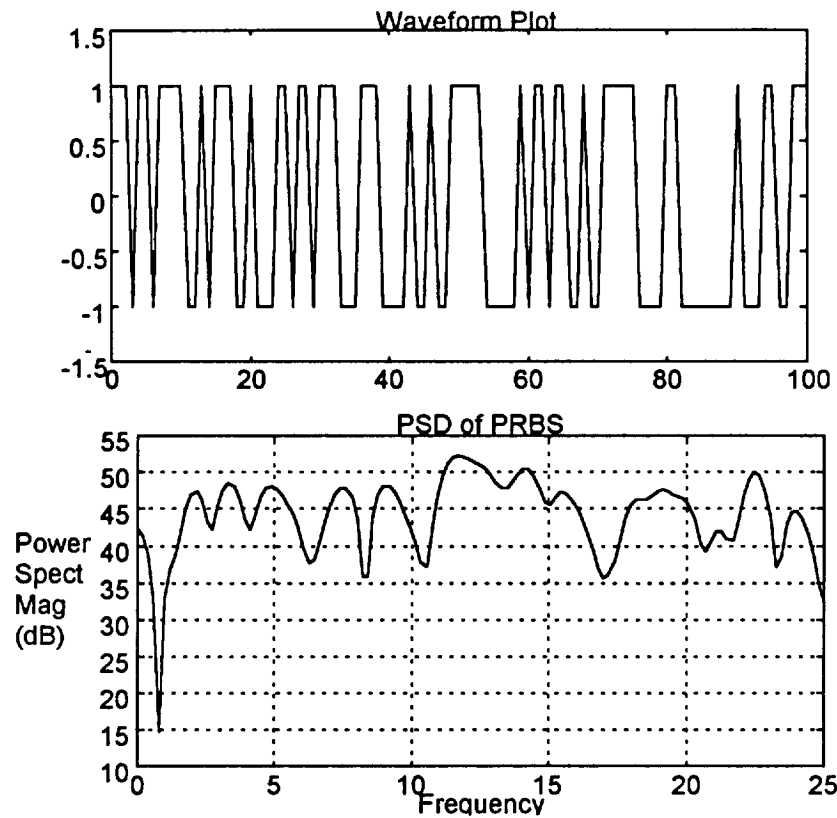
Figure 14. (a) Pseudorandom Binary Sequence (b) PSD of PRBS.

Chirp Signal

Chirp is a technique invented by B. M. Oliver at Bell Labs in which signals are represented by a rapid up or down sweep in frequency [13]. Chirp signals (sine sweeps) have been used for both radar and communication applications. This waveform was chosen as an input signal because of its selectable frequency range. Chirp signals have been known to produce regions with low power spectrum [14]. For this reason, Franklin, Powell, and Workman [14] describe an expression for a chirp signal that does not have low power spectrum in the desired bandwidth. Their chirp waveform is expressed as

$$r_k = A_0 + a_k \sin 2\pi f_k k, \tag{2.12}$$

$$a_k = a_{max} \text{ sat}\left(\frac{k}{\rho N}\right) \text{sat}\left(\frac{N-k}{\rho N}\right), \text{ and} \tag{2.13}$$

$$f_k = f_{start} + \frac{k}{N}(f_{stop} - f_{start}), \tag{2.14}$$

where

N = number of points in the data window,
A_0 = constant reference offset adjustment,
a_{max} = maximum amplitude,
ρ = fraction of window length for amplitude ramps,
f_{start} = starting frequency of chirp, and
f_{stop} = stopping frequency of chirp.

The chirp expression used in the identification experiments of this thesis, however, can be characterized with the following equation:

$$u(t) = \cos(2\pi(f_l + t\Delta) + 2\pi f_o t) \tag{2.15}$$

where

f_l is the starting frequency,
f_h is the ending frequency,
f_0 is the center frequency, and
$\Delta = f_h - f_l$.

A chirp waveform is shown in Figure 15(a) having values f_l = 1 Hz, f_0 = 4 Hz, and f_h = 2 Hz. The power spectral density of the chirp is shown in Figure 15(b).

Bipolar Ramping Pulse

The bipolar ramping pulse shown in Figure 16 has been included primarily to test the amplitude response characteristics of the manipulator joints. This input signal produces a series of periodic, alternating, ramping pulses. The user defined pulse width remains constant throughout the pulse sequence. In system identification literature, the impulse and step inputs have been used for transient analysis for several nonparametric

16
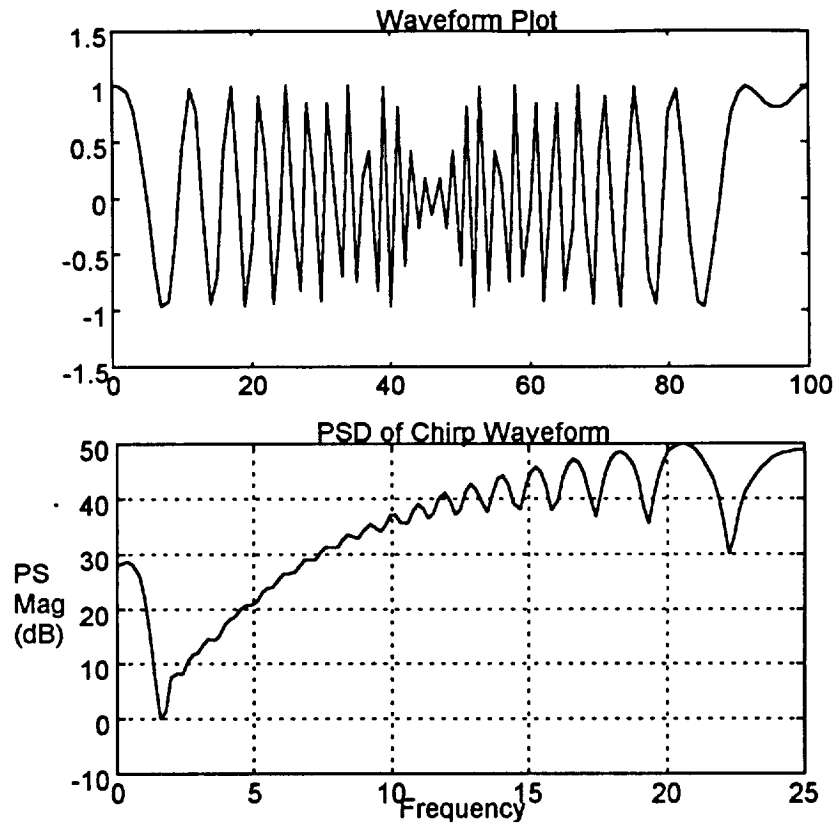
Figure 15. (a) Chirp Waveform (b) PSD of Chirp Waveform.
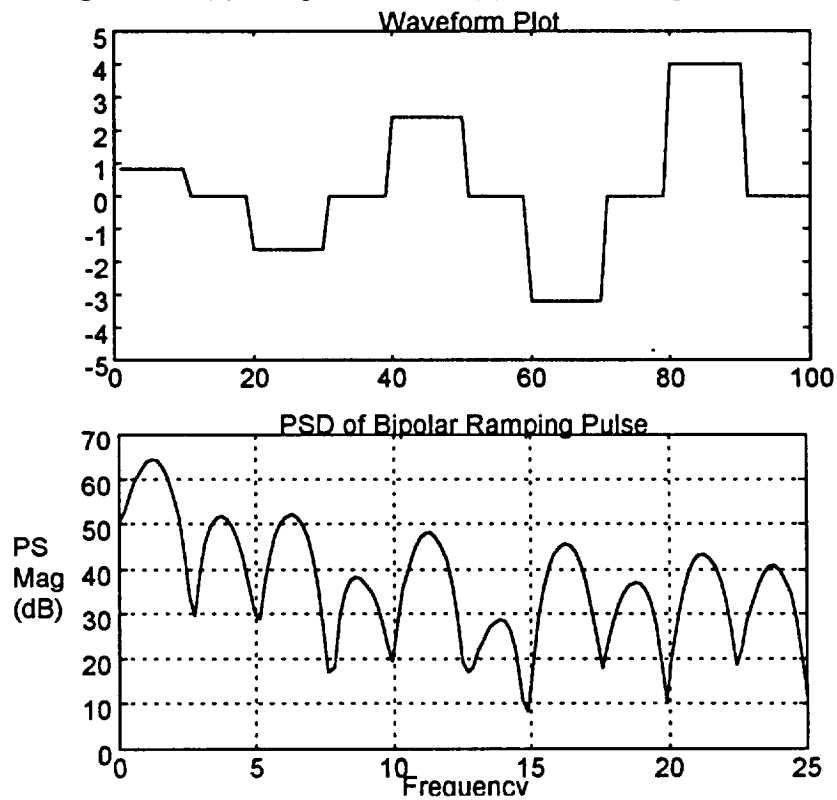
Figure 16. (a) Bipolar Ramping Pulse (b) PSD of Bipolar Ramping Pulse.

identification experiments. This sequence of alternating, ramping pulses will serve as a test signal for parametric model estimation.

B. Generation of Input Excitations

All input excitations were generated by a program written using MATLAB. The program allows a user to graphically display the generated waveform after selecting its appropriate parameters, such as its frequency and amplitude. The software then outputs a 100-point waveform data file representing a discrete-time version of the continuous-time signal. Most data files contained one complete cycle of the waveform in order to allow the excitation control computer to accurately control the frequency of the selected discrete-time waveform. The length of the actual excitation is a periodic version of the 100 samples. In this way, each excitation was allowed to reach steady-state conditions. Figure 17 shows the initial user interface for the waveform generation software.
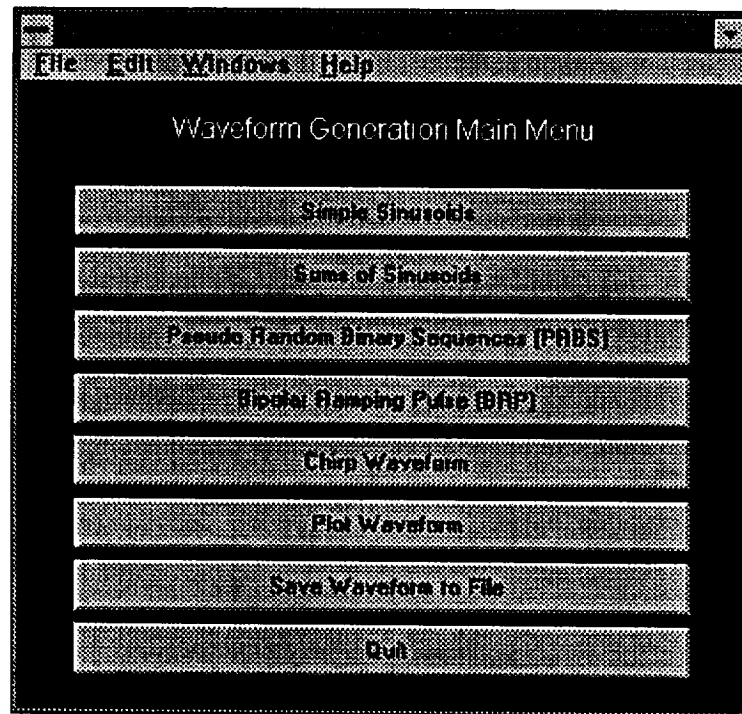
Figure 17. Waveform Generation Software User Interface.

3. Input Excitations and Control

As seen in the overall experiment design depicted in Figure 10, the generated waveform is controlled and channeled to various joints of the HMTB manipulator by the excitation control computer. This section will describe the hardware, procedures, and algorithms used to channel the generated excitation signals to specific joints of the HMTB manipulator for the purpose of conducting single-input, single-output (SISO) and multi-input, multi-output (MIMO) system identification tests.

A.   Single Joint Excitation

The excitation control computer, an IBM 386 PC, was used to perform all system identification tests.   This PC contained the AT-MIO-16 National Instruments data acquisition board [15].   The AT-MIO-16 applies itself well to various multifunction analog, digital, and timing applications. In the experiment design, the AT-MIO-16 was used to convert the discrete-time input waveform to an equivalent frequency modulated analog signal. This was accomplished by forming a periodic version of each 100-sample waveform and then outputting the new frequency modulated signal through the digital-to-analog converter.

Since the purpose of the identification experiment was to identify a dynamic model localized about an RPCM trajectory vector, the excitation control computer was interfaced to the HMTB manipulator at the exact location astronauts would be interfaced, that is, at the interface for the 2x3 DOF hand controller.   Figure 18 shows the wiring implementation used to interface the AT-MIO-16 data acquisition board to the 2x3 DOF hand controller processor for SISO identification tests.

AT-MIO-16 board   2x3 DOF HC processor

	HC GND	
Dig Out 24 o—		—o pin 8
	HC Activation	
Dig Out 25 o—		—o pin 20
	Single Axis Input	
DAC0 20 o—		—o pin 16

Figure 18. Single Axis Interface Configuration.

Each single axis test consisted of moving the HMTB arm autonomously to the RPCM initial trajectory called the RPCM HOLSTER OUT APPROACH POINT. Next, the HMTB manipulator was placed in single joint mode allowing only the selected joint to accept input while all other joints were actively servoing. With the RPCM ORU (Figure 9) loaded in the HMTB end effector, input control was transferred to the excitation control computer to perform the SISO tests in Table 1. All SISO tests were performed in position mode with direct input to each joint variable.

Code written in the 'C' language was used to modify the control frequency and number of waveform iterations of the AT-MIO-16 board. For safety reasons, all AT-MIO-16 single axis input excitations were first tested on an oscilloscope.

19

Single Input/Single Output Tests

Test No.	Input Excitation	Maximum Amplitude	Time/Frequency Characteristics
1	single sinusoid	1	freq=5 Hz
2	sum of two sinusoids	1	$freq_1$=1.25 Hz, $freq_2$=5 Hz
3	sum of two sinusoids	2	$freq_1$=1.25 Hz, $freq_2$=5 Hz
4	sum of two sinusoids	1	$freq_1$=2.5 Hz, $freq_2$=10 Hz
5	pseudorandom binary sequence	1	order<100
6	pseudorandom binary sequence	2	order<100
7	bipolar ramping pulse	4	freq=1 Hz, pulse width=0.1 sec
8	chirp signal	1	$freq_{start}$=5 Hz, $freq_{end}$=10 Hz

Table 1. Single-Input, Single-Output Tests.

B. Multiple Joint Excitation with Bias Compensation

Multi-input, multi-output (MIMO) tests, shown in Table 2, were used to identify the dynamical characteristics of the HMTB joints as well as to verify the models obtained using the SISO identification tests. The excitation control computer to HMTB manipulator wiring interface used in the SISO experiments was modified for the MIMO

Multiple Input/Multiple Output Tests

Test No.	Input Excitation	Maximum Amplitude	Time/Frequency Characteristics
1	single sinusoid	1	freq=5 Hz
2	single sinusoid	2	freq=5 Hz
3	single sinusoid	2	freq=10 Hz
4	sum of two sinusoids	1	$freq_1$=1.25 Hz, $freq_2$=5 Hz
5	sum of two sinusoids	2	$freq_1$=1.25 Hz, $freq_2$=5 Hz
6	sum of two sinusoids	2	$freq_1$=2.5 Hz, $freq_2$=10 Hz
7	pseudorandom binary sequence	1	order<100
8	pseudorandom binary sequence	2	order<100
9	bipolar ramping pulse	4	freq=1 Hz, pulse width=0.1 sec
10	chirp signal	1	$freq_{start}$=0 Hz, $freq_{end}$=1 Hz
11	chirp signal	1	$freq_{start}$=0 Hz, $freq_{end}$=5 Hz
12	chirp signal	1	$freq_{start}$=5 Hz, $freq_{end}$=10 Hz
13	chirp signal	1	$freq_{start}$=5 Hz, $freq_{end}$=15 Hz

Table 2. Multi-Input, Multi-Output Tests.

tests. This modification involved designing and implementing a bias compensator to offset the 2x3 DOF hand controller biases in the X, Y, and Z translational axes. Figure 19 shows the bias compensating wiring scheme used to interface the AT-MIO-16 data acquisition board to the 2x3 DOF hand controller processor for MIMO identification tests.

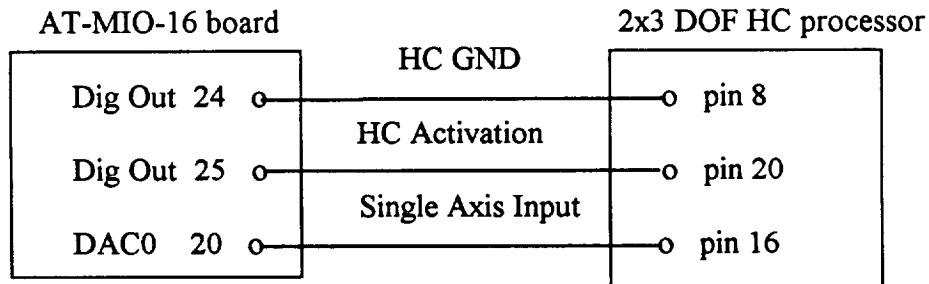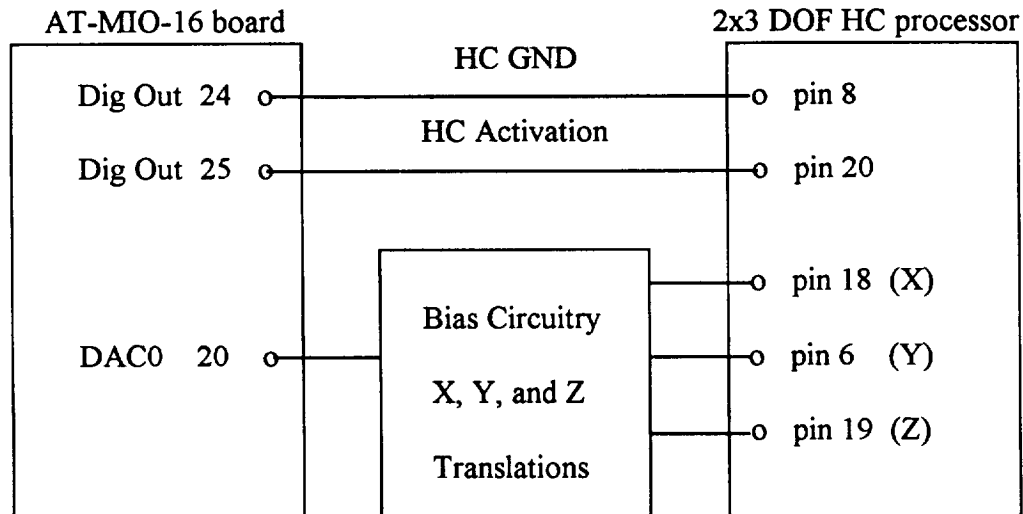AT-MIO-16 board   2x3 DOF HC processor

Figure 19. Multiple Axes Interface with Bias Compensation.

Preliminary procedures for MIMO testing involved moving the HMTB arm autonomously to the RPCM HOLSTER OUT APPROACH POINT and then transferring input control to the excitation control computer. The HMTB manipulator was then placed in Cartesian mode allowing only the translational inputs to accept values with respect to the end effector control frame. All rotational inputs (Euler angles) were held as constant as possible. With the RPCM ORU loaded in the HMTB end effector, the excitation control computer performed the MIMO tests in Table 2. All MIMO tests were performed in position mode.

4. 1553 Bus Data Acquisition

As each identification test was performed on the HMTB manipulator, an Ada software program recorded various joint parameters. The 1553 data acquisition program recorded, measured, and commanded joint angles from sensors located at the manipulator actuators as well as force and moment data from the force-torque sensor located at the end effector. Data was recorded at 50 Hz, which is the fixed position loop transfer rate. This rate served to provide the Nyquist sampling frequency (25 Hz) for the input excitations used. In the identification experiments, the excitations were well below the Nyquist frequency. The Nyquist rate, however, was not as important as the bandwidth of the excitations.

Another constraint imposed on the experiment design was the limited available memory storage for recording the joint data. Approximately twenty minutes of recording time was allotted on the control station computer. This equates to recording a total of

five experiment tests per run. After each set of five tests, the recorded files would have to be transferred to another computer to provide memory for another set of tests.

5. 1553 Bus Format to ASCII Conversion

The final segment of the experiment design involved converting the 1553 recorded data file to an ASCII flat file format. This task was performed by a MATLAB conversion program. The conversion program extracted measured and commanded joint data from the 1553 formatted data file to be identified and saved this data in an ASCII flat file format to be used for nonparametric and parametric analysis.

III. Nonparametric Model Estimation

As a precursor to parametric identification, nonparametric methods are used first to extract characteristics of the unknown system which provides information in how to apply various parametric techniques. This chapter will show results of applying frequency, correlation, and spectral analysis techniques to the shoulder yaw, shoulder pitch, and elbow pitch joints of the HMTB manipulator. The results will help determine appropriate parametric model structures for the next chapter.

1. Procedure Description and Rationale

Nonparametric model estimation involves determining a system's characteristics from Bode plots and plots of input/output cross-correlation. Though sufficient, nonparametric methods give only moderately accurate models. For time domain nonparametric analysis, the impulse response and the step response are both useful in determining some basic control related characteristics of a system such as delay time, static gain and dominating time constants. Frequency domain techniques provide information such as the estimated transfer function, the bandwidth of a system, and a system's phase characteristics. The techniques employed in this investigation include transfer function analysis, correlation analysis, and spectral analysis.

Transfer function analysis was used to determine the frequency response of the yet to be identified system. This information helped to determine the frequency range of the input excitations to be used in the identification experiments. The frequency response approach was performed by applying a sum of sinusoidal inputs to the system and then recording the input/output time histories for each joint. Autocorrelation and cross-correlation functions were first computed from the data and then transformed to power spectral density and cross-power spectral density estimates, respectively. Spectral estimates were smoothed and averaged by using a Hamming window with the lag length approximately equal to a tenth of the number of data points. The estimated transfer function for each joint was computed as the ratio of the cross-power spectrum to the input power spectrum. Each joint's transfer function estimate was represented in the form of Bode plots.

Correlation analysis techniques were employed to provide information on the degree of linear dependence of a system's parameters, that is, how well future values of the data can be predicted based on past observations. Correlation analysis is usually based on white noise or any input signal that is independent of the disturbances. A distinct advantage of correlation techniques is its insensitivity to additive noise on the output [9].

Spectral analysis, a very versatile nonparametric technique, used various persistently exciting input signals to yield spectral estimates of the system. The spectral density or spectrum is a frequency domain function used to measure the frequency distribution of the mean square value of the data. Spectral estimates for each joint were computed using a Hamming window with the lag length approximately equal to a tenth of the number of data points.

2. Shoulder Yaw Joint
A. Transfer Function Analysis

Since astronauts will use the hand controller to operate the manipulator joints and the input signals for this identification were introduced through the same interface, the frequency range of the input signals were selected to coincide with astronaut response times (3 to 5 Hz) [16]. To perform transfer function analysis of the shoulder yaw joint, a sum of two sinusoids input whose frequency content ranged from 2.5 Hz to 10 Hz was introduced into the shoulder yaw position loop. The upper frequency (10 Hz) was selected because it was at least twice the average frequency response for astronauts. Deductively, if the identified model is valid for twice the intended bandwidth then it is reasonable to assume that the actual model will be well behaved within the intended 3 to 5 Hz bandwidth. Figure 20 shows both sum of sinusoids input and output discrete time sequences recorded for the shoulder yaw joint during the identification experiment. As seen in Figure 20, considerable noise is present on the input signal. From the actual output sequence in this same figure, it is clear that the data is affected by disturbances. This is perhaps due to background interference being carried through the hardware interface. Figure 21 shows a magnified version of the shoulder yaw joint waveforms. This version of the input sequence shows the effect of the sample-and-hold and quantization functions being implemented by the HMTB control computer on the hand controller signal.
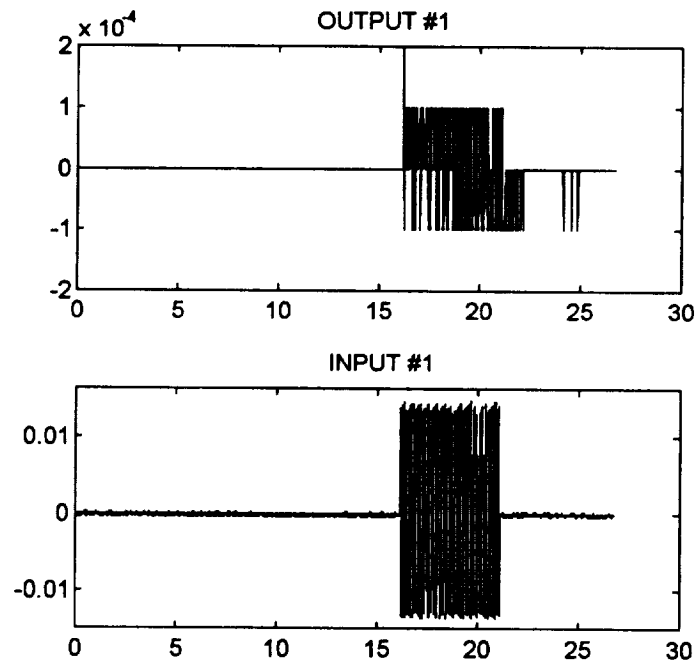

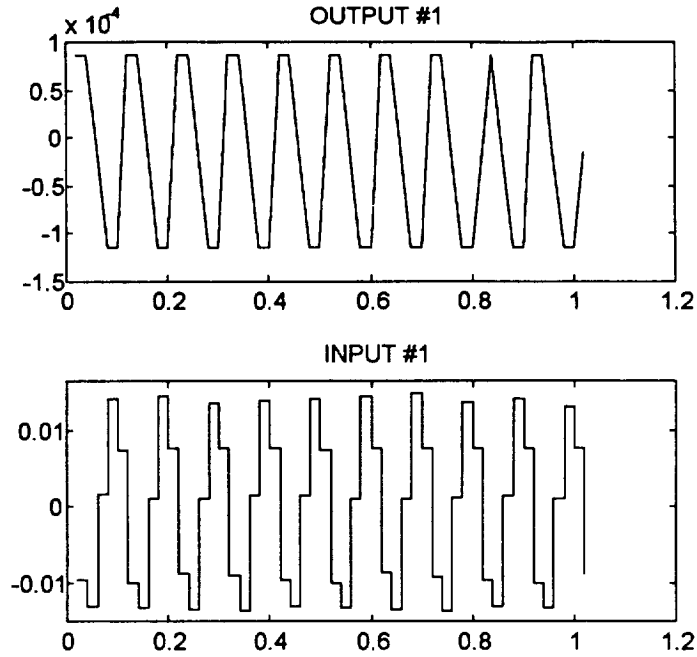Figure 20. Shoulder Yaw Sum of Sinusoids I/O at 10 Hertz.

Figure 21. Shoulder Yaw Sum of Sinusoids Activity.

If the dynamics of the shoulder yaw joint is assumed to be linear in a small localized region, then the output $y(t)$ can be seen as a weighted sequence of the form

$$y(t) = \sum_{k=0}^{\infty} h(k) u(t-k) + v(t) \tag{3.1}$$

where

$h(k)$ is the weighting sequence, and

$v(t)$ is the disturbance.

The autocorrelation function may be estimated from the input data sequence as follows:

$$R_u(\tau) = \lim_{N \to \infty} \frac{1}{N} \sum_{t=1}^{N} u(t+\tau) u^T(t). \tag{3.2}$$

Note that the cross-correlation function $R_{yu}(\tau)$ may be computed in the same manner. Taking the Fourier transform of

$$R_{yu}(\tau) = \sum_{k=0}^{\infty} h(k) R_u(\tau - k) \tag{3.3}$$

yields

$$\Phi_{yu}(w) = H(e^{-iw}) \Phi_u(w). \tag{3.4}$$

25

The estimated transfer function is computed as

$$H(e^{-iw}) = \Phi_{yu}(w) / \Phi_u(w).$$

$$(3.5)$$

The discrete-time transfer function estimate for the sum of sinusoids data sequence is shown in Figure 22.
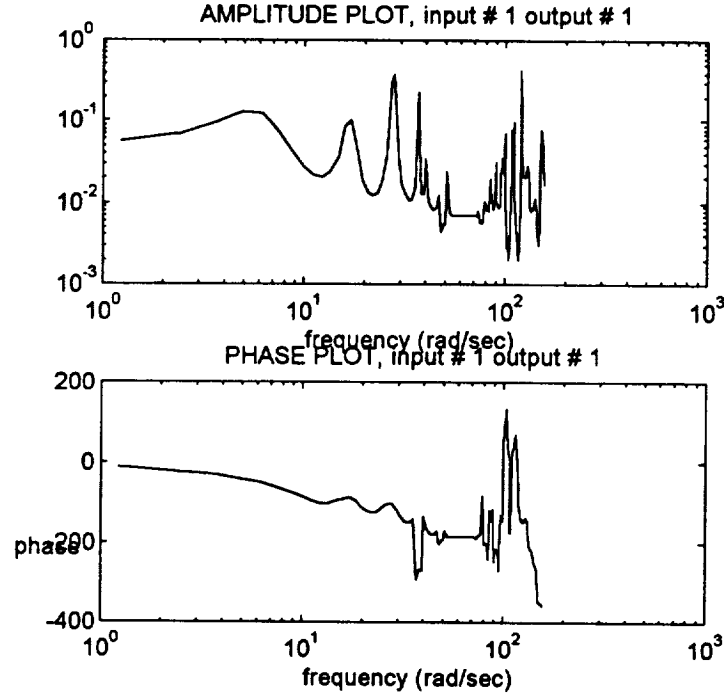

Figure 22. Shoulder Yaw Transfer Function Estimate.

Graphical interpretation of this transfer function yields a gain less than one for the entire bandwidth with a low frequency cutoff at approximately $w=$ 6 rad/sec. The negative slope slightly above the break frequency indicates a second-order system until approximately 10 rad/sec. The rest of the graph shows additional resonances and disturbances of the system above 10 rad/sec.

B. Correlation Analysis

Correlation analysis techniques were applied to the shoulder yaw joint to provide information on the degree of linear dependence of the input and output of the joint. Correlation analysis is usually based on white noise or any input signal that is independent of the disturbances. For this reason, a pseudorandom binary sequence (PRBS) was used to excite the joint. PRBS signals simulate white noise statistical properties for the purpose of nonparametric identification. The one difference between PRBS and white noise is its periodicity. The mathematical PRBS expression has already been shown (2.11). Figure 23 shows the entire input/output sequence of the PRBS input signal applied to the shoulder yaw joint during the identification experiment. Figure 24 shows a magnified version of the PRBS shoulder yaw joint activity.

Explanation of correlation analysis can be discussed by using the definition of the covariance function, that is,

$$C_{xy}(\tau) = E[\{x(t) - \mu_x\}\{y(t + \tau) - \mu_y\}] \qquad (3.6)$$

where

$E[\ ]$ is the expectation operator,

μ_m is the expected value (mean) of sequence m.

It can be shown that the covariance function and the correlation function are related through the following relationship,

$$C_{xy}(\tau) = R_{xy}(\tau) - \mu_x\mu_y. \qquad (3.7)$$

Since the PRBS has zero mean, the covariance and correlation functions are equivalent.

Figure 25 shows three graphical representations of the output covariance (the autocorrelation of the output), the autocorrelation of the input, and the cross-correlation from the input to the output. The first graph in Figure 25 shows how the output signal is correlated with the transfer function. The autocorrelation of the input shows a signal that is white in nature but exhibits some periodicity as can be seen by the small graphical peaks which is expected for a PRBS. The autocorrelation graph of the input is typical since the autocorrelation function is an even function. The autocorrelation function evaluated at zero yields the mean square value of the input. The cross-correlation graph displays propagation characteristics of the joint such as the distance and/or the velocity of an input through the system. Cross-correlation also gives an estimate of the order of the system. The peaks of the cross-correlation graph indicate the contribution of each of several independent sources of excitation found in the output measurement.
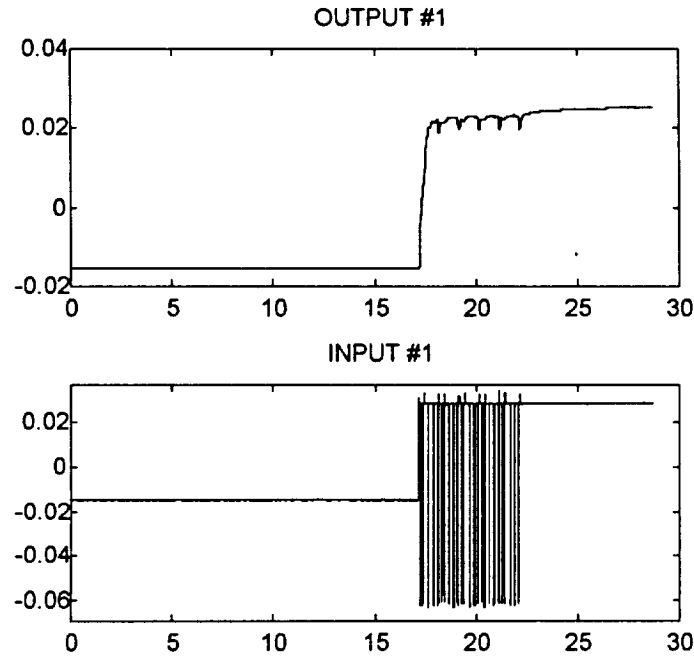

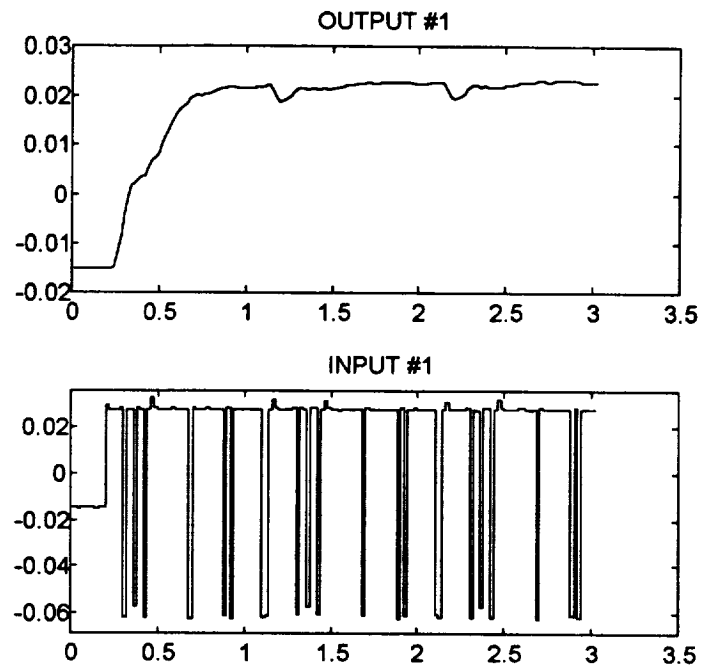Figure 23. Shoulder Yaw PRBS Data.
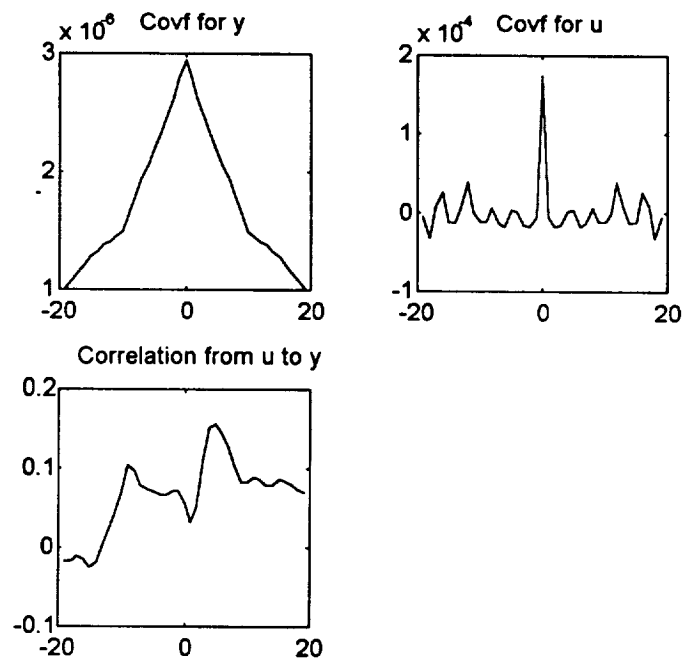
Figure 24. Shoulder Yaw PRBS Activity.

Figure 25. Shoulder Yaw Correlation Plots.

C. Spectral Analysis

Spectral analysis, the Fourier transform of the autocorrelation function, was used to measure the frequency distribution of the mean square value of the data. Two input excitations were used to determine the spectra of the joint. The bipolar ramping pulse (BRP) whose energy focused around 1 Hz was used while a sum of two sinusoids input was used with frequency components at 2.5 and 10 Hz.

The bipolar ramping pulse signal was used to determine several spectral estimates of the shoulder yaw joint (Figure 26). Each spectral estimate was computed using a Hamming window.
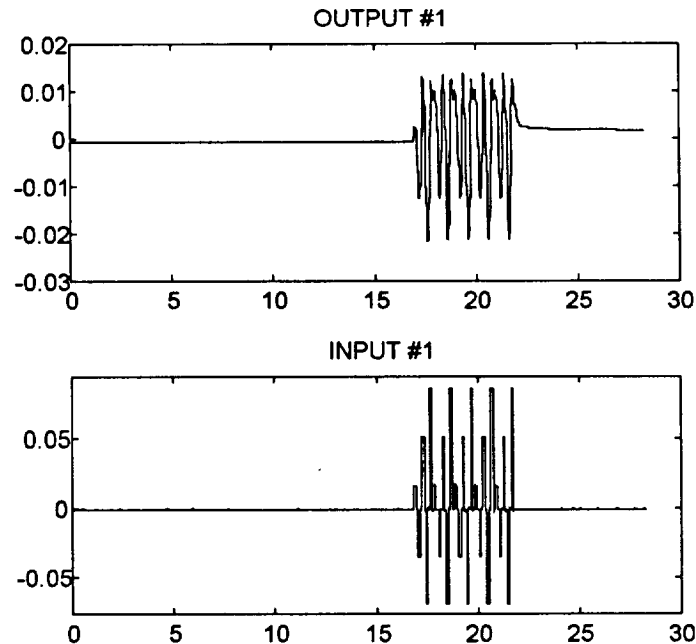
OUTPUT #1

INPUT #1

Figure 26. Shoulder Yaw Bipolar Ramping Pulse Data.

Plots of the estimated disturbance spectrum, the output spectrum, the input power spectrum, and the cross-spectrum are shown in Figures 27 through 30, respectively. The plots indicate that disturbance phenomena are predominantly focused in the lower frequencies around one hertz. The output spectrum and the input power spectral density (PSD) both show higher amplitudes in the one to five hertz range. Various higher frequency lobes indicate that other modes of the system are being excited by the input signal. The estimated cross-spectrum reveals the same information.

The small spectral amplitudes are attributed to the very small hand controller gains used in the HMTB control computer. That is, the HMTB computer system scaled the HC signals to a very small range before allowing the input signals to enter the position control loop. Since the experiment control computer, used to perform the system identification tests, was interfaced through the hand controller hardware, it was subject to the same input scaling resulting in small spectral amplitudes.
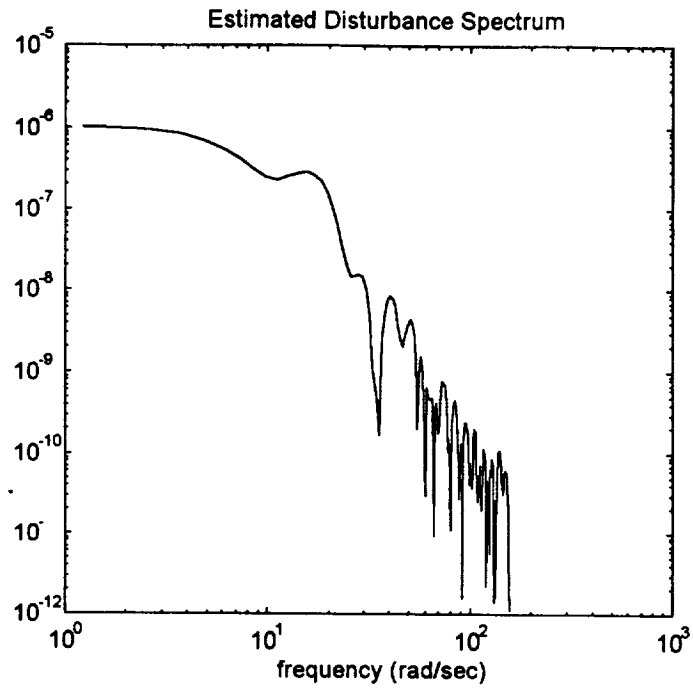
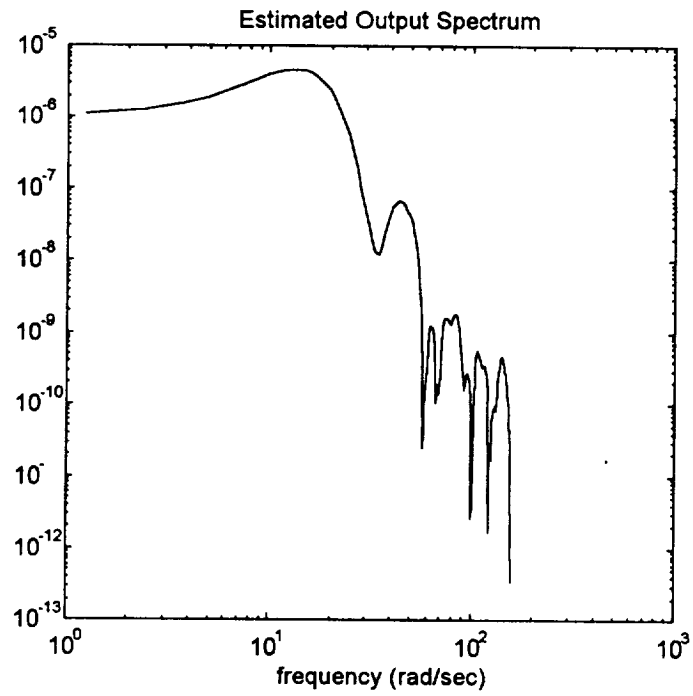Figure 27. Shoulder Yaw Estimated Disturbance Spectrum.

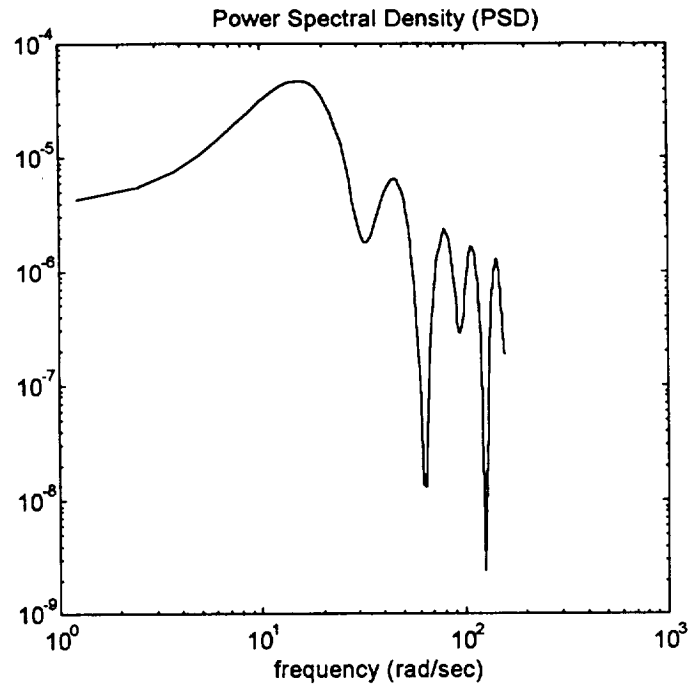Figure 28. Shoulder Yaw Estimated Output Spectrum.

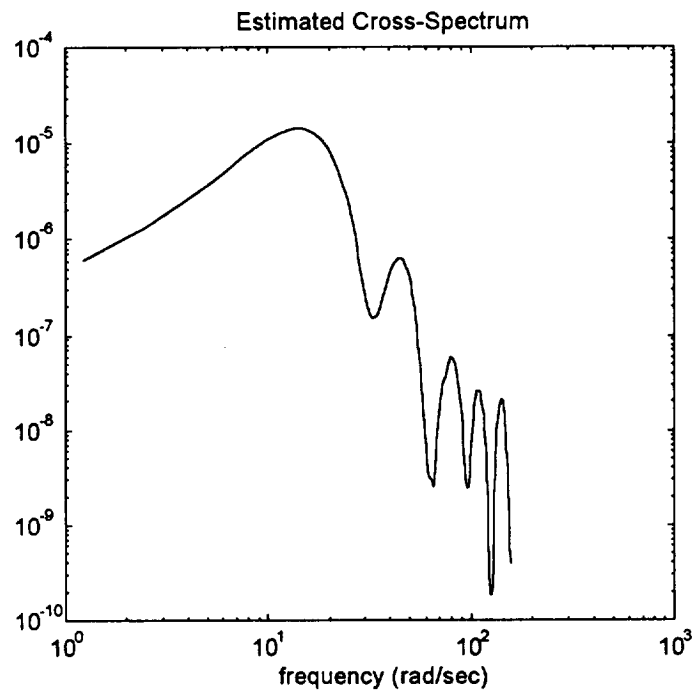Figure 29. Shoulder Yaw Estimated Input Power Spectrum.

Figure 30. Shoulder Yaw Estimated Cross-Spectrum.

The sum of sinusoids input signal was used to determine several spectral estimates for frequencies less than 10 Hertz (62.8 rad/sec). Each spectral estimate was computed using a Hamming window. Figure 31 shows the entire I/O data record for the shoulder yaw joint. Figure 32 shows the sum of sinusoids activity.

31

Spectral estimates, Figures 33 through 36, reveal that the disturbances are at least two orders of magnitude lower for frequencies less than 10 Hertz (62.8 rad/sec). The estimated cross-spectrum reveals that other modes of the system are being excited.
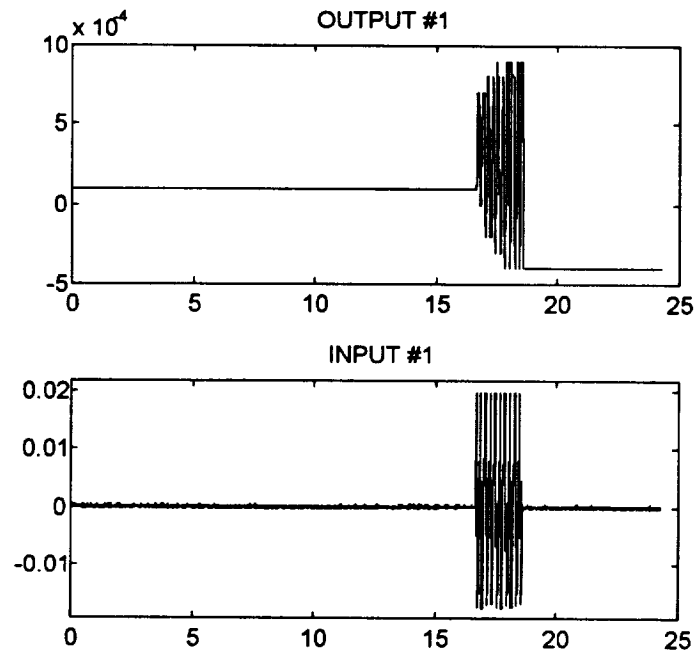
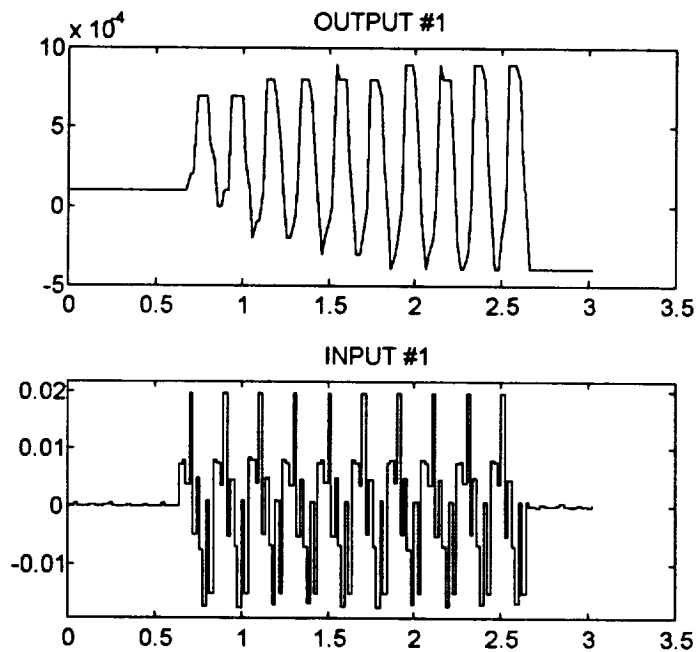Figure 31. Shoulder Yaw Sum of Sinusoids Input.

Figure 32. Shoulder Yaw Sum of Sinusoids Activity.
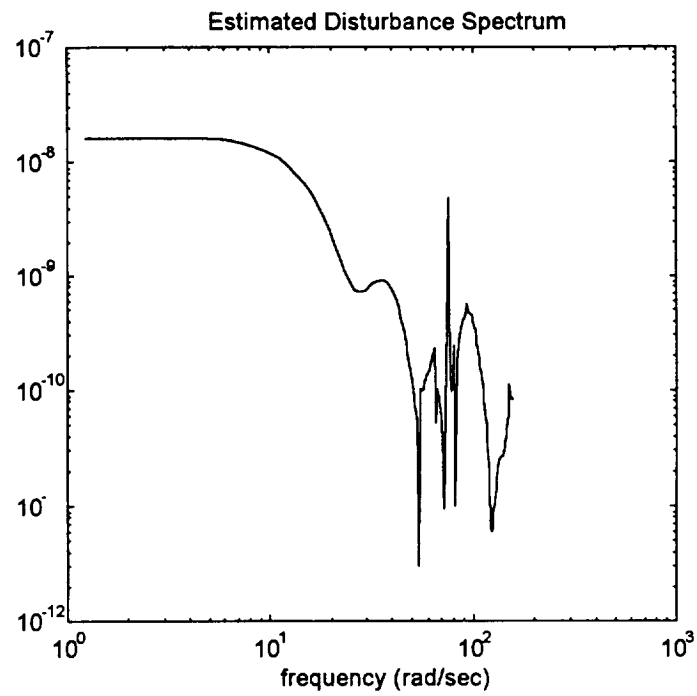
Figure 33. Shoulder Yaw Estimated Disturbance Spectrum.
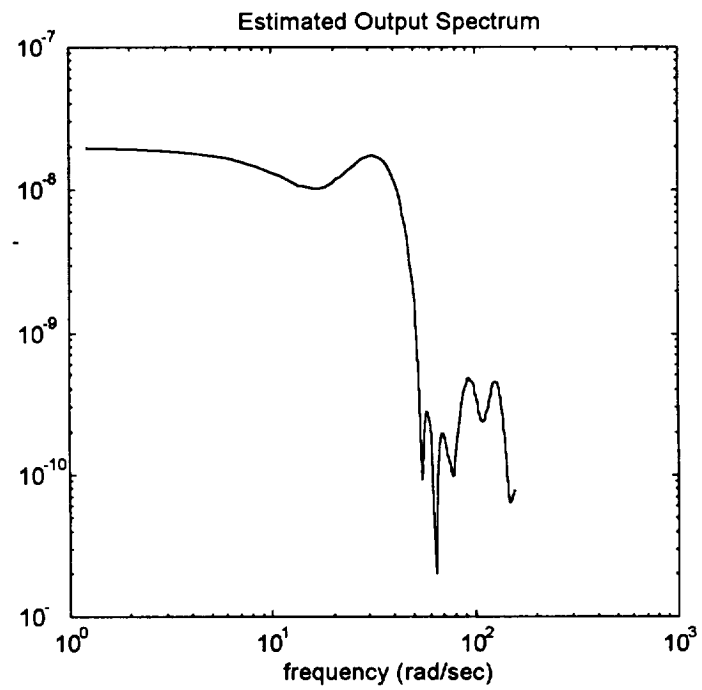

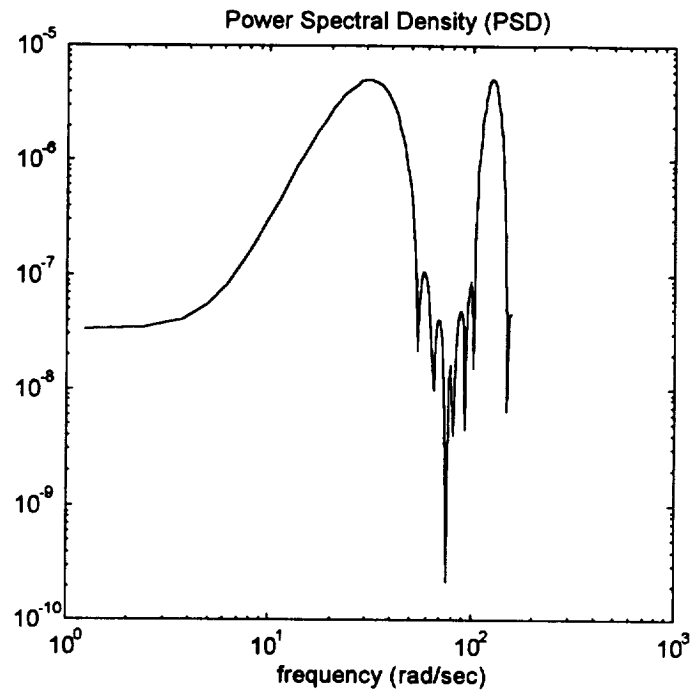**Figure 34. Shoulder Yaw Estimated Output Spectrum.**
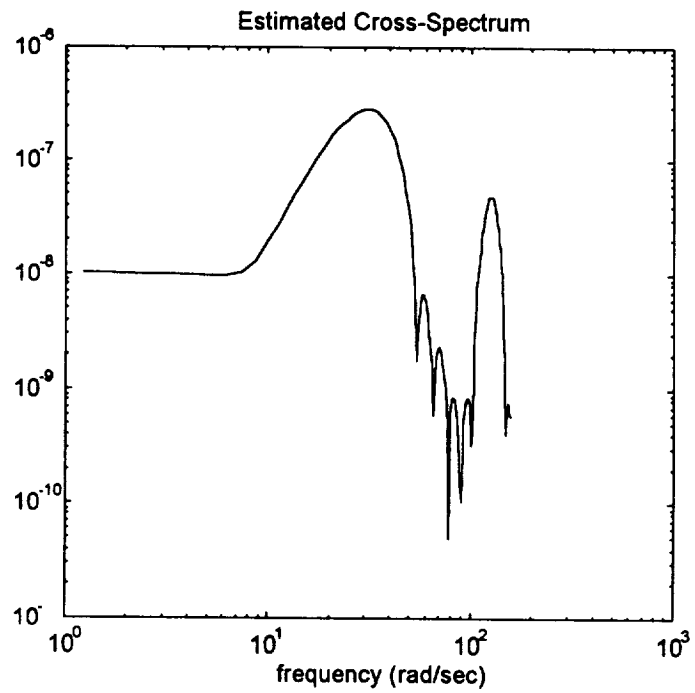
Figure 35. Shoulder Yaw Estimated Power Spectrum.

Figure 36. Shoulder Yaw Estimated Cross-Spectrum.

3. Shoulder Pitch and Elbow Pitch Joints

Identical nonparametric procedures performed for the shoulder yaw joint were also performed for the shoulder pitch and elbow pitch joints. Transfer function analysis for both joints yielded break frequencies at approximately seven radians per second. Correlation analysis as applied to both joints yielded two to five delay units from the input to the output of each joint implying possible system orders. Results from spectral analysis for each joint indicated that the disturbances were at least an order of magnitude lower than the output spectrums. Plots and graphs from the nonparametric procedures described above are displayed in Appendix A.1 for both shoulder pitch and elbow pitch joints.

4. Nonparametric Conclusions

Transfer function analysis, correlation analysis, and spectral analysis techniques have been used to determine a crude nonparametric estimation of three HMTB manipulator joints (shoulder yaw, shoulder pitch, and elbow pitch). The nonparametric model estimation techniques used in this chapter suggest that parametric models should be selected to properly model the noise dynamics as well the system's dynamics.

Nonparametric analysis described each joint with minor to moderate process and measurement disturbances. The plots reveal greater measurement disturbances than process disturbances. Transfer function analysis of each joint indicates that models need to be constructed within a 1 to 5 Hz bandwidth.

Errors in the nonparametric estimations may be attributed to several sources: random errors, bias errors, quantization errors in the experiment design, and choice of input signal. Random errors are caused by nonlinearities in the system. Bias errors are due to resolution errors in the spectral density estimates as well as unmeasured inputs that contribute to the output. Quantization errors are caused by the sample-and-hold function used in the HMTB control computer when accepting the hand controller input signal. Velocity limits in the control system also contributed to errors in the estimations. The experiment design introduced errors on the input measurements with improperly shielded wires in the experiment control computer interface. When these errors are introduced into an experiment design, the likelihood of obtaining accurate estimates decreases.

IV. Parametric Model Estimation:
Transfer Function and State-Space System Identification

The parametric identification procedures employed in this chapter use various black-box transfer function model structures to determine model estimates for the HMTB joints. The transfer function models, found within the *MATLAB System Identification Toolbox* by Lennart Ljung, use prediction error techniques to determine parameters for each black-box model. Residual analysis and cross-validation procedures will be primarily used to choose the best model estimate for each joint.

1. Parametric Procedures

Though sufficient, nonparametric methods as discussed in the previous chapter give only moderately accurate models from observed input/output data. To obtain more accurate model estimates, parametric identification techniques are used. The basic requirements for parametric identification are the observed input/output data, a set of candidate model structures, and a criterion to select the best model in the set [10]. The system identification process as described by Ljung is shown in Figure 37, that is, after data has been collected from an experiment, a model structure is chosen, the criterion to identify a particular model in the structure is selected, the model is then calculated and validated. If the model is not satisfactory, another criterion is selected or another structure is chosen. Ljung's parametric identification process is quite iterative [10].

```
┌─────────────────────────────┐
│       Obtain I/O Data        │
└─────────────────────────────┘
              │
              ▼
┌─────────────────────────────┐
│      Choose Model Set        │
└─────────────────────────────┘
              │
              ▼
┌─────────────────────────────┐
│    Choose Criterion to Fit   │
└─────────────────────────────┘
              │
              ▼
┌─────────────────────────────┐
│       Calculate Model        │
└─────────────────────────────┘
              │
              ▼
┌─────────────────────────────┐
│        Validate Model        │
└─────────────────────────────┘
```
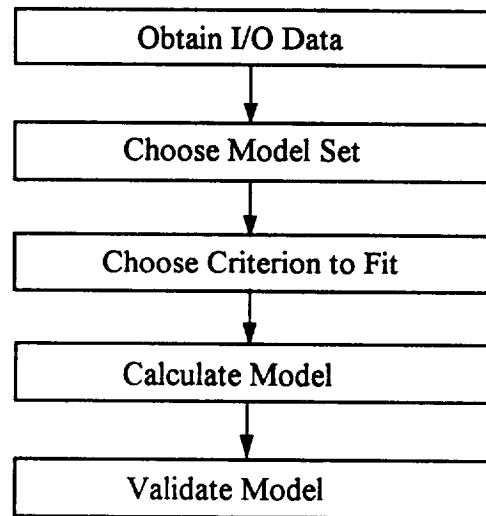
Figure 37. System Identification Process.

Model structures tested for the identification of the shoulder yaw, shoulder pitch, and elbow pitch joints include the autoregressive with extra input (ARX) model, the autoregressive moving average with extra input (ARMAX) model, the output error (OE) model, and the four-stage instrument variable (IV4) model forms. These model structures were selected to produce the best approximation for each joint's dynamic characteristics. During the parameter estimation and analysis procedures, the ARX and IV4 structures did

not produce consistent results, therefore, only results from the ARMAX and OE model structures will be shown. These results are consistent with the results obtained from the nonparametric tests performed earlier. The nonparametric estimation yielded considerable information about the noise dynamics of each joint which coincides with the fact that both ARX and IV4 model structures do not sufficiently characterize the noise dynamics.

For each HMTB joint, parametric techniques will be employed to determine the best model that fits several data sets. To perform this task, a transfer function that corresponds to the model will be obtained, residual analysis will be performed to determine the whiteness and independence of the model estimate's equation errors, and pole-zero plots will be shown to determine if the model estimate is stable. The model will be compared to the I/O data to determine if the estimate produces a proper fit. Next, cross-validation will be shown to determine if the model estimate can fit other data sets. The state-space representation of the best model estimate will be obtained. And finally, the linear combination of state-space representations will be determined to produce a multivariable state-space estimate of all three
joints.

Figure 38 shows the operator interface developed specifically for this thesis to perform nonparametric estimation and parametric evaluation of the HMTB joints. The algorithms used in the evaluation code utilize functions from the *MATLAB System Identification Toolbox (version 3)*.
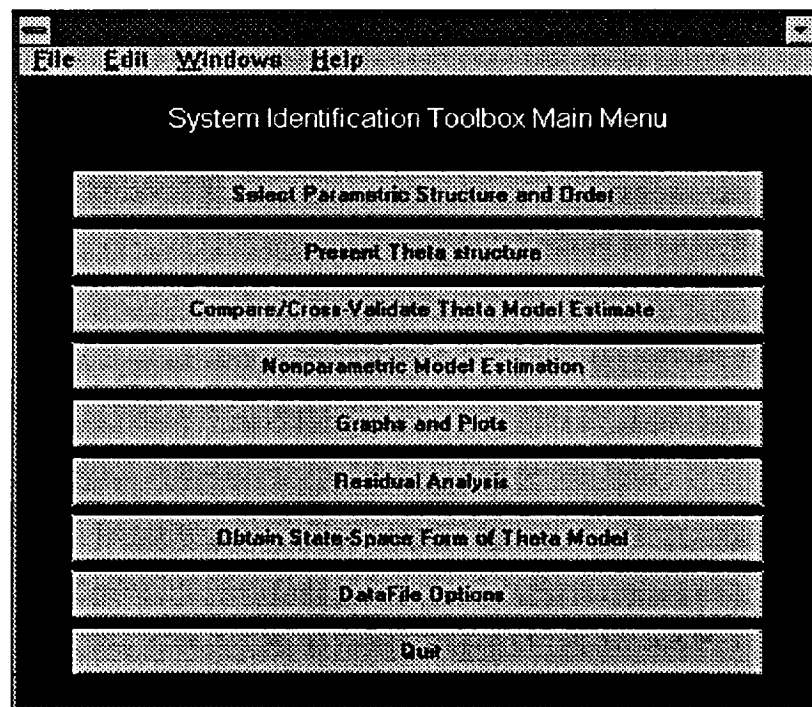

Figure 38. System Identification Operator Interface.

2. Parametric Black-Box Models

Most n-th order systems can be described with a simple, linear difference equation

$$y(t) + a_1 y(t-1) + \ldots + a_{na} y(t-n_a) =$$

$$b_1 u(t-1) + \ldots + b_{nb} u(t-n_b) + \mathcal{E}(t). \tag{4.1}$$

The disturbance term $\mathcal{E}(t)$ serves as a direct error in the difference equation. This general model is generally referred to as an equation error model. The linear block-box models used in this section serve to estimate the general equation error model. The equation error dynamical model may also be described as

$$y(t) = G(q, \theta) u(t) + H(q, \theta) \mathcal{E}(t) \tag{4.2}$$

where

$G(q)$ is the system transfer function,

$H(q)$ is the disturbance transfer function,

$\mathcal{E}(t)$ is the disturbance,

θ is the parameter vector, and

q is the delay operator.

The ARMAX linear block-box model structure corresponds to setting

$$G(q) = q^{-nk} \frac{B(q)}{A(q)} \quad \text{and} \quad H(q) = \frac{C(q)}{A(q)} \tag{4.3}$$

where

$$C(q) = 1 + c_1 q^{-1} + c_2 q^{-2} + \ldots + c_{nc} q^{-nc}.$$

The ARMAX structure gives considerable freedom in describing the properties of the disturbance term by estimating the error equation as a moving average of white noise. This structure describes the system that has a common factor in the denominators of the $G(q)$ and $H(q)$ polynomials.

The output error (OE) model structure allows the transfer functions, $G(q)$ and $H(q)$, to be independently determined. That is, neither transfer function has a common polynomial description. The OE structure has the model form

$$y(t) = \frac{B(q)}{F(q)} u(t) + \mathcal{E}(t). \tag{4.4}$$

Both ARMAX and OE models structures are estimated using a prediction error method (PEM). The PEM is a modification of the least squares (LS) method. In the general LS method, the estimation procedure is performed by selecting the parameter vector θ that minimizes the loss function,

$$V(\theta) = \frac{1}{N}\sum_{t=1}^{N}\varepsilon^2(t). \tag{4.5}$$

The PEM enhances the LS approach by forming the residual $\varepsilon(t)$ as a difference between the measured output $y(t)$ and a prefiltered output prediction $\hat{y}(t|t-1;\theta)$, that is,

$$\varepsilon(t) = y(t) - \hat{y}(t|t-1;\theta) \tag{4.6}$$
where

$$\hat{y}(t|t-1;\theta) = H^{-1}(q^{-1};\theta)\,G^{-1}(q^{-1};\theta)u(t) + \{I - H^{-1}(q^{-1};\theta)\}y(t).$$

For a model estimate to correctly describe an unknown system, the residuals (equation errors) must be ideally white and independent of the input.

3. Identification of Shoulder Yaw Joint
A. Preliminary Model Estimates

Several ARX, ARMAX, IV4, and OE model structures were used to identify the dynamical characteristics of the shoulder yaw joint. Among these model structures, only the ARMAX and OE estimates exhibited a better fit among many data sets. Therefore, only ARMAX and OE estimates will be discussed. From the experiment tests, the shoulder yaw appeared to exhibit a more nonlinear response. This information quickly implies perhaps a higher order design to estimate this joint's response. Throughout the identification process, models selected have been those that were the simplest to obtain while yet maintaining stability and the best approximation to many data sets.

ARMAX

After several iterations, an ARMAX model containing five poles, two zeros, and two delays on the input was found to sufficiently characterize the shoulder yaw joint. The transfer function is expressed as

$$H(z) = \frac{0.003804\ z^3 + 0.003504\ z^2 - 0.004285\ z}{z^5 - 2.542\ z^4 + 2.367\ z^3 - 0.8523\ z^2 - 0.08044\ z + 0.1103}. \tag{4.7}$$

Prediction error analysis of the ARMAX estimate yielded residuals that were white and with a high degree of independence. Figure 39 shows the residuals of the ARMAX model estimate using the PRBS input signal. The first plot in Figure 40 shows the whiteness of the model's residuals (the autocorrelation of the residual) while the second (lower) plot shows the residual independence (the cross-correlation of the residual and the input) as a function of lag (delay). The dashed lines in each plot represent 99% confidence intervals. That is, if the curve in each plot goes significantly outside the confidence intervals, the model is not accepted as a good estimate.
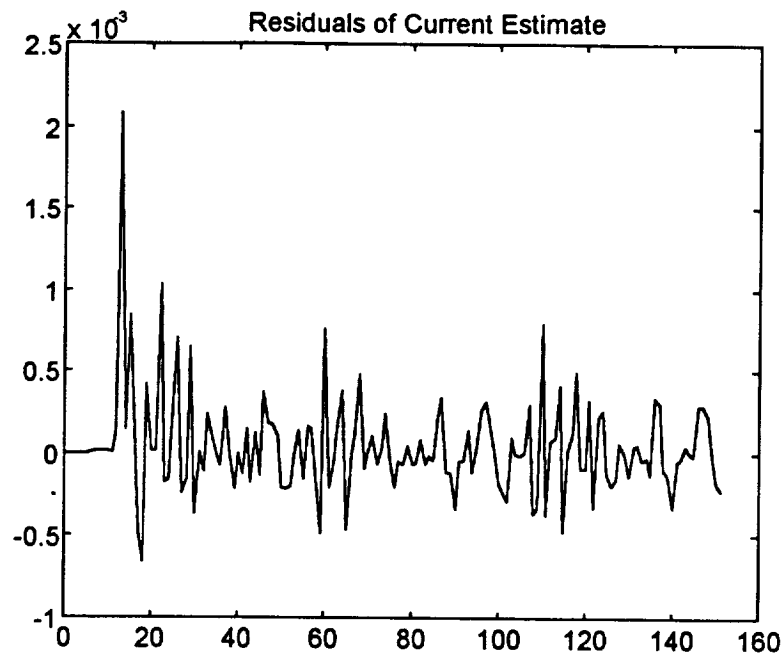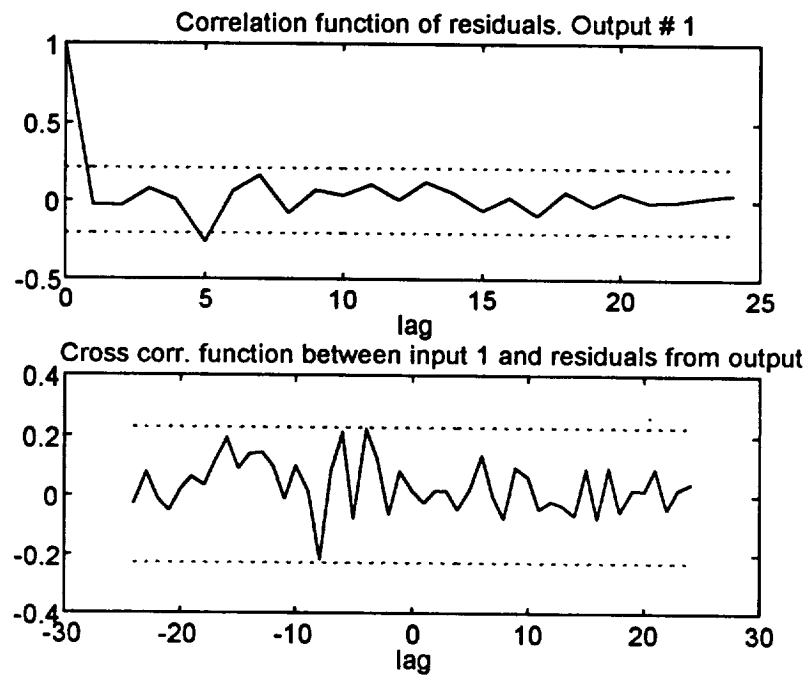
Figure 39. Shoulder Yaw ARMAX Residuals.

Figure 40. Shoulder Yaw ARMAX Residual Whiteness and Independence.

The pole-zero plot (Figure 41) displays the poles and zeros of the ARMAX model estimate. Since the poles of the discrete-time system are in the unit circle, the model is stable. The close pole and zero in the graph indicate a near pole-zero cancellation possibly indicating that the model order selected was too high. The other models tested without the close pole and zero produced estimates that did not sufficiently characterize the dynamics.

OUTPUT # 1 INPUT # 1
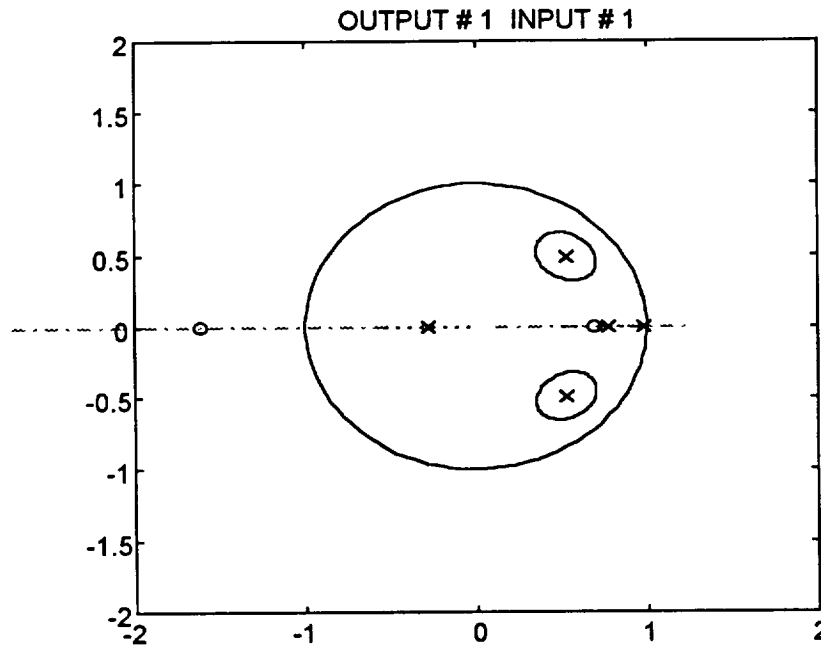
- Figure 41. Shoulder Yaw ARMAX Pole-Zero Plot.

The ARMAX model estimate was then compared to the data set that produces the model. Figure 42 shows a comparison of the estimated model output to the measured output. Even though the model didn't follow the PRBS data set very well, it showed the best flexibility in following many other data sets. Figure 43 shows the cross-validation of the ARMAX model estimate to the sum of sinusoids ten hertz input signal. Since cross-validation of a model estimate is a much harder task, the cross-validation of the model to various data sets weighed heavily in determining the best model estimate.
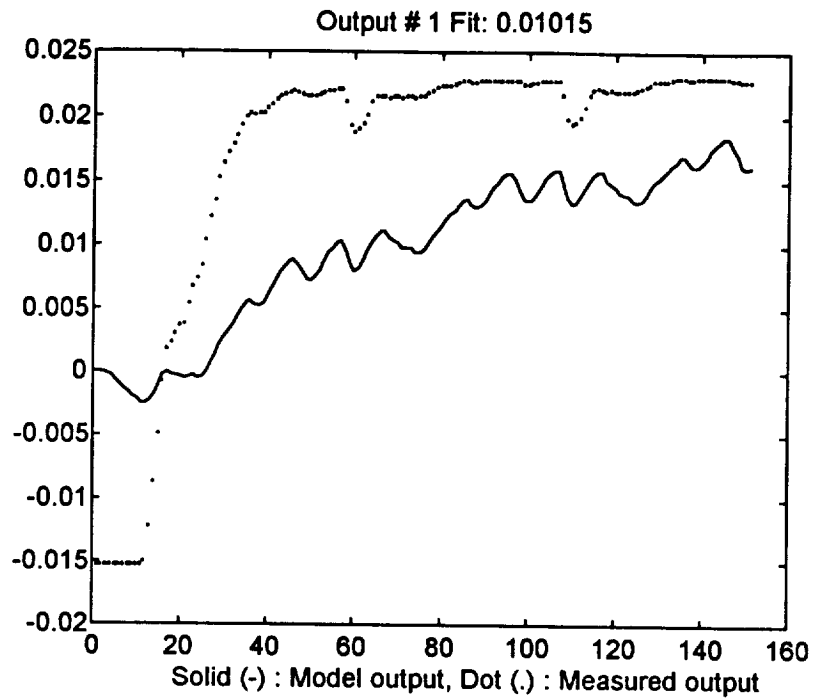
Figure 42. Shoulder Yaw ARMAX Output Comparison.
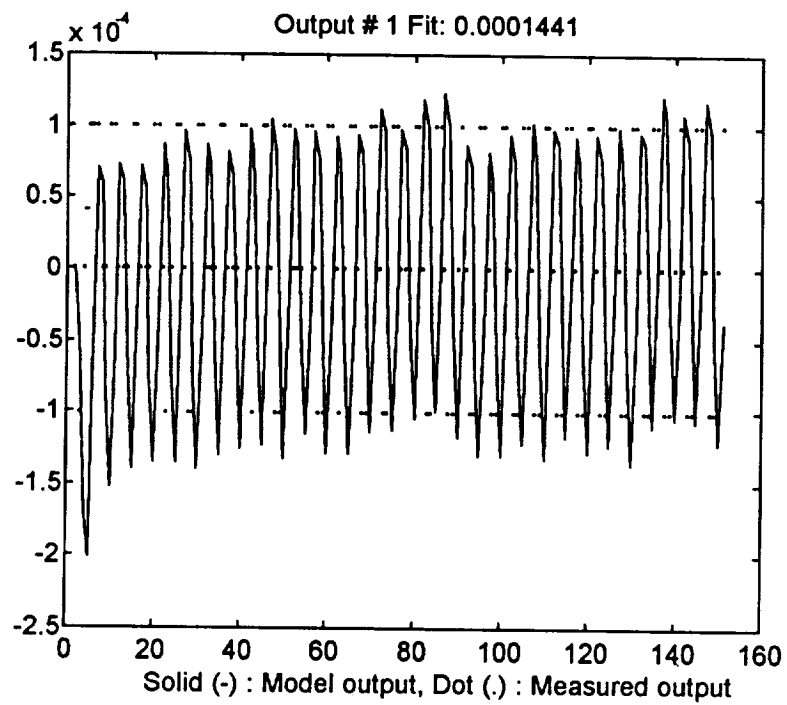
Figure 43. Shoulder Yaw ARMAX Cross-Validation.

OE

An OE model containing two poles, one zero, and two delays on the input also produced good results for the shoulder yaw joint. The transfer function for this OE estimate is

$$H(z) = \frac{0.0464\,z + 0.06144}{z^3 - 0.7501\,z^2 - 0.1815\,z}. \tag{4.8}$$

Prediction error analysis of this OE estimate yielded residuals that were not very white. This might be attributed to the fact that the OE structure focuses more on the dynamics G and less on the noise properties H. Figure 44 shows the residuals of the OE model estimate using the PRBS input signal. The first plot in Figure 45 shows the whiteness of the model's residuals (the autocorrelation of the residual) while the second (lower) plot shows the residual independence as a function of lag (delay). The cross-correlation of the OE residuals to the input signal shows slight independence for small positive and negative lags. Since the residual independence does not go significantly outside the confidence intervals, the OE model is accepted as a possible shoulder yaw estimate.
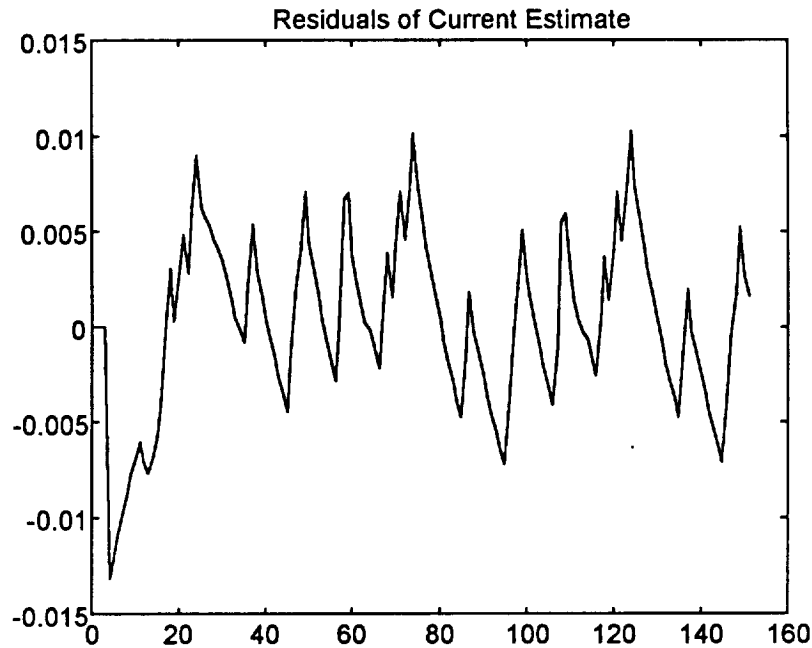
Figure 44. Shoulder Yaw OE Residuals.

The pole-zero plot (Figure 46) displays the poles and zeros of the OE model estimate. Since the poles of the discrete-time system are inside the unit circle, the model is stable. Various tests using a higher number of OE poles yielded an unstable system.

43
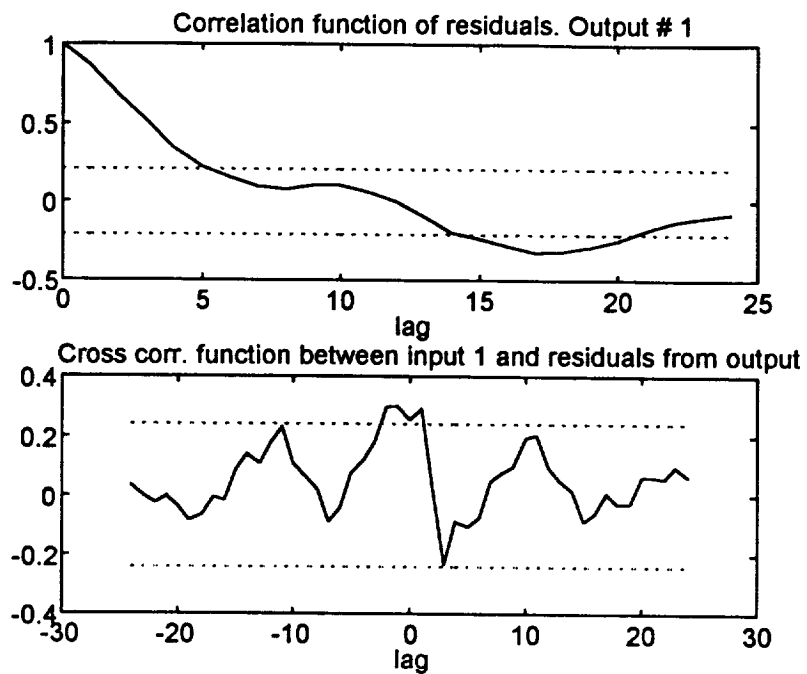
Figure 45. Shoulder Yaw OE Residual Whiteness and Independence.
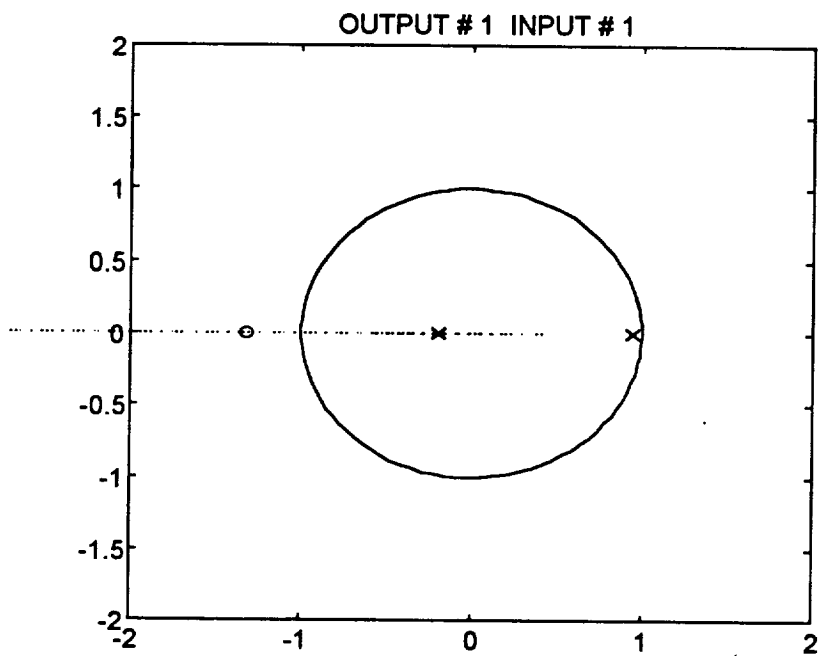
Figure 46. Shoulder Yaw OE Pole-Zero Plot.
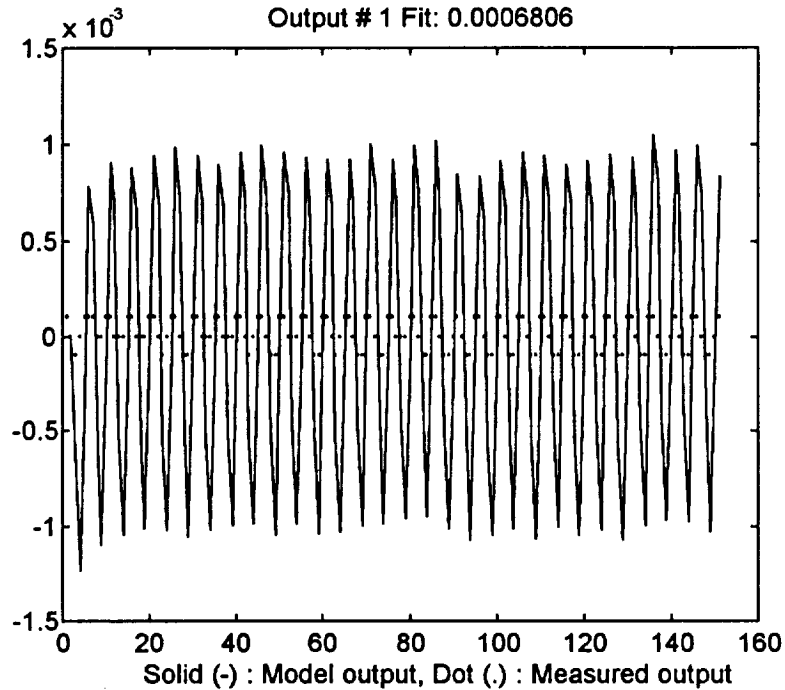
44
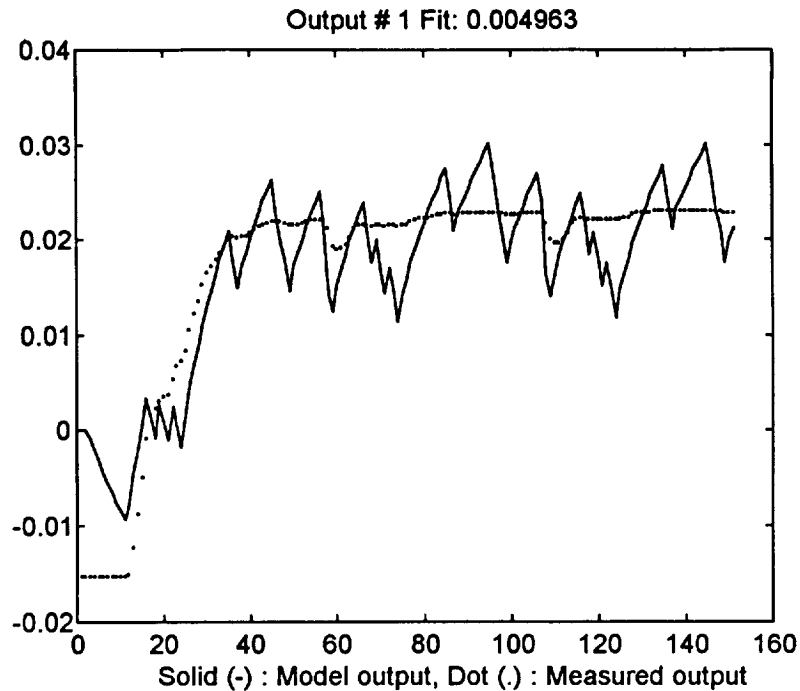
Figure 47. Shoulder Yaw OE Output Comparison.

Figure 48. Shoulder Yaw OE Cross-Validation.

The OE model estimate was then compared to the data set that produces the model (Figure 47). The OE model estimate only fitted the mean of the PRBS data rather than the peaks of the sequence. This fit is perhaps better than the ARMAX comparison, however, the OE showed poor flexibility in following other data sets. Figure 48 shows the cross-validation of the OE model estimate to the sum of sinusoids ten hertz input signal.

45

The OE estimate exhibited the correct frequency response, as seen by the zero crossing in Figure 48, but failed to match the peaks of the sequence. This response is due to the magnitude of the OE estimate being less than unity at the frequency of the input data. This OE response was typical to other data files.

B. Determination of Best Model Estimate

The ARMAX structure with five poles, two zeros, and two delays on the input was selected as the best linear approximation for the shoulder yaw dynamics in a localized region. Since the bode plots of the ARMAX estimate (Figure 49) showed comparable results to the OE and ARX estimates shown, the ARMAX model exhibited some of the true characteristics of the unknown system. The ARMAX estimate was selected because of the whiteness and independence of its residuals. Also, the cross-validation of the model to several data sets described a more flexible estimate. For these reasons, the ARMAX model was selected as the best estimate of the shoulder yaw joint.
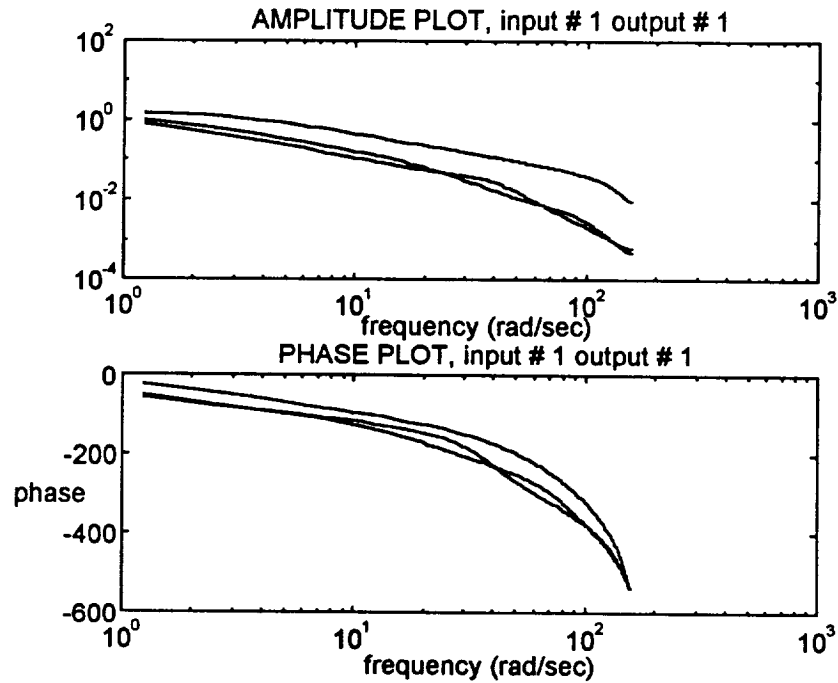
Figure 49. Bode Plots of the ARMAX, ARX, and OE Estimates.

C. SISO State-Space Estimate

The SISO state-space estimate for the ARMAX shoulder yaw joint is:

$$x(k + 1) = A_1 x(k) + B_1 u(k) + K_1 e(k) \tag{4.9}$$

$$y(k) = C_1 x(k) + D_1 u(k) + e(k)$$

where

46

$$
A_I = \begin{bmatrix} 2.5420 & 1.0000 & 0 & 0 & 0 \\ -2.3667 & 0 & 1.0000 & 0 & 0 \\ 0.8523 & 0 & 0 & 1.0000 & 0 \\ 0.0804 & 0 & 0 & 0 & 1.0000 \\ -0.1103 & 0 & 0 & 0 & 0 \end{bmatrix}, \qquad B_I = \begin{bmatrix} 0 \\ 0.0038 \\ 0.0035 \\ -0.0043 \\ 0 \end{bmatrix}
$$

$$
C_I = \begin{bmatrix} 1 & 0 & 0 & 0 & 0 \end{bmatrix}, \qquad D_I = 0,
$$

$$
K_I = \begin{bmatrix} 2.1470 \\ -2.4323 \\ 1.1597 \\ 0.0804 \\ -0.1103 \end{bmatrix}, \qquad \text{given } X0 = \begin{bmatrix} 0 \\ 0 \\ 0 \\ 0 \\ 0 \end{bmatrix}.
$$

4. Identification of Shoulder and Elbow Pitch Joints

The same model structures (ARX, ARMAX, IV4, and OE) and procedures used to identify the dynamical characteristics of the shoulder yaw joint were also used to identify parametric dynamic models for the shoulder pitch and elbow pitch joints. Plots and graphs from the shoulder pitch and elbow pitch joints are shown in Appendix A.2. Summary of the best model estimate for each joint follows:

Shoulder Pitch

The OE model containing two poles, one zero, and one delay on the input was selected as the best linear approximation for the shoulder pitch dynamics in a localized region. The transfer function for this OE estimate is

$$
H(z) = \frac{0.03459 \, z + 0.07584}{z^2 - 0.9776 \, z + 0.07922} . \tag{4.10}
$$

There are two primary reasons for selecting the OE estimate as the best dynamic approximation. First, the residuals were truly independent of the input which implies that the model is a very good approximation to the real joint dynamics. And second, the cross-validation of the model to several data sets described a more flexible model estimate. The SISO state-space estimate for the OE shoulder pitch joint is:

$$
x(k + 1) = A_2 x(k) + B_2 u(k) + K_2 e(k) \tag{4.11}
$$

$$
y(k) = C_2 x(k) + D_2 u(k) + e(k)
$$

where

$$A_2 = \begin{bmatrix} 0.9776 & 1.0000 \\ -0.0792 & 0 \end{bmatrix}, \quad B_2 = \begin{bmatrix} 0.0346 \\ 0.0758 \end{bmatrix}$$

$$C_2 = \begin{bmatrix} 1.0000 & 0 \end{bmatrix}, \quad D_2 = 0,$$

$$K_2 = \begin{bmatrix} 0 \\ 0 \end{bmatrix}, \quad \text{given } X0 = \begin{bmatrix} 0 \\ 0 \end{bmatrix}.$$

<u>Elbow Pitch</u>

An ARMAX model containing two poles, one zero, and two delays on the input was found to sufficiently characterize the dynamics of the elbow pitch joint. The transfer function for this model estimate is expressed as

$$H(z) = \frac{0.01237\,z + 0.0426}{z^3 - 1.488\,z^2 + 0.5435\,z}. \tag{4.12}$$

There are two primary reasons for selecting the ARMAX estimate as the best dynamic approximation. First, the residuals were whiter than the OE estimate indicating that the ARMAX appropriately modeled the noise characteristics of the joint. And second, the cross-validation of the model to several data sets described a more flexible model estimate. The SISO state-space estimate for the ARMAX elbow pitch joint is:

$$x(k+1) = A_3\,x(k) + B_3\,u(k) + K_3\,e(k) \tag{4.13}$$

$$y(k) = C_3\,x(k) + D_3\,u(k) + e(k)$$

where

$$A_3 = \begin{bmatrix} 1.4877 & 1.0000 & 0 \\ -0.5435 & 0 & 1.0000 \\ 0 & 0 & 0 \end{bmatrix}, \quad B_3 = \begin{bmatrix} 0 \\ 0.0124 \\ 0.0426 \end{bmatrix}$$

$$C_3 = \begin{bmatrix} 1.0000 & 0 & 0 \end{bmatrix}, \quad D_3 = 0,$$

$$K_3 = \begin{bmatrix} 1.4698 \\ -0.2739 \\ 0 \end{bmatrix}, \quad \text{given } X0 = \begin{bmatrix} 0 \\ 0 \\ 0 \end{bmatrix}.$$

48

5. State-Space Multivariable Representation

Each SISO state-space estimate previously determined was identified about an operating point. For the purpose of this identification, the operating point was chosen to coincide with the insertion point trajectory vector for the RPCM ORU exchange task. With each input signal producing only small deviations around the operating point, a local neighborhood was defined about the RPCM insertion point for which each identified SISO model is valid. This is the essence of linear approximation of a nonlinear model [18].

The following three-joint, linear, multivariable state-space estimate was formed using each joint's best dynamic SISO representation:

$$x(k+1) = A\,x(k) + B\,u(k) + K\,e(k) \tag{4.14}$$

$$y(k) = C\,x(k) + D\,u(k) + e(k)$$

where

$$A = \begin{bmatrix} A_1 & 0 & 0 \\ 0 & A_2 & 0 \\ 0 & 0 & A_3 \end{bmatrix}, \qquad B = \begin{bmatrix} B_1 & 0 & 0 \\ 0 & B_2 & 0 \\ 0 & 0 & B_3 \end{bmatrix},$$

$$C = \begin{bmatrix} C_1 & 0 & 0 \\ 0 & C_2 & 0 \\ 0 & 0 & C_3 \end{bmatrix}, \qquad D = \begin{bmatrix} D_1 & 0 & 0 \\ 0 & D_2 & 0 \\ 0 & 0 & D_3 \end{bmatrix},$$

$$K = \begin{bmatrix} K_1 & 0 & 0 \\ 0 & K_2 & 0 \\ 0 & 0 & K_3 \end{bmatrix}.$$

The matrices A_n, B_n, C_n, D_n, and K_n where n = 1, 2, or 3 refer to matrices previously determined in equations 4.9, 4.11, and 4.13. This multivariable state-space estimate will be used for comparison purposes. The actual RPCM data set along with several MIMO data sets will be used to cross-validate this multivariable estimate.

V. Parametric Model Estimation:
Observer/Kalman Filter Identification

Among alternate system identification procedures are the ones based on system realization theory. One such technique, used in the identification of space structures, is Observer/Kalman Filter Identification (OKID). This technique computes Markov parameters from pulse system response histories using an asymptotically stable observer to form a stable discrete state-space model. This chapter will briefly discuss the OKID technique provided in the *System/Observer/Controller Identification Toolbox (SOCIT)* by Jer-Nan Juang, Lucas G. Horta, and Minh Phan [19]. Residual analysis and cross-validation procedures will be used to identify the best state-space models for the HMTB joints.

1. OKID Background and Procedure

When a pulse sequence is used as input into the discrete-time state-space dynamic equation

$$x(k + 1) = A x(k) + B u(k)$$ (5.1)

$$y(k) = C x(k) + D u(k),$$

the resulting series of equations can be formed into a pulse-response matrix Y, that is,

$$Y = [D \quad CB \quad CAB \quad ..... \quad C A^{k-1}B].$$ (5.2)

The elements of the matrix Y are known as the system Markov parameters. System realization involves determining the matrices A, B, C, and D from the system Markov parameters to satisfy the state and measurement equations (5.1) [8]. Minimum realization theory, attributed to Ho and Kalman [12], determines a model with the smallest state-space dimension among all realizable systems. The procedure starts by forming the generalized Hankel matrix composed of Markov parameters in the following manner:

$$H(k-1) = \begin{bmatrix} Y_k & Y_{k+1} & .. & Y_{k+\beta-1} \\ Y_{k+1} & Y_{k+2} & .. & Y_{k+\beta} \\ \vdots & \vdots & . & \vdots \\ Y_{k+\alpha-1} & Y_{k+\alpha} & .. & Y_{k+\alpha+\beta-2} \end{bmatrix}.$$ (5.3)

If the number of rows α and the number of columns β are greater than the order of the system, then the Hankel matrix is of rank n. This realization algorithm extracts linear state-space matrix components from noise-free data.

For noisy input/output sequences, the Eigensystem Realization Algorithm (ERA) produces better results [8]. By deleting specific rows and columns of the Hankel matrix, ERA forms a block data matrix composed of strongly measured Markov sequence components. A minimum realization may be obtained by factorization of the block data

matrix using singular value decomposition. The order of the identified system is determined by selecting the number of significant singular values.

Observer/Kalman Filter Identification is determined by inserting an observer into the discrete-time state-space dynamic equation (5.1) to form the discrete-time state-space observer model

$$x(k+1) = \overline{A} \, x(k) + \overline{B} \, v(k) \tag{5.4}$$

$$y(k) = C \, x(k) + D \, u(k),$$

where

$$\overline{A} = A + GC,$$

$$\overline{B} = [\, B + GD \quad -G \,], \text{ and}$$

$$v(k) = \begin{bmatrix} u(k) \\ y(k) \end{bmatrix}.$$

When a pulse sequence is used as input into the observer model (5.4), the following observer Markov parameters may be computed:

$$\overline{Y} = [\, D \quad C\overline{B} \quad C\overline{A}\,\overline{B} \quad ..... \quad C\,\overline{A}^{k-1}\overline{B} \,]. \tag{5.5}$$

The OKID technique then computes the system Markov parameters from the observer Markov parameters for minimum realization of a state-space model estimate. It is obvious from (5.5) that the matrices A, B, C, and D are embedded in the observer Markov parameters. Since the observer gain G may be arbitrarily chosen, the OKID routine creates a deadbeat observer by simply placing all the eigenvalues of $\overline{A}$ at the origin producing an asymptotically stable observer. Setting G to be the deadbeat observer gain allows for a minimum number of Markov parameters to describe the input/output relationship of a system [8].

Juang [8] describes the relationship between the state-space observer model and the Kalman filter equation

$$\hat{X}(k+1) = A\hat{X}(k) + B\,u(k) + K\mathcal{E}_r(k) \tag{5.6}$$

$$\hat{y}(k) = C\hat{X}(k) + D\,u(k),$$

where

$\hat{X}(k)$ is the estimated state,

$\hat{y}(k)$ is the estimated measurement,

K is the Kalman filter gain, and

$\mathcal{E}_r(k)$ is the residual defined as the difference $y(k) - \hat{y}(k)$.
The observer gain is said to be the steady-state Kalman filter gain

$$K = -G \tag{5.7}$$

in theory if the residuals are identically zero, $\mathcal{E}_r(k) = 0$, and the data length is sufficiently long to produce negligible truncation error. Theoretical background of the OKID technique is found in the text *Applied System Identification* by Jer-Nan Juang [8].

For each joint, system and observer parameters will first be determined. Next, the associated prediction errors will be computed. The Hankel matrix will be shown for proper order selection. After selecting the system order from the Hankel singular values, the state-space estimate will be realized. This realization will also yield the Kalman filter gain which for the purposes of this investigation will be approximated to the observer gain since each estimate will be selected to minimize the residuals and the arm will be operated in a localized region to minimize system nonlinearities. Each model estimate will be compared to the data set that produced the model as well as cross-validated to another data set. A three-joint multivariable state-space model will be determined from the three SISO state-space estimates.

2. Identification of Shoulder Yaw Joint
A. Determine Markov Parameter Set

An upper bound for the OKID model order must first be specified to compute an estimate. Using a fifth order system as the upper bound, five independent observer parameters were initially computed to identify the shoulder yaw state-space model using the PRBS input/output data. The system and observer Markov parameters for the shoulder yaw joint are shown in Figure 50. As seen in Figure 50, the rate of decay for the observer parameters is much larger than that for the system Markov parameters. This demonstrates the advantage of the deadbeat observer in minimizing the number of pulse response samples used to realize the state-space equation [8]. The relatively high number of independent Markov parameters shown in the plot indicates that the shoulder yaw joint exhibits relatively significant nonlinear characteristics.

Pulse Response Estimate of System

Pulse Response Estimate of Observer
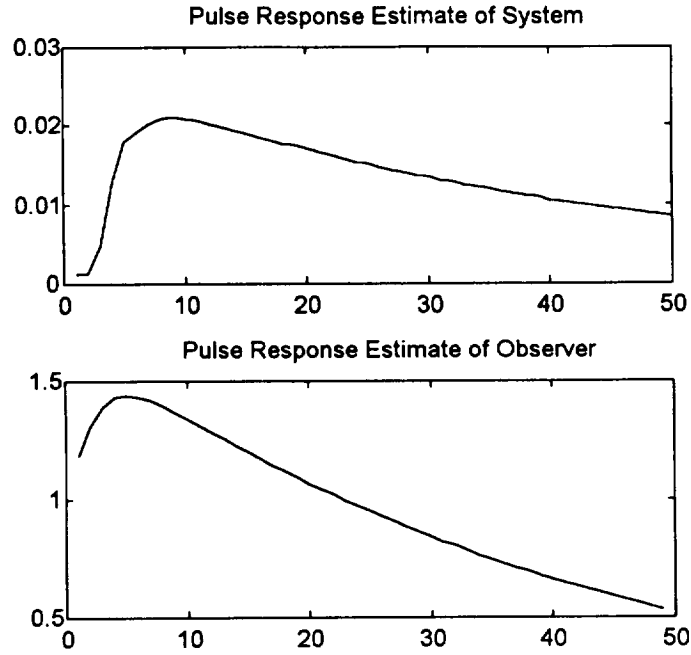
Figure 50. Shoulder Yaw System and Observer Markov Parameters.

B. OKID State-Space Estimate

The normalized prediction errors associated with the independent observer parameters and the input data file are shown in Figure 51. The lower plot in Figure 51 shows the variance of each observer parameter with the measured data. A smoothing error is also plotted next to each variance. Using the Hankel matrix of singular values (Figure 52), a system order of two was selected for minimum realization of the shoulder yaw joint, that is, the second-order model obtained described 99.8691% of the test data.
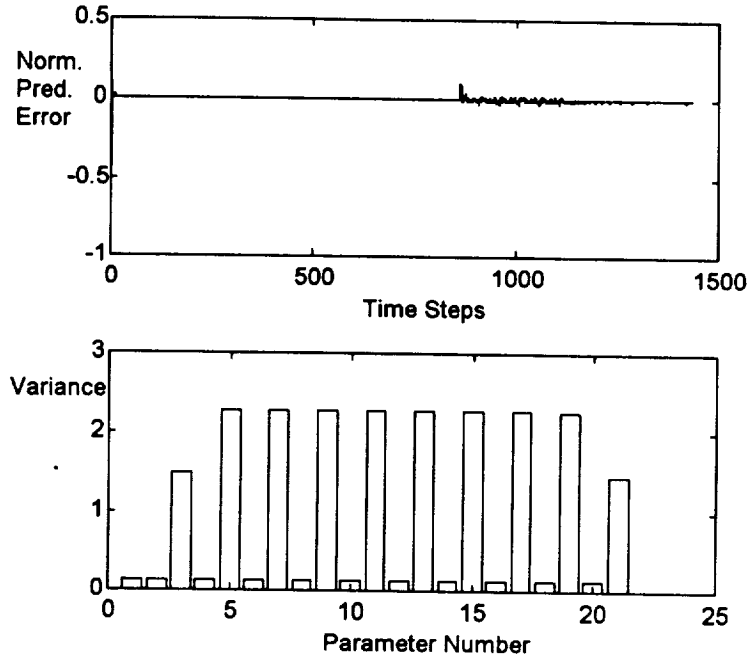
Figure 51. Shoulder Yaw Output Prediction Errors.
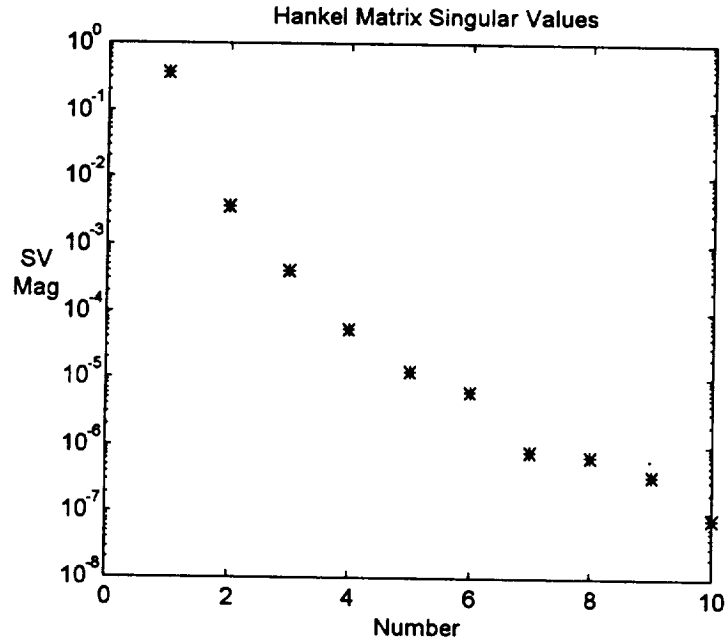
Figure 52. Shoulder Yaw Hankel Matrix.

The following discrete-time state-space observer model has been realized for the shoulder yaw joint:

$$x(k + 1) = (A_1 + G_1C_1) x(k) + [B_1 + G_1D_1 \quad -G_1] v(k) \tag{5.8}$$

$$y(k) = C_1 x(k) + D_1 u(k),$$

54

where

$$A_l = \begin{bmatrix} .99487 & .02896 \\ -.15355 & .55941 \end{bmatrix}, \qquad B_l = \begin{bmatrix} 2.7065 \\ 12.366 \end{bmatrix},$$

$$C_l = \begin{bmatrix} .004706 & -.001125 \end{bmatrix}, \qquad D_l = 0.000714,$$

$$G_l = \begin{bmatrix} -276.41 \\ -123.20 \end{bmatrix}, \qquad \text{and} \quad v(k) = \begin{bmatrix} u(k) \\ y(k) \end{bmatrix}.$$

C. Analysis

The bode plots of the discrete-time state-space model estimate is shown in Figure 53. The frequency range of this estimate seems to be valid for extremely low frequencies less than 1 Hz.
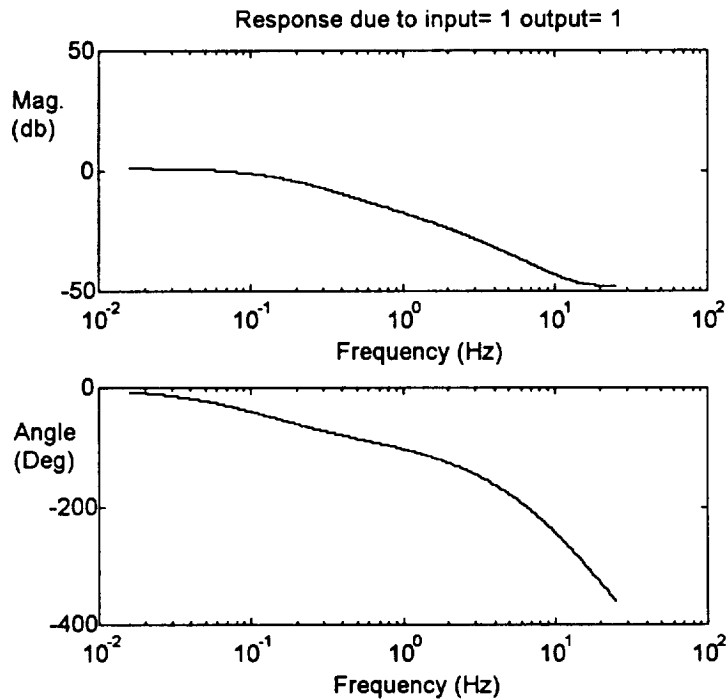
Figure 53. Shoulder Yaw Bode Plots of State-Space Estimate.

To validate the state-space model estimate, the model output was compared to the data set that produced the model. Figure 54 shows the predicted state-space output compared to the measured output. As seen in the graph, the second-order model estimate predicts the measured output extremely well.

Output Number = 1
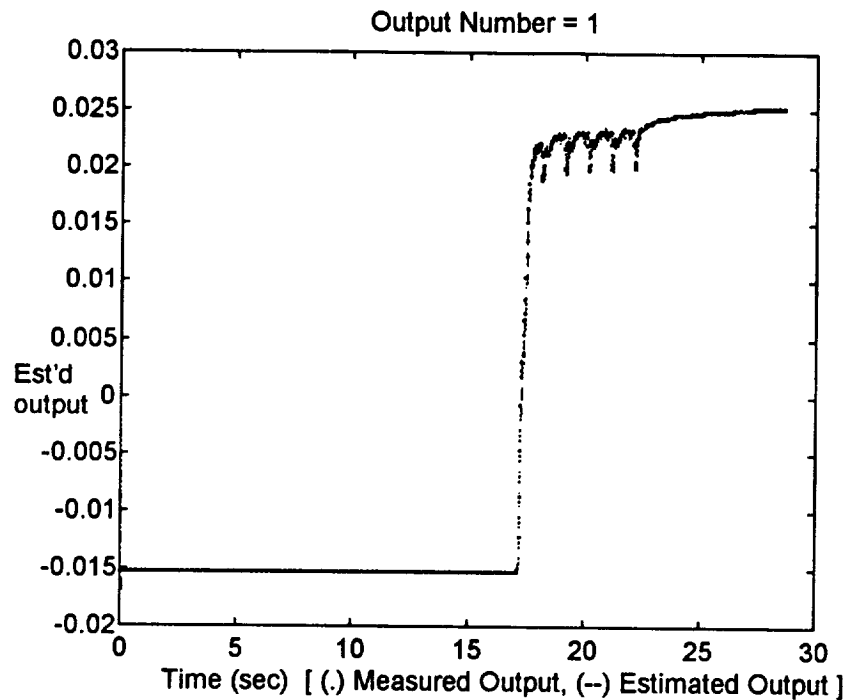
Figure 54. Shoulder Yaw Predicted Versus Measured Output.

Cross-validating the shoulder yaw model OKID estimate with the five to ten Hertz linearly swept chirp signal (Figure 55) produced good results. Residuals for the cross-validation were very low. This implies that the deadbeat observer can possibly be considered the Kalman Filter gain according to 5.7.

Output Number = 1
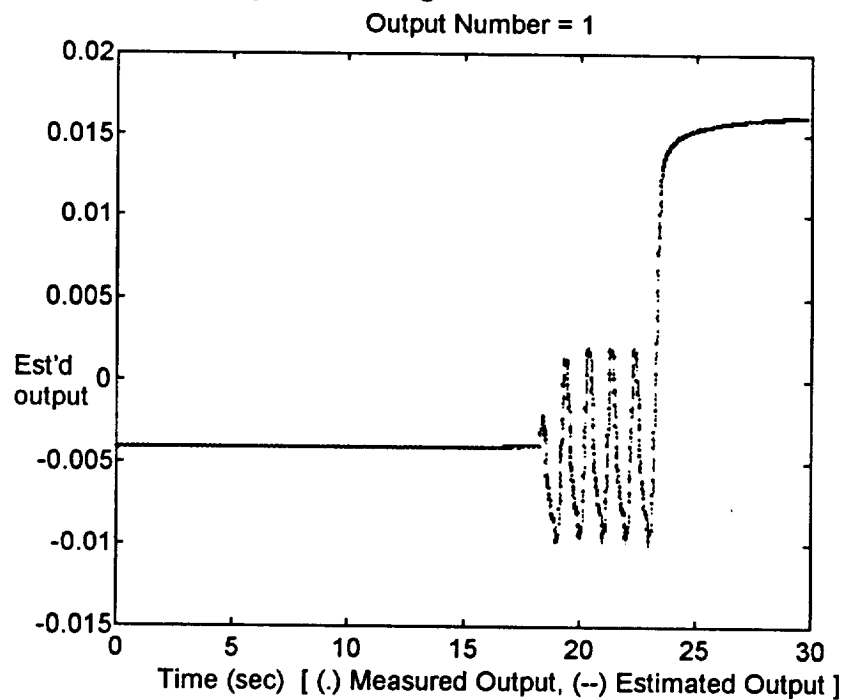
Figure 55. Shoulder Yaw Chirp Cross-Validation.

It should be noted that numerous iterations were performed to obtain this state-space model estimate. In the iterations where the data was not detrended, the best estimate for minimum realization was a fourth-order system. This higher-order system produced extremely poor residuals and therefore was rejected as the shoulder yaw estimate. The only advantage of the fourth-order system was the minimum number of independent observer Markov parameters needed to realize the state-space dynamic equation.

3. Identification of Shoulder and Elbow Pitch Joints

The same OKID procedures used to identify the dynamic characteristics of the shoulder yaw joint were also used to identify parametric dynamic models for the shoulder pitch and elbow pitch joints. Plots and graphs from the shoulder pitch and elbow pitch joints are shown in Appendix A.3. Summary of both model estimates follows:

Shoulder Pitch

A system order of two was selected for minimum realization of the shoulder pitch joint. More specifically, the second-order model obtained described 96.1075 % of the test data. The following discrete-time state-space observer model has been realized for the shoulder pitch joint:

$$x(k+1) = (A_2 + G_2 C_2) x(k) + [B_2 + G_2 D_2 \quad -G_2] v(k) \tag{5.9}$$

$$y(k) = C_2 x(k) + D_2 u(k),$$

where

$$A_2 = \begin{bmatrix} .90891 & .10801 \\ -.35206 & .33925 \end{bmatrix}, \qquad B_2 = \begin{bmatrix} 6.881 \\ 11.762 \end{bmatrix},$$

$$C_2 = \begin{bmatrix} .014742 & -.0065875 \end{bmatrix}, \qquad D_2 = 0.010405,$$

$$G_2 = \begin{bmatrix} -65.283 \\ 22.597 \end{bmatrix}, \qquad \text{and} \qquad v(k) = \begin{bmatrix} u(k) \\ y(k) \end{bmatrix}.$$

Elbow Pitch

A system order of two was selected for minimum realization of the elbow pitch joint. More specifically, the second-order model obtained described 98.8832 % of the test data. The following discrete-time state-space observer model has been realized for the elbow pitch joint:

$$x(k+1) = (A_3 + G_3 C_3) x(k) + [B_3 + G_3 D_3 \quad -G_3] v(k) \tag{5.10}$$

$$y(k) = C_3 x(k) + D_3 u(k),$$

where

$$A_3 = \begin{bmatrix} .94738 & .077488 \\ -.27646 & .517280 \end{bmatrix}, \qquad B_3 = \begin{bmatrix} 4.7407 \\ 11.0670 \end{bmatrix},$$

$$C_3 = \begin{bmatrix} .013258 & -.0059914 \end{bmatrix}, \qquad D_3 = 0.0032941,$$

$$G_3 = \begin{bmatrix} -77.049 \\ 11.586 \end{bmatrix}, \qquad \text{and} \qquad v(k) = \begin{bmatrix} u(k) \\ y(k) \end{bmatrix}.$$

Though higher order models may have produced better fits in reducing the residuals, it was more advantageous to minimize the system order thus reducing the complexity of both state-space dynamic estimates.

4. State-Space Multivariable Representation

Each SISO state-space estimate previously determined was identified about the insertion point for the RPCM ORU exchange task. With each input signal producing only small deviations around the operating point, a local neighborhood was defined about the RPCM insertion point for which each identified SISO model is valid. The following three-joint, linear, multivariable state-space estimate was formed using the dynamic SISO state-space representation for each joint:

$$x(k+1) = A x(k) + B u(k) + K e(k) \tag{5.11}$$

$$y(k) = C x(k) + D u(k) + e(k)$$

where

$$A = \begin{bmatrix} A_1 & 0 & 0 \\ 0 & A_2 & 0 \\ 0 & 0 & A_3 \end{bmatrix}, \qquad B = \begin{bmatrix} B_1 & 0 & 0 \\ 0 & B_2 & 0 \\ 0 & 0 & B_3 \end{bmatrix},$$

$$C = \begin{bmatrix} C_1 & 0 & 0 \\ 0 & C_2 & 0 \\ 0 & 0 & C_3 \end{bmatrix}, \qquad D = \begin{bmatrix} D_1 & 0 & 0 \\ 0 & D_2 & 0 \\ 0 & 0 & D_3 \end{bmatrix}, \qquad K = \begin{bmatrix} K_1 & 0 & 0 \\ 0 & K_2 & 0 \\ 0 & 0 & K_3 \end{bmatrix}.$$

The matrices A_n, B_n, C_n, D_n, and K_n where n = 1, 2, or 3 refer to matrices previously determined in equations 5.8, 5.9, and 5.10. This multivariable state-space estimate will be used for comparison purposes. The actual RPCM data set along with several MIMO data sets will be used to cross-validate this multivariable estimate.

VI. Comparison of Identified Models

This chapter will compare the multivariable state-space model estimate obtained using prediction error techniques within Lennart Ljung's *System Identification Toolbox* and the multivariable state-space model estimate obtained using the Observer/Kalman Filter identification (OKID) technique provided in the *System/Observer/Controller Identification Toolbox (SOCIT)* by Jer-Nan Juang, Lucas G. Horta, and Minh Phan. Frequency plots and pole/zero maps for each estimate will be shown. Both multivariable estimates will be compared to data sets obtained from an RPCM experiment and a MIMO experiment using the chirp signal. Fit comparisons and residual analysis will be performed for each state-space estimate.

1. Identified Model Forms

The identification techniques investigated and described in the previous chapters represent parametric models of the form

$$y(t) = G(q)u(t) + v(t) \qquad (6.1)$$

where

$G(q)$ is the open-loop transfer function, and
$v(t)$ represents the disturbances.

This linear equation attempts to describe the open-loop dynamic characteristics of each of the three HMTB joints with additive disturbances. It should be noted that this dynamic equation is, in essence, an open-loop representation of the actual closed-loop dynamical implementation for each joint. This implies that the actual closed-loop dynamics will be embedded within the open-loop description of each joint. For high noise-to-signal ratios in the I/O time histories of each joint, the disturbances may be represented as

$$v(t) = H(q)e(t) \qquad (6.2)$$

where

$H(q)$ is the disturbance dynamics, and
$e(t)$ represents white noise.

In the *System Identification Toolbox*, prediction error techniques were used to determine ARMAX and OE black-box model structures for each joint. The ARMAX structure forms the joint dynamics according to the block diagram shown in Figure 56. The OE structure differs from the ARMAX structure by allowing the disturbances (noise) to go unfiltered as shown in Figure 57. The parametric black-box model developed for each joint was then converted to a SISO state-space estimate.
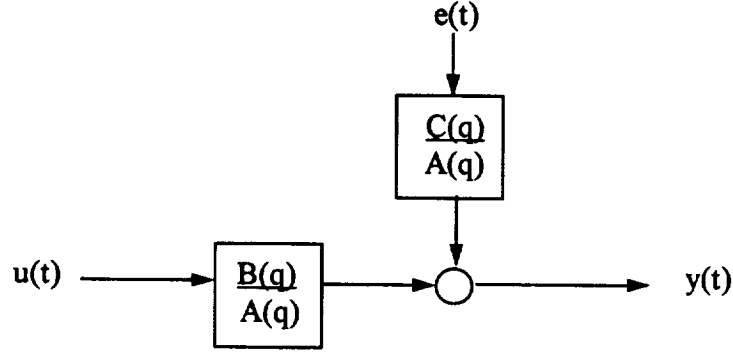
Figure 56. ARMAX Structure Block Diagram.
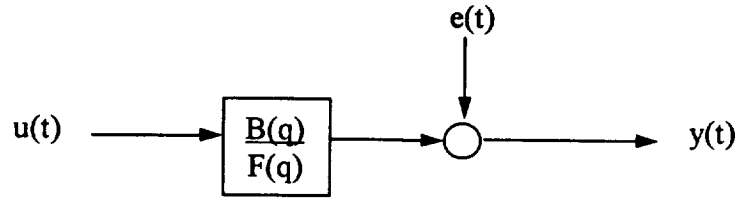
Figure 57. OE Structure Block Diagram.

A linear combination of the SISO state-space estimates were used to develop the multivariable state-space model. Linearization of the HMTB arm was performed by allowing only small perturbations in each joint's input signal to produce a localized region. The multivariable estimate obtained using prediction error techniques described the dynamics in the flexible innovations discrete-time state-space model form

$$x(k+1) = A x(k) + B u(k) + K e(k) \tag{6.3}$$

$$y(k) = Cx(k) + D u(k) + e(k).$$

The Observer/Kalman Filter Identification (OKID) technique identifies the dynamic characteristics of each joint using a discrete-time observer model of the form

$$\hat{X}(k+1) = A \hat{X}(k) + B u(k) - G\mathcal{E}(k) \tag{6.4}$$

$$y(k) = C \hat{X}(k) + D u(k) + \mathcal{E}(k).$$

where

$\hat{X}(k)$ is the estimate of state $x(k)$, and

$\mathcal{E}(k) = y(k) - \hat{y}(k)$.

It should be noted that the observer G can only be equated to the steady-state Kalman Filter gain K if and only if the residuals $\mathcal{E}(k)$ are white, zero mean and Gaussian [8]. In the following comparisons, the identified observer is not the Kalman Filter gain.

The computed observer G simply minimizes the residuals due to nonlinearities in each joint, non-whiteness of the noise processes, and correlation effects between the residual and the input signal.

Both multivariable model estimates will be compared using equivalent state-space representations, that is $K = -G$ where K in this case is simply a residual filter. For notation purposes, the multivariable model identified using prediction error techniques will be called the SysID model and the model identified using the Observer/Kalman Filter Identification (OKID) technique will be called the OKID model.

2. Transfer Function Analysis

The transfer function $G(q)$ from equation 6.1 may expressed in terms of the state-space matrices A, B, C, and D as

$$G(q) = C(qI - A)^{-1}B + D. \qquad (6.5)$$

Bode plots for the SysID MIMO model shown in Figures 58 - 60 describe the frequency and phase response characteristics of the shoulder yaw, shoulder pitch, and elbow pitch joints, respectively.
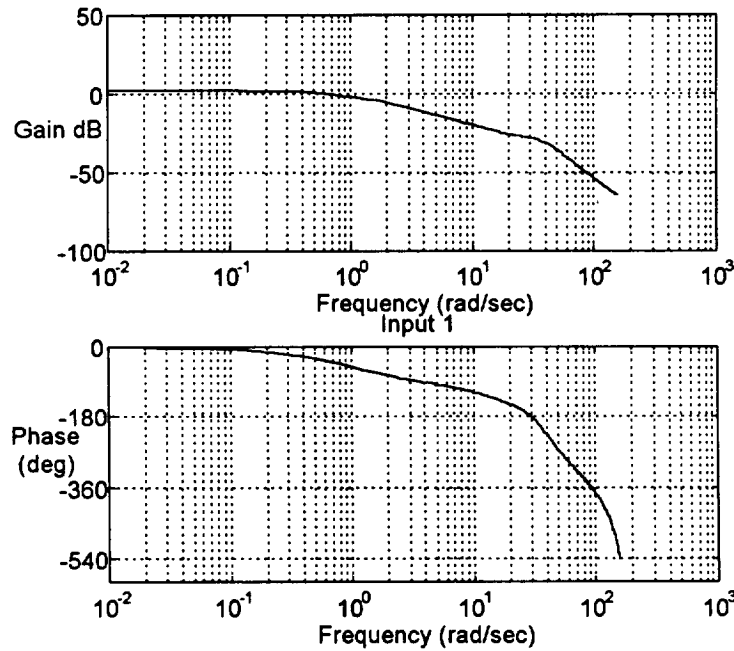
Figure 58. SysID Shoulder Yaw Bode Plots.
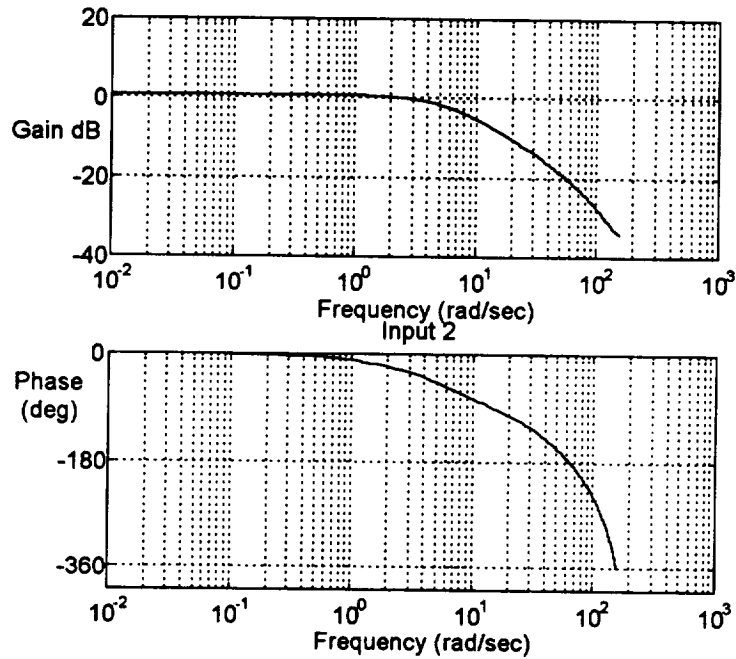
Figure 59. SysID Shoulder Pitch Bode Plots.
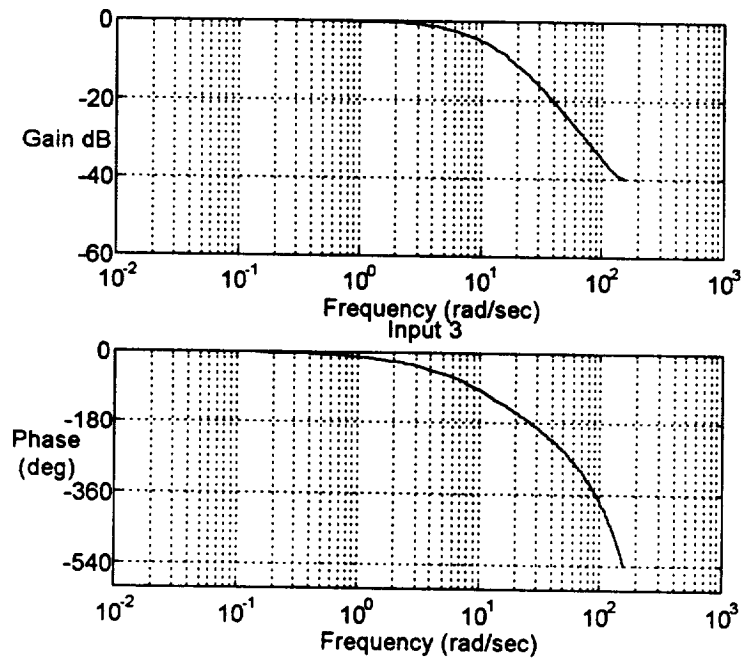
Figure 60. SysID Elbow Pitch Bode Plots.

Bode plots for the OKID MIMO model shown in Figures 61 - 63 describe the frequency and phase response characteristics of the shoulder yaw, shoulder pitch, and elbow pitch joints, respectively. As seen in the bode plots (Figures 58 - 63), the OKID model and the SysID model produced comparable results indicating that both techniques captured true frequency characteristics of each HMTB joint.
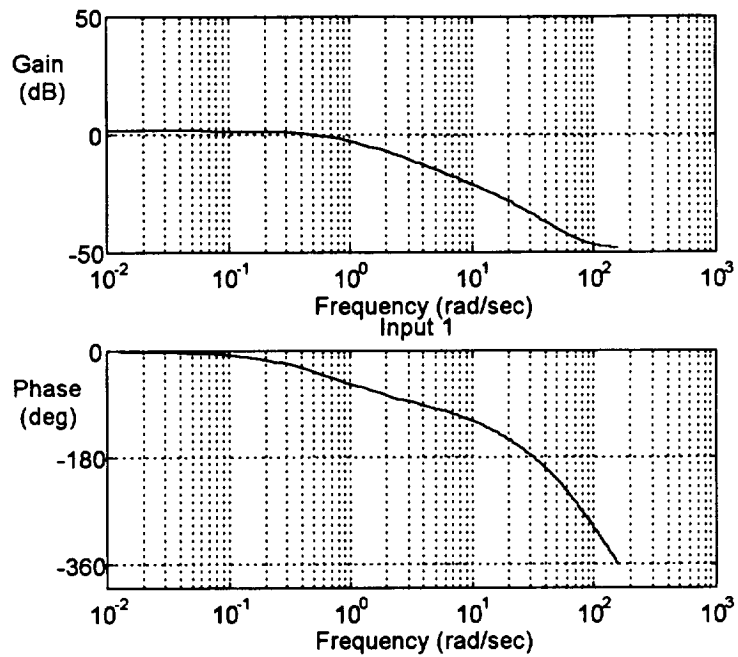
Figure 61. OKID Shoulder Yaw Bode Plots.
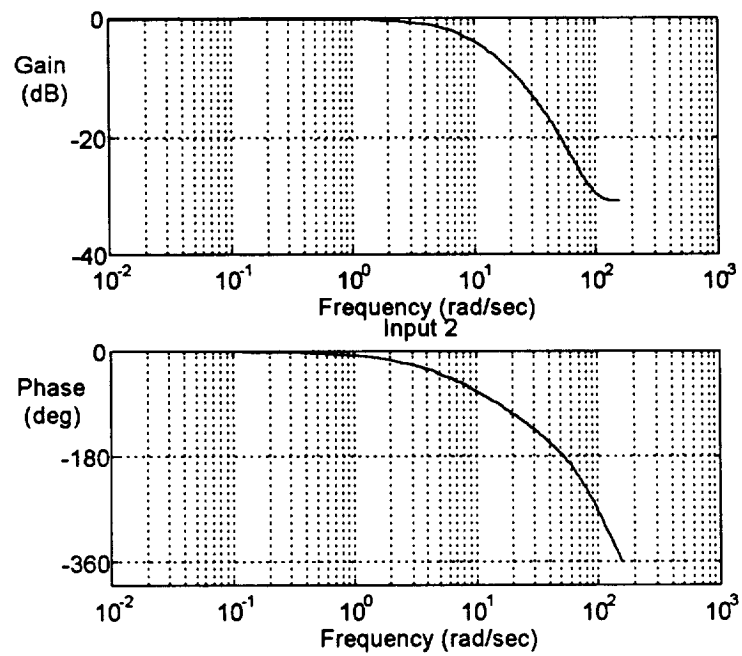
Figure 62. OKID Shoulder Pitch Bode Plots.
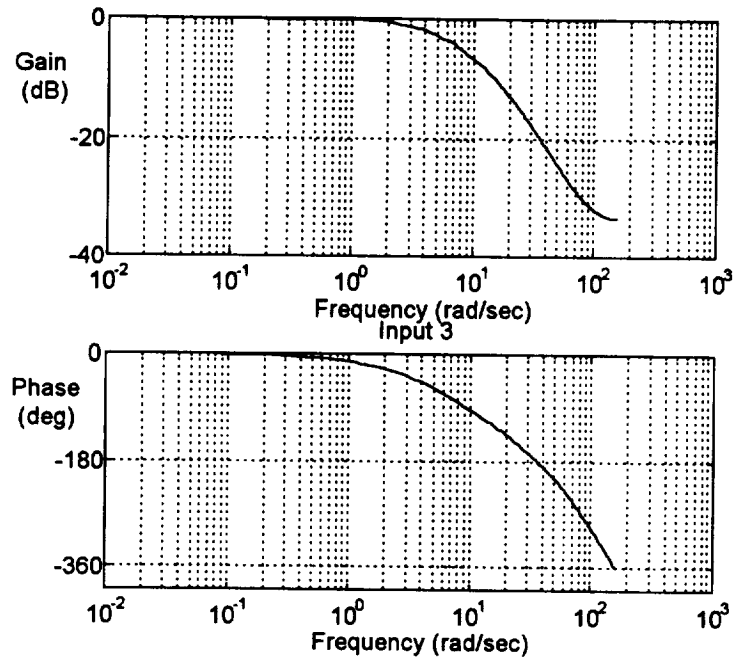
Figure 63. OKID Elbow Pitch Bode Plots.

3. Pole/Zero Map

Figure 64 shows the eigenvalues and transmission zeros of the SysID multivariable model. The eigenvalues (roots of the characteristic equation) represent the poles of the discrete-time MIMO estimate. Since the magnitude of the eigenvalues are less than unity, the discrete-time model is considered stable. The eigenvalue-transmission zero combination near the origin indicates that the SysID model may be unnecessarily complex to describe the HMTB joints.
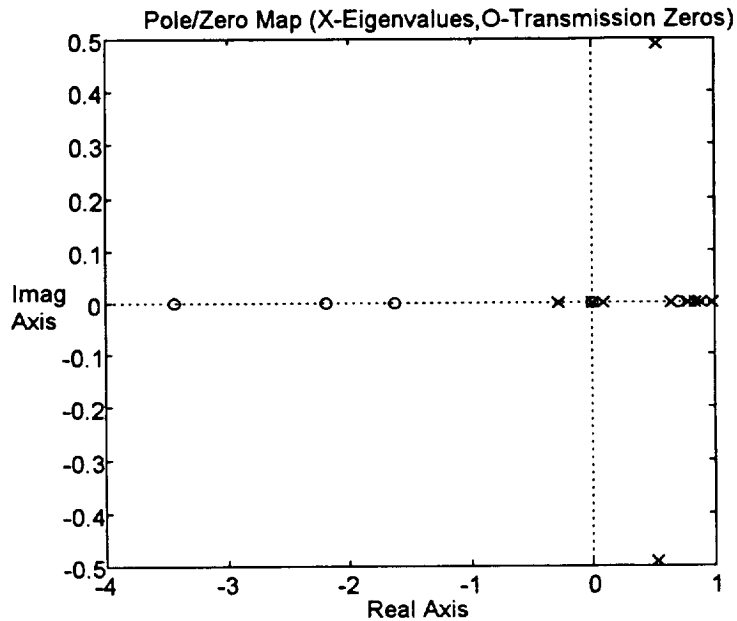
Figure 64. SysID Multivariable Model Pole/Zero Map.

The pole/zero map showing the eigenvalues and transmission zeros of the OKID multivariable model is shown in Figure 65. Since the magnitude of the eigenvalues in Figure 65 are less than unity, this model is considered stable. The OKID MIMO model differs from the SysID MIMO model in that the eigenvalues of the OKID model are all real, all transmission zeros are complex conjugates, and a minimum number of eigenvalues are used to describe the system.
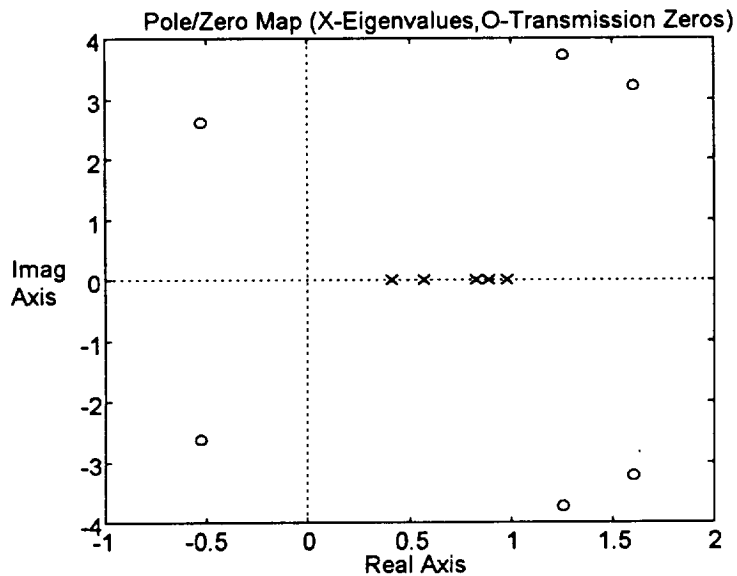
Figure 65. OKID Multivariable Model Pole/Zero Map.

4. RPCM Fit Comparison

Both multivariable state-space model estimates were compared to shoulder yaw, shoulder pitch, and elbow pitch data obtained from an RPCM experiment (joint angles shown in Figure 66) performed in the hydraulic manipulator test bed at NASA LaRC. Both estimates will be evaluated on the how well each model fits the data set as well as the whiteness and independence of each model's residuals. Ideally, all residuals should be white and independent of the input for the model to perfectly identify the dynamic characteristics of the joints.
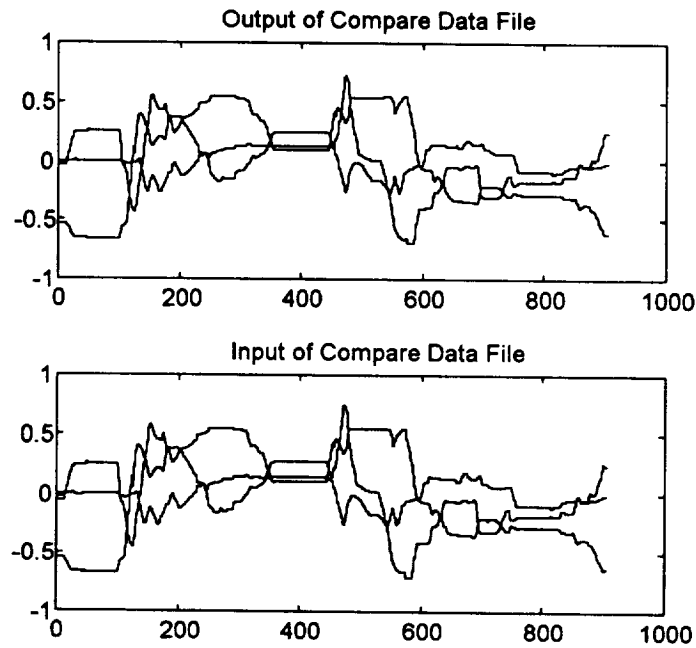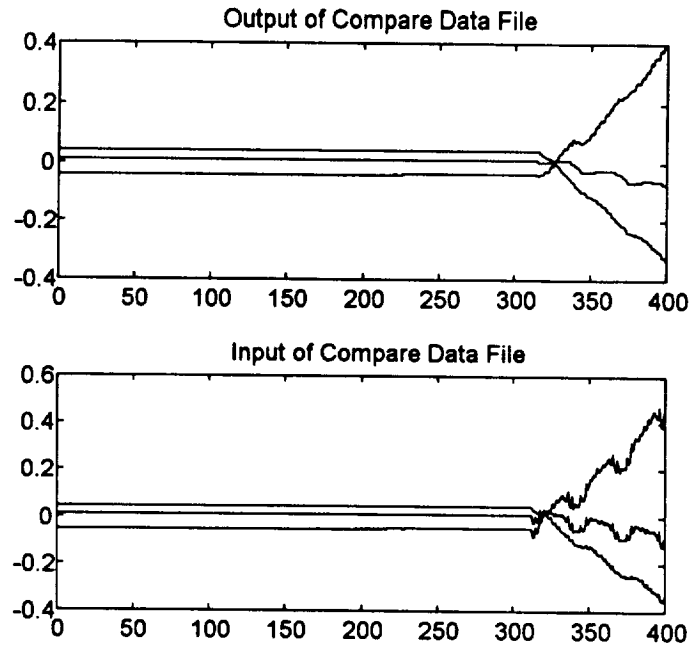

Figure 66. Multivariable RPCM Experiment Data.

SysID RPCM Model Fit

Figures 67 - 69 show outputs of the multivariable SysID model compared to actual outputs from the RPCM experiment. As seen in the Figures 67 and 69, the SysID model matches both the shoulder yaw and elbow pitch responses quite well. The shoulder pitch model output shown in Figure 68 is adequate but doesn't quite match the peaks of the RPCM data set. This implies that the SysID model may not sufficiently characterize the true dynamic characteristics of the shoulder pitch joint.
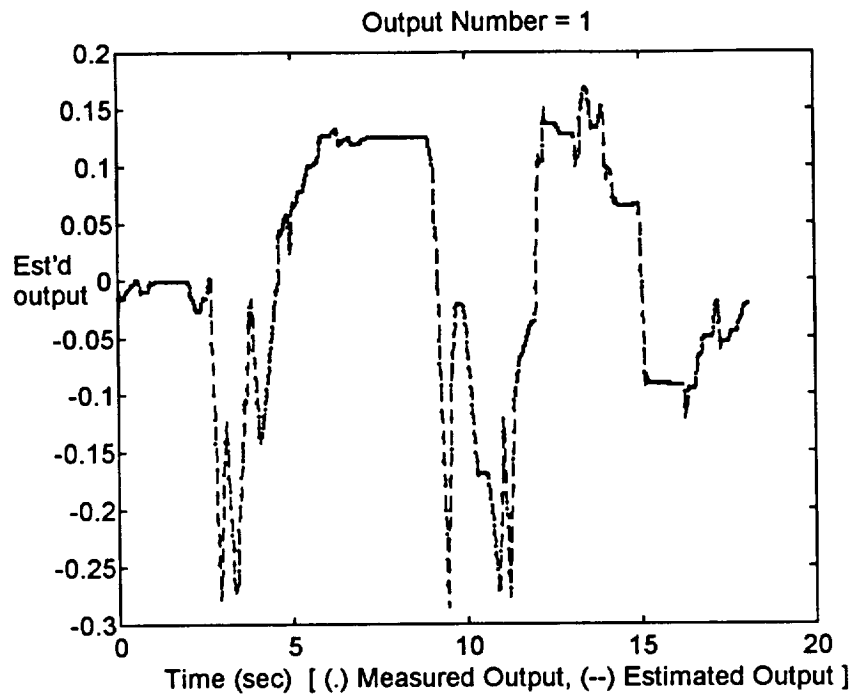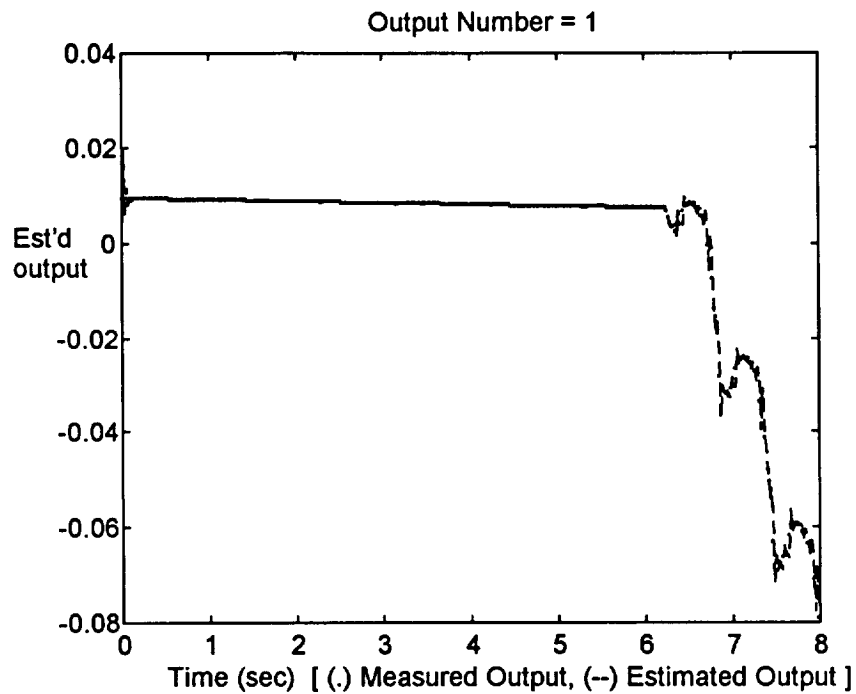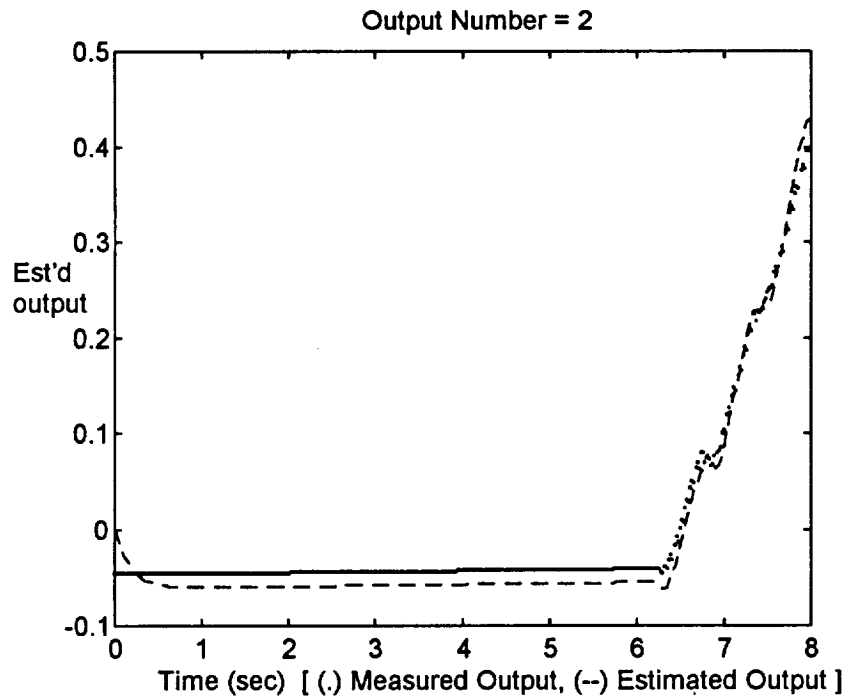
Figure 67. SysID RPCM Shoulder Yaw Comparison.
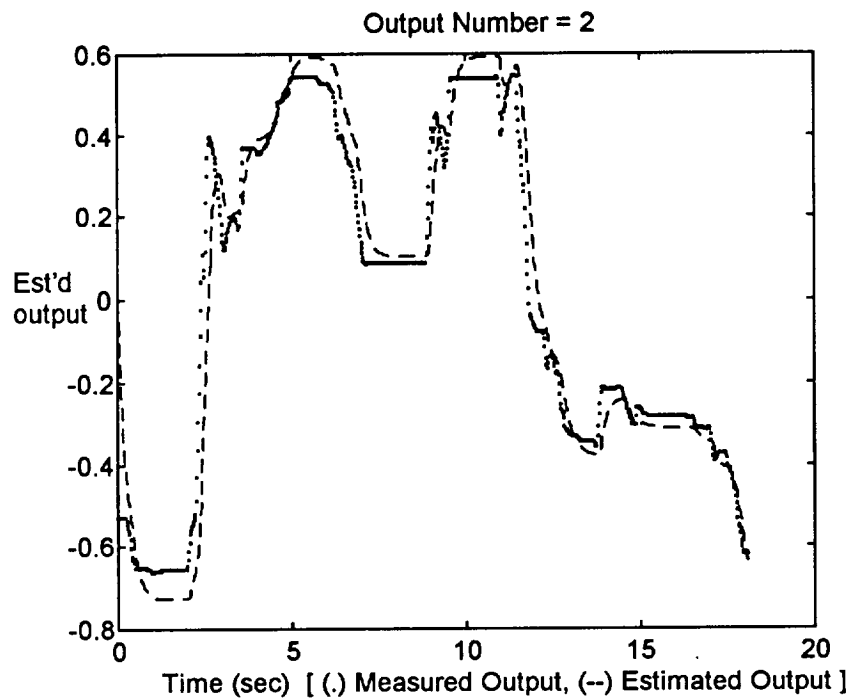
Figure 68. SysID RPCM Shoulder Pitch Comparison.
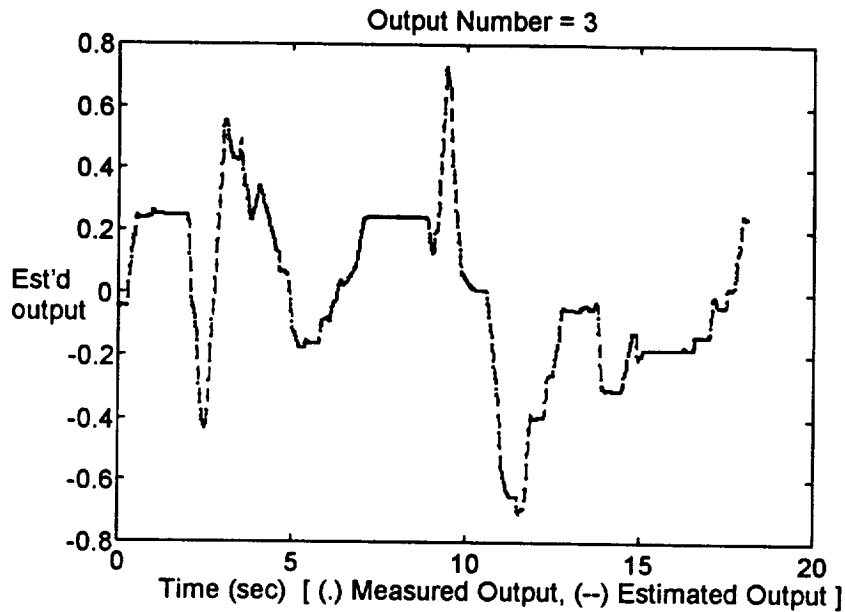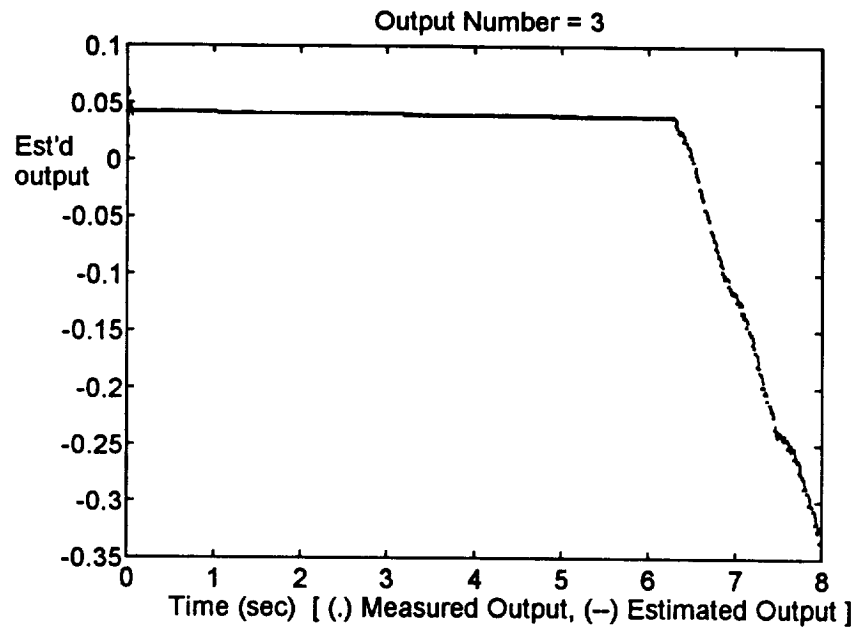
Figure 69. SysID RPCM Elbow Pitch Comparison.

The residuals associated with the RPCM data and the SysID multivariable model estimate are shown in Figure 70. For the SysID model to correctly describe the dynamics of each joint, residuals must be ideally white and independent of the input. Figures 71 and 72 show the whiteness of the SysID residuals associated with the RPCM data set. As seen in the figures, the shoulder yaw and elbow pitch residuals are fairly white. Residuals for the shoulder pitch joint, however, were not white. This is partially due to the use of the OE structure which focuses more on the dynamics than the noise properties of the shoulder pitch joint.
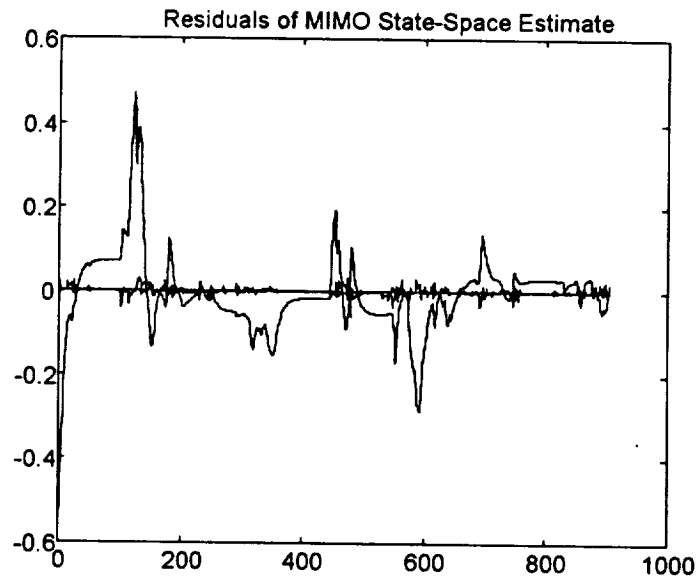
Figure 70. SysID RPCM MIMO Residuals.
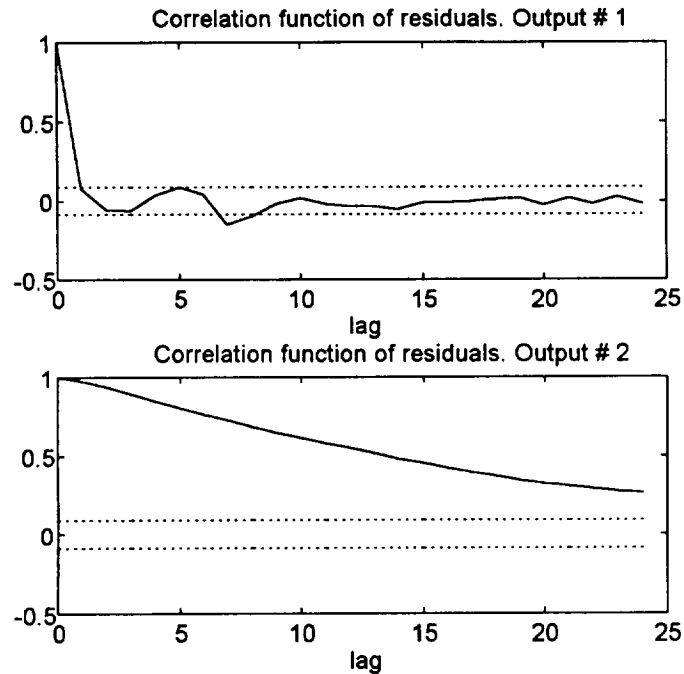
Figure 71. SysID Shoulder Yaw and Pitch Residual Whiteness.
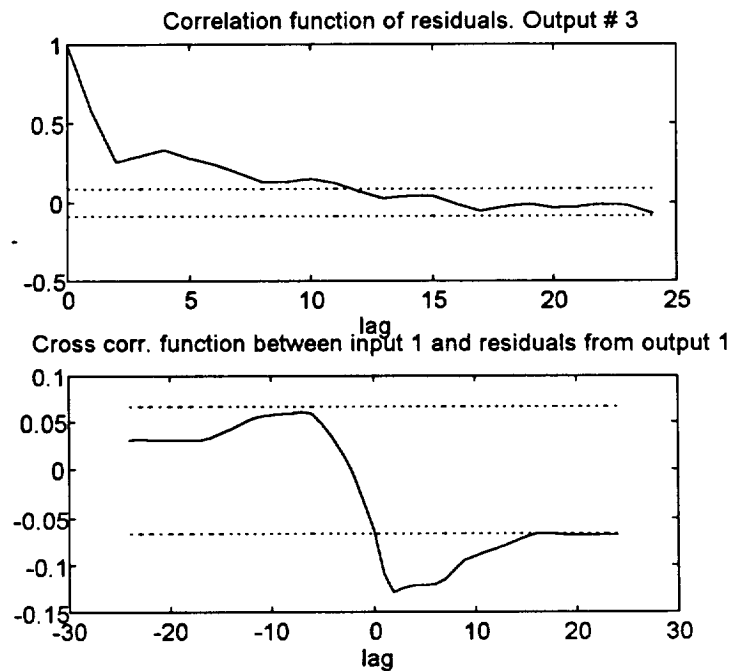
Figure 72. SysID Elbow Pitch Whiteness and Shoulder Yaw Independence.

To determine residual independence for the multivariable SysID model estimate, the cross-correlation of the residual and the input for each joint was determined. The lower plot in Figure 72 shows the independence of the shoulder yaw residuals. For small positive lags, the shoulder yaw residuals are correlated. For lags greater than fifteen, the

SysID estimate correctly models the dynamics of the shoulder yaw joint for the RPCM data set.

OKID RPCM Model Fit

Figures 73 - 75 show outputs of the multivariable OKID model compared to actual outputs from the RPCM experiment. As seen in the comparison plots, the OKID model matches the shoulder yaw, shoulder pitch, and elbow pitch outputs very well.
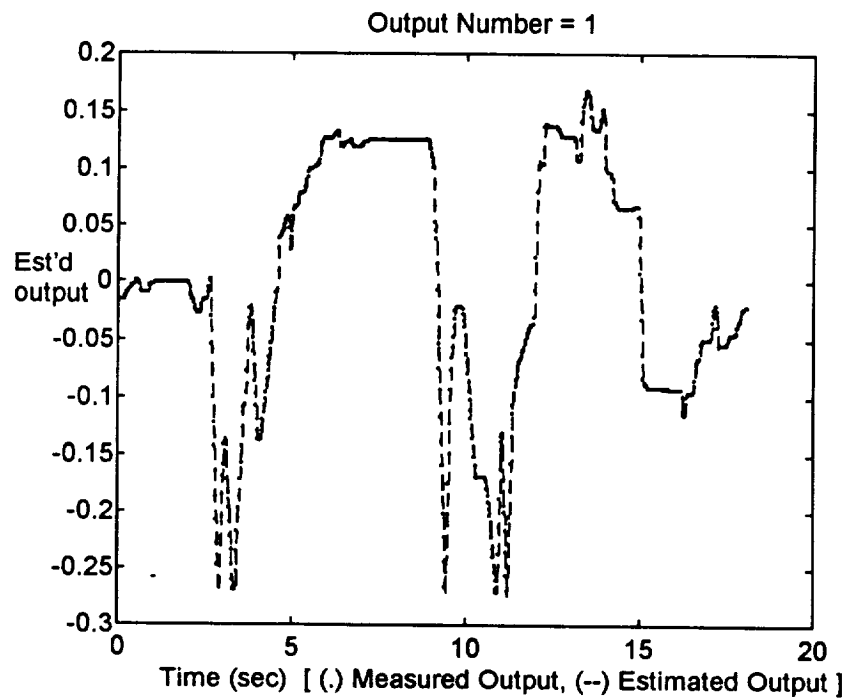
Figure 73. OKID RPCM Shoulder Yaw Comparison.
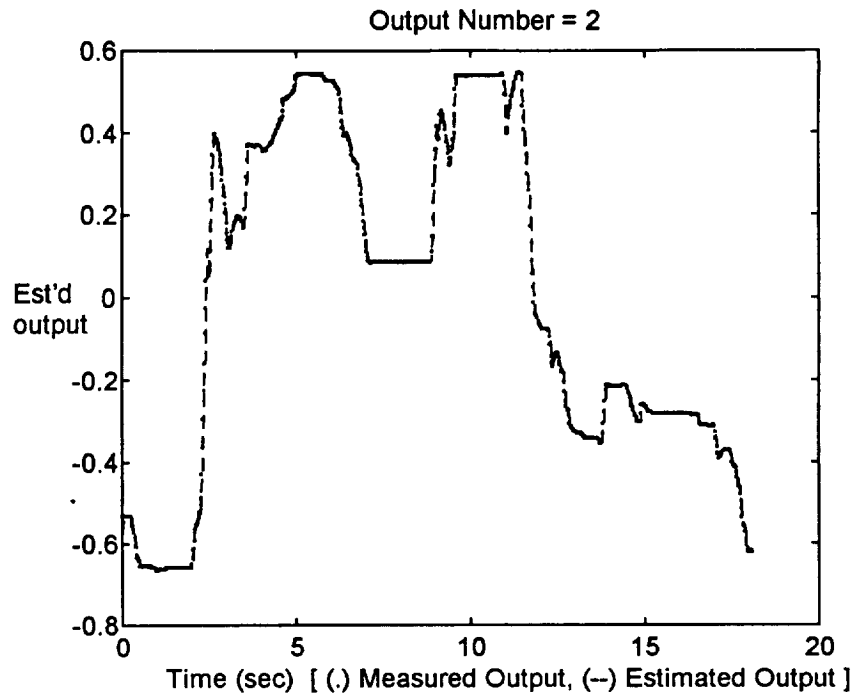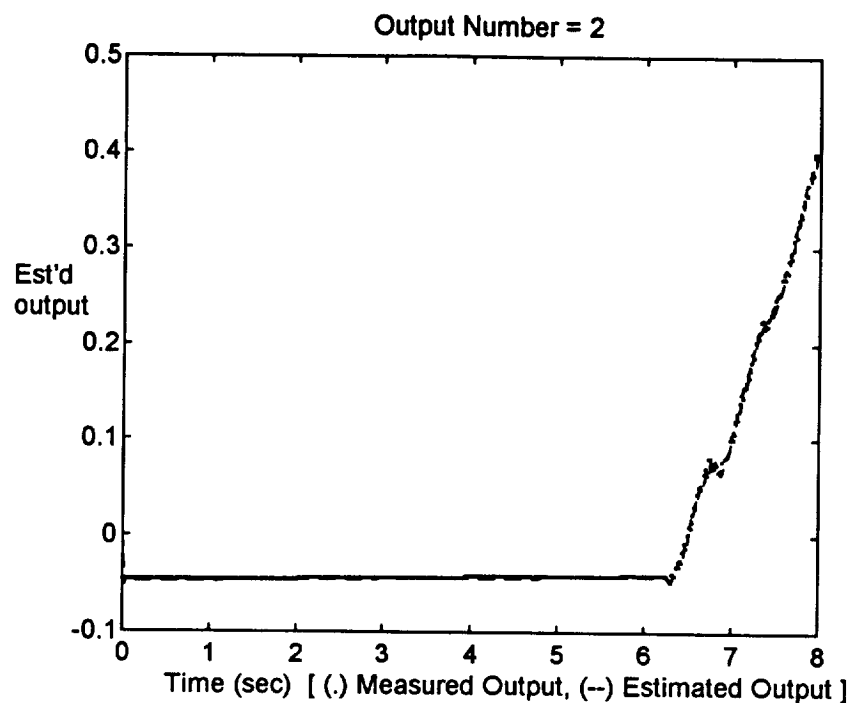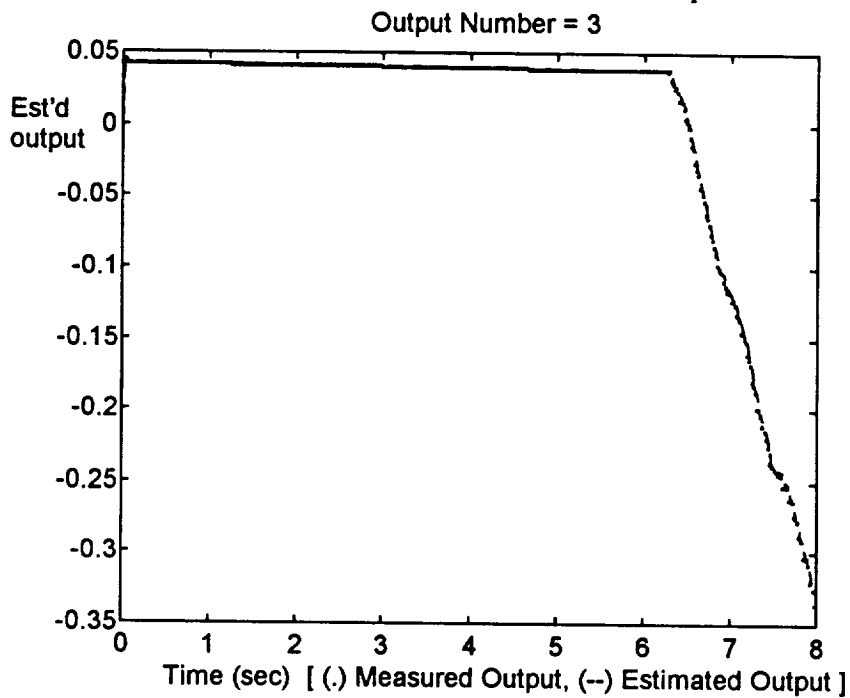
Figure 74. OKID RPCM Shoulder Pitch Comparison.
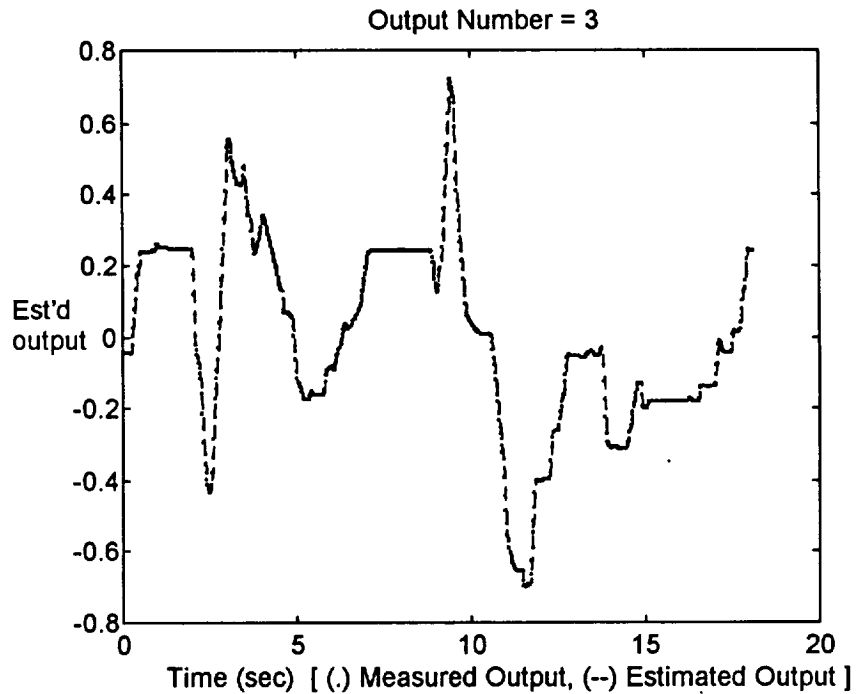
Figure 75. OKID RPCM Elbow Pitch Comparison.

The residuals associated with the RPCM data and the OKID multivariable model estimate are shown in Figure 76. The computed residuals for the shoulder yaw and shoulder pitch joints are fairly white as seen in Figures 77. Residuals for the elbow pitch joint (Figure 78, top plot) are not as white as the other joints. Overall, the OKID produces good residual whiteness for the RPCM experiment.
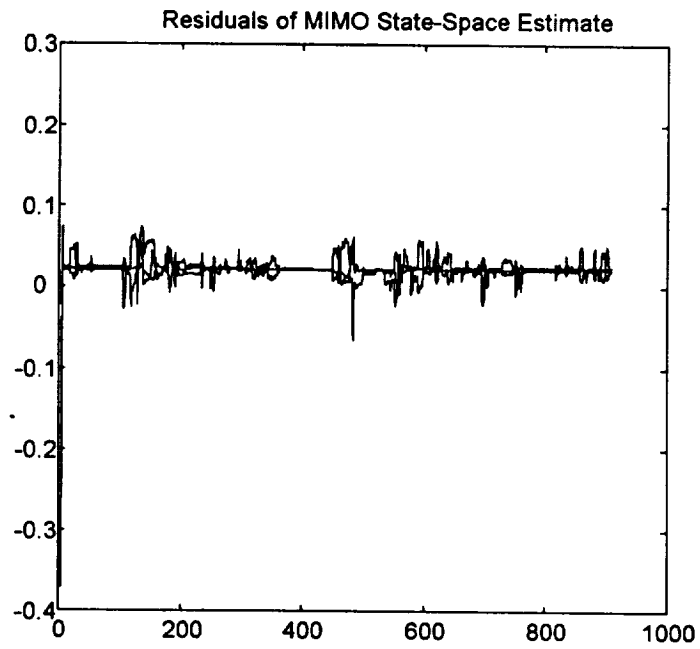
Figure 76. OKID RPCM MIMO Residuals.
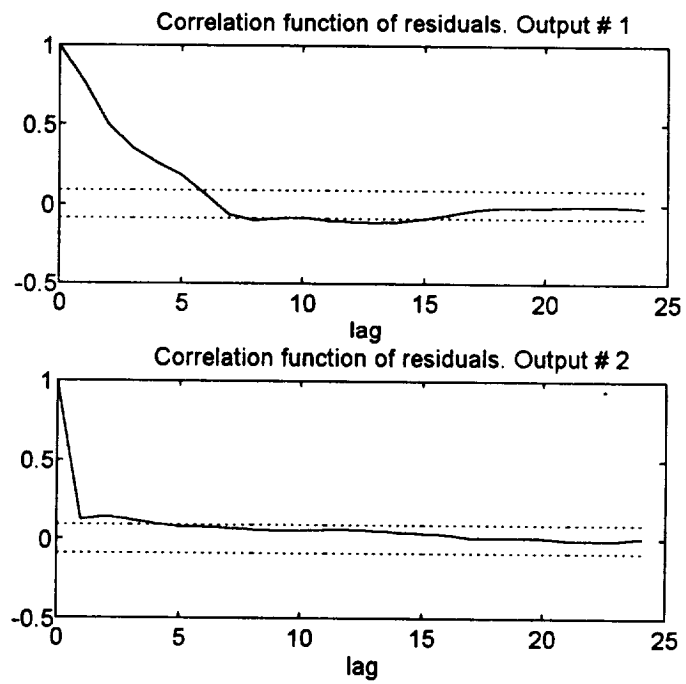
Figure 77. OKID Shoulder Yaw and Pitch Residual Whiteness.
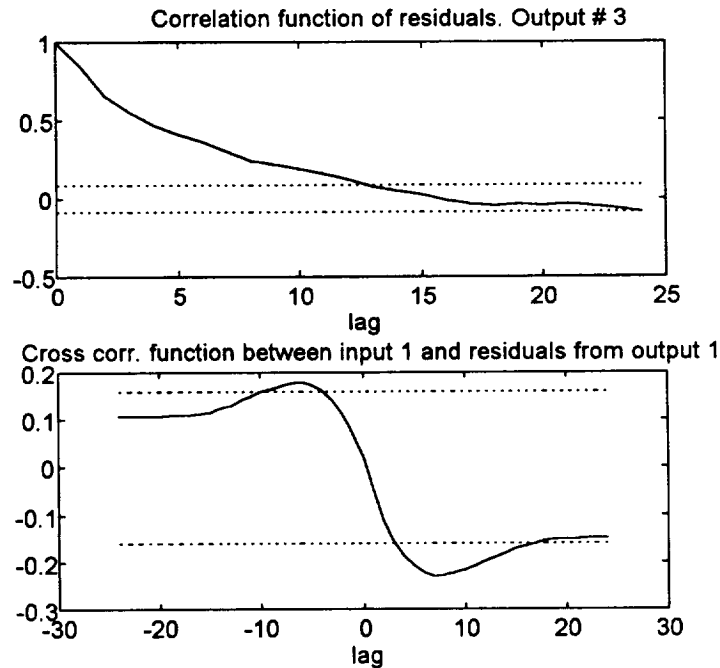
Figure 78. OKID Elbow Pitch Whiteness and Shoulder Yaw Independence.

The lower plot in Figure 78 shows the independence of the shoulder yaw residuals. For positive lags between five and fifteen, the shoulder yaw residuals were moderately correlated. This can possible be attributed to the significant nonlinearities previously found in the shoulder yaw joint.

5. MIMO Chirp Fit Comparison

Besides the RPCM experiment data, both multivariable state-space estimates were compared to various MIMO data sets to determine the constraints of each identified model. Results of comparing both model estimates to various MIMO data sets will be provided in the next section. This section will describe comparisons of the model estimates to the five to ten hertz linearly swept MIMO chirp data set (Figure 79). Output comparisons of each joint will be shown for both model estimates as well as the magnitude of each model's residuals to the MIMO chirp data set.

Figure 79. Multivariable Chirp Experiment Data.

SysID MIMO Chirp Fit

Figures 80 - 82 show outputs of the multivariable SysID model compared to actual outputs from the MIMO chirp experiment. The SysID model effectively matched both the shoulder yaw and elbow pitch responses. The shoulder pitch model output (Figure 81) deviated slightly from the shoulder pitch chirp output. This characteristic was also found when the shoulder pitch model output was compared to the RPCM data set. This implies that the multivariable SysID model, though adequate, may not sufficiently characterize the true dynamics of the shoulder pitch joint.

Figure 80. SysID Chirp Shoulder Yaw Comparison.

Figure 81. SysID Chirp Shoulder Pitch Comparison.

75

Figure 82. SysID Chirp Elbow Pitch Comparison.

The residuals associated with the MIMO chirp data set and the SysID multivariable model estimate are shown in Figure 83. The largest residual in the plot is attributed to the model errors of the shoulder pitch joint. Residual analysis for the MIMO chirp data set (not shown), were comparable to the results obtained using the RPCM experiment data. In other words, shoulder yaw and elbow pitch residuals are fairly white. Residuals for the shoulder pitch joint, however, were not white.
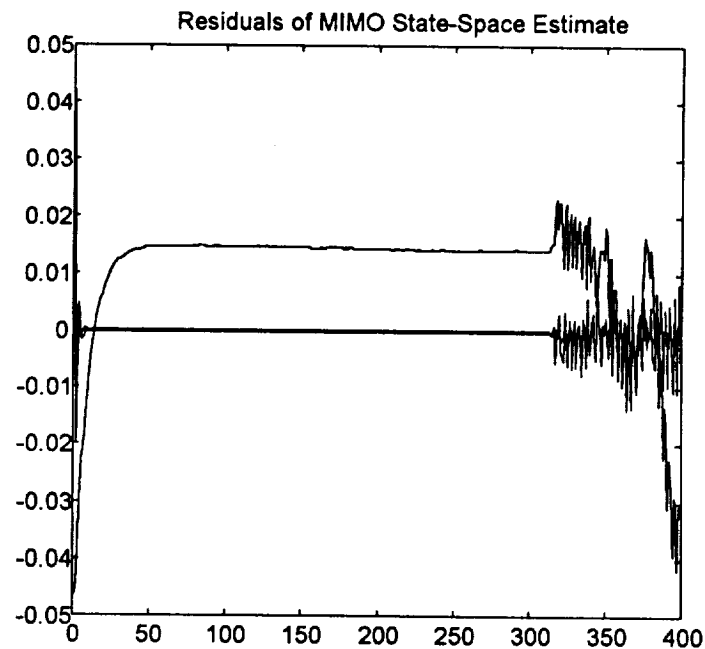
Figure 83. SysID MIMO Chirp Residuals.

Results of residual independence for the multivariable SysID model estimate yielded slight dependence for the shoulder yaw joint at small lags indicating that the SysID model may not adequately characterize shoulder yaw characteristics in the ten hertz range. A small amount of coupling was also found to exist between the shoulder yaw residuals and shoulder pitch input at this frequency range.

OKID MIMO Chirp Fit

Figures 84 - 86 show outputs of the multivariable OKID model compared to actual outputs from the MIMO chirp data set. The OKID model output matched the shoulder yaw, shoulder pitch, and elbow pitch outputs very well.
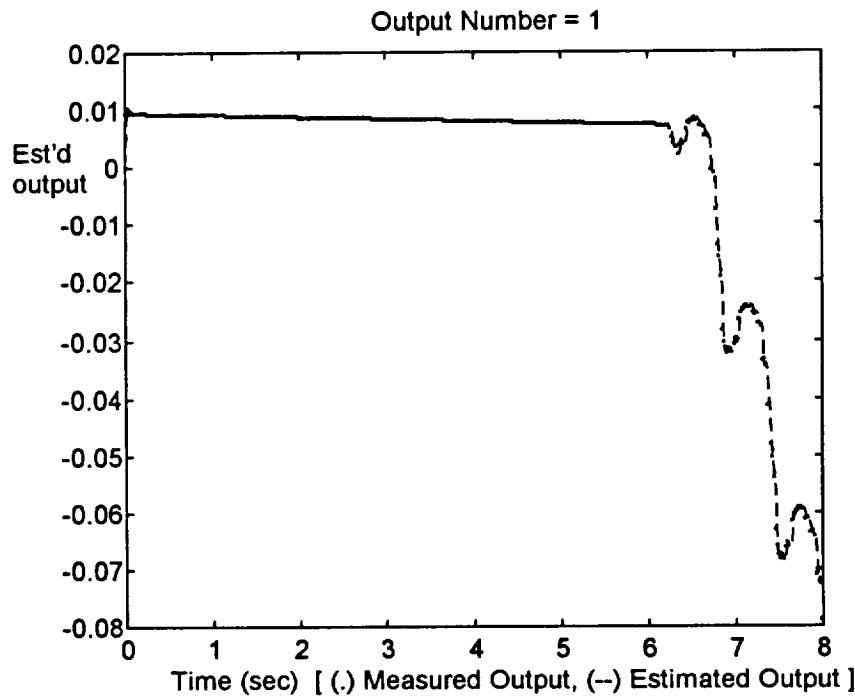
Figure 84. OKID Chirp Shoulder Yaw Comparison.

Figure 85. OKID Chirp Shoulder Pitch Comparison.

Figure 86. OKID Chirp Elbow Pitch Comparison.

The residuals associated with the MIMO chirp data set and the OKID multivariable model estimate are shown in Figure 87. The OKID model estimate produced good residual whiteness for the shoulder pitch and the elbow pitch joints (not shown). However, shoulder yaw residuals showed only marginal whiteness.
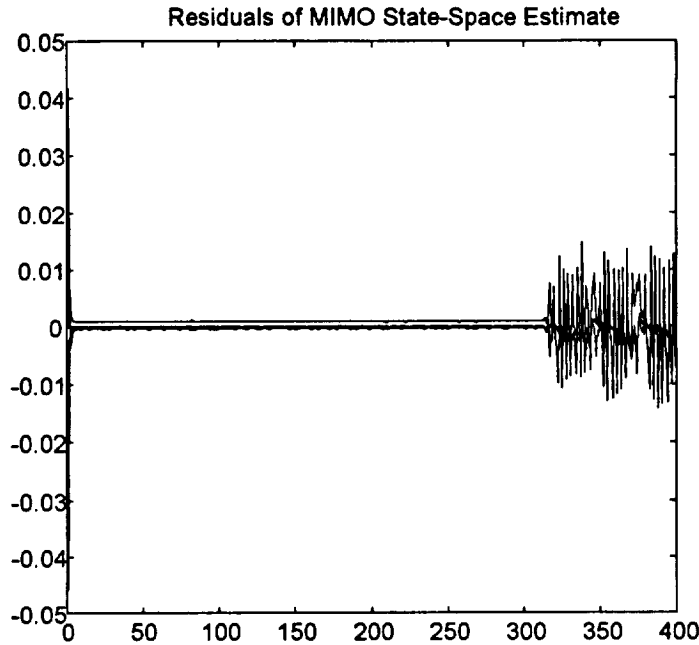
Figure 87. OKID MIMO Chirp Residuals.

Results of residual independence for the multivariable OKID model estimate produced significant correlation for the shoulder yaw joint at small lags indicating that the OKID model may not adequately characterize shoulder yaw dynamics in the ten hertz range. A small amount of coupling was found to exist between the shoulder yaw residuals and shoulder pitch input and between the shoulder yaw residuals and the elbow pitch input in the ten hertz frequency range.

6. Comparison Results

This section will compare both the SysID and OKID multivariable model estimates for several performance categories. For each category, the strengths and weaknesses of each model will be evaluated as well as the technique used to identify the model estimate. Performance categories will include frequency bandwidth, model stability, flexibility, parsimony, robustness, RPCM experiment fit, and various MIMO data fits.

Frequency Bandwidth

The SysID and OKID models both produced comparable Bode plots indicating that both techniques captured true frequency content of each HMTB joint. Both model estimates were able to follow data sets containing frequency content in the range of 3 to 5 Hz though the identified cutoff frequency for each joint was found to be approximately 1 Hz. Initially, this 1 Hz cutoff result was considered questionably low. Later, however, this low frequency cutoff was verified by a report conducted by the STX Corporation for NASA [16]. The STX report found that Martin Marietta's 1 Hz bandwidth was significantly lower than bandwidths recommended by prior research and by other research engineers [16]. The uncertainty in proper bandwidth selection lies in the fact that an optimum bandwidth for space telerobot applications is unknown.

When compared to data sets containing a greater than 5 Hz frequency content, the OKID estimate slightly outperformed the SysID estimate for each joint. This may have been attributed to inadequate modeling of the SysID estimate.

Stability

Since the magnitude of the eigenvalues for both multivariable model estimates were less than unity, both models were found to be stable.

Flexibility

In terms of flexibility, the prediction error techniques used to determine the SysID model estimate provided numerous approaches to model both the dynamics of the system as well as the noise properties of the HMTB joints. The OKID technique, though more accurate, was less flexible.

Parsimony

The Observer/Kalman filter identification (OKID) technique was more parsimonious in its attempt to describe the dynamic characteristics of the HMTB joints. Information extracting using this technique produced a minimum realization in allowing each joint to be described by a second-order system. In contrast, the SysID model used a fifth-order model to describe the shoulder yaw dynamics, a second-order model to describe the shoulder pitch dynamics, and a third-order model to describe the elbow pitch dynamics.

Robustness of estimates

The SysID model proved to be more robust when compared to the OKID model estimate. Comparable SysID models were obtained even in the presence of bias errors and outliners in the data set. For instance, data detrending and/or filtering reduced a particular SysID model from a third-order system to a second-order system. In contrast, the OKID estimate was more sensitive to bias errors and outliners in the data set. One OKID model required a fourth-order system to describe the dynamics of a joint. However, a second-order model was sufficient when the data set was detrended.

RPCM Experiment Fit

The OKID multivariable model estimate provided a much better fit when compared to data obtained from the RPCM experiment. The OKID estimate obtained a more accurate fit by effectively minimizing the residuals for each joint model. The identified model showed minimal coupling between the joints in the localized region. The SysID model estimate consistently showed high residuals for the shoulder pitch SISO estimate. This can be attributed to the OE model structure used to characterize the joint.

MIMO Data Fits

The OKID estimate produced a better fit when compared to a majority of MIMO data sets. For low frequency data sets, the SysID estimate modeled the dynamics of the shoulder yaw joint much better than the OKID estimate. This would imply perhaps a hybrid model between the OKID estimate (shoulder pitch and elbow pitch) and the SysID

estimate (shoulder yaw) to provide an overall better multivariable model estimate for low frequencies.

Overall, the Observer/Kalman filter identification (OKID) technique produced a better multivariable estimate when compared to the SysID multivariable model estimate. Menu-driven software was developed and used to evaluate the OKID model and to compare both multivariable models.

VII. Conclusions

Linear, dynamic models for three joints of the hydraulic manipulator test bed (HMTB) at the NASA Langley Research Center have been identified using nonparametric and parametric system identification techniques. Nonparametric techniques yielded an approximate 1 Hz bandwidth for each joint using transfer function analysis, an expected order for each joint using correlation analysis, and the degree of process and measurement disturbances for each joint using spectral analysis. Two different parametric identification techniques were used and compared in developing dynamic models of the joints. The first parametric technique, used primarily for control system identification, employed a prediction-error method to produce a stable model estimate. The bandwidth for this estimate proved adequate when compared to several data sets. An advantage of this technique is its flexibility of use. The user has several options, alternatives, and methods from which to conduct an identification investigation. When compared to the RPCM experiment data, this technique yielded adequate results. The second parametric technique, used primarily in modal system identification, employed a minimum realization algorithm to produce a stable model estimate using only second-order systems to describe the characteristics of each joint. This technique was extremely simple to use while yet providing an adequate bandwidth for the identified models among many data sets. The models identified using this technique produced an accurate fit to both the RPCM experiment data and various MIMO data sets.

Matlab menu-driven system identification software scripts were developed for this thesis. One program, using functions from the *MATLAB System Identification Toolbox*, was used to perform nonparametric and parametric analysis of the manipulator data. The other program identified models using the Observer/Kalman Filter Identification (OKID) technique, provided in the *System/Observer/Controller Identification Toolbox (SOCIT)*. The latter program used several toolboxes to perform MIMO comparisons for the identified multivariable models. Both programs were found to be extremely useful especially in minimizing the time required to perform nonparametric and parametric analysis of the data. The programs, modular in design, are easily expandable. Though written to use data from the manipulator joints, the programs may be easily adapted to incorporate data from any dynamic system for the purpose of identification.

1. Suggestions for Future Work

With the identified models in this investigation valid only in a localized region with a specific loading, additional identification tests should be performed. Recursive identification methods, in particular, should be performed with several different loading configurations for the manipulator. Also, a more complete model should be identified by determining the dynamic parameters of the shoulder roll, wrist pitch, wrist yaw, and wrist roll joints (which were not identified in this thesis).

2. Model Reference Control

A model reference control system is proposed for the previously identified multivariable dynamic HMTB model. In this controls approach, the behavior of the ground-based model would closely resemble the behavior of the on-orbit flight model for

each joint. This capability would allow astronauts to perform crucial mission training tasks with a ground-based hydraulic manipulator that would be kinematically and dynamically equivalent to the flight manipulator. Figure 88 shows a block diagram of the model reference control system proposed for the DOSS manipulator. A distinct advantage of this control system is its ability to perform acceptably in the presence of nonlinearities, uncertainties, and variations in the identified system parameters [18]. This service would de-emphasize errors developed in the dynamic parameters during the model identification process.

Using the previously identified linear, dynamic HMTB model (equation 5.1), a linear model reference system can be described by the state equation

$$x_d(k + 1) = A\, x_d(k) + B\, v(k) \tag{7.1}$$

where

$x_d(k)$ is the state vector of the on-orbit dynamic model,
$v(k)$ is the input vector,
A is the model reference state matrix, and
B is the model reference state matrix.

The model reference control system will have a stable equilibrium state if the magnitude of the discrete-time eigenvalues of A are less than unity. The primary task of the controller in Figure 88 will be to adjust the actuating signal of the identified HMTB model for the purpose of driving the state error between both models to zero [18].
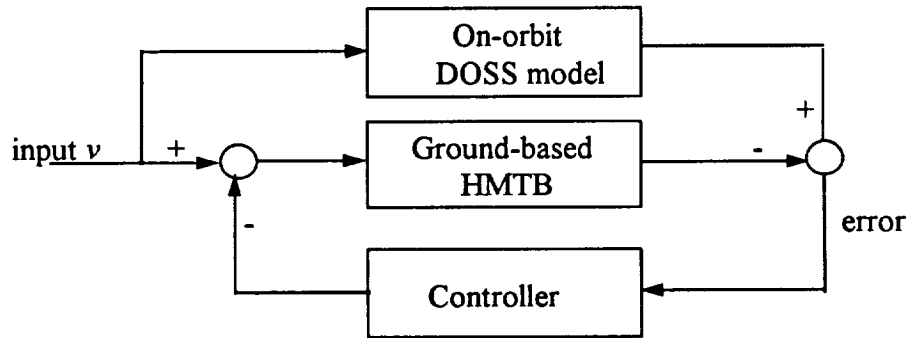
Figure 88. Model Reference Control System for DOSS.

References

[1]   Kohrs, Richard H., "Freedom is an International Partnership," *Aerospace America.* September 1990.

[2]   Fisher, Arthur., "NASA's New Direction," *Popular Science*, March 1991.

[3]   *Summary and Principal Recommendations of the Advisory Committee on the Future of the U.S. Space Program.* NASA Headquarters, December 10, 1990.

[4]   Lawler, A. and Knapp, B., "Canadian Station Role Revised," *Space News.* April 25-May 1, 1994.

[5]   *Flight Telerobotic Servicer (FTS) Requirements Document for Phase C/D.* NASA SS-GSFC-0043, September 1990.

[6]   *FTS-Trainer Design Review Data Package.* WSM E91/004, March 1, 1991.

[7]   *MSS On-Orbit Operations Concept Document, Vol. 2.* SPAR-SS-R0444, December 1992.

[8]   Juang, Jer-Nan., *Applied System Identification.* Prentice-Hall, Englewood Cliffs, New Jersey, 1994.

[9]   Soderstrom, T., and Stoica, P., *System Identification.* Prentice-Hall, Englewood Cliffs, New Jersey, 1989.

[10]   Ljung, L., *System Identification: Theory for the User.* Prentice-Hall, Englewood Cliffs, New Jersey, 1987.

[11]   Juang, J.-N., and Pappa, R. S., "A Comparative Overview of Modal Testing and System Identification for Control of Structures." *Shock and Vibration Digest*, Vol. 20, No. 5, May 1988, pp. 4-15.

[12]   Ho, B. L. and Kalman, R. E., "Effective Construction of Linear State Variables Models from Input/Output Data," *Proceedings of the 3rd Annual Allerton Conference on Circuit and System Theory*, pp. 449-459, 1965.

[13]   Ha, T. T. and Pratt, T., *Study of Spread Spectrum Multiple Access Systems for Satellite Communications with Overlay on Current Services,* NASA CR-180827, 1987.

[14]   Franklin, G. F., Powell, J. D., and Workman, M. L., *Digital Control of Dynamic Systems.* Second Edition. Addison-Wesley, 1990.

[15]   *AT-MIO-16 User Manual.* National Instruments Corporation, Part Number 320476-01, 1992.

[16]   Brooks, T. L., *Telerobot Response Requirements.* STX Corporation. Report Number STX/ROB/90-03. March 1990.

[17]   Shattuck, P. L. and Lowrie, J. W., "Flight Telerobotic Servicer Legacy." *Cooperative Intelligent Robotics in Space III*, Vol. 1829, 1992, pp. 60-74.

[18]   Ogata, K., *Modern Control Engineering.* Second Edition. Prentice-Hall, Englewood Cliffs, New Jersey, 1990.

[19]   Juang, J.-N., Horta L., and Phan M., *System/Observer/Controller Identification Toolbox (SOCIT).* NASA TM-107566. February 1992.

Appendix A. Plots and Graphs

This appendix contains plots and graphs for the shoulder pitch and elbow pitch joints. Explanation of the graphs are discussed in the main text. The graphs and plots are divided into three subdivisions as follows:

A.1   Nonparametric Plots
A.2   Classical Parametric Plots
A.3   OKID Parametric Plots.

A.1   Nonparametric Plots
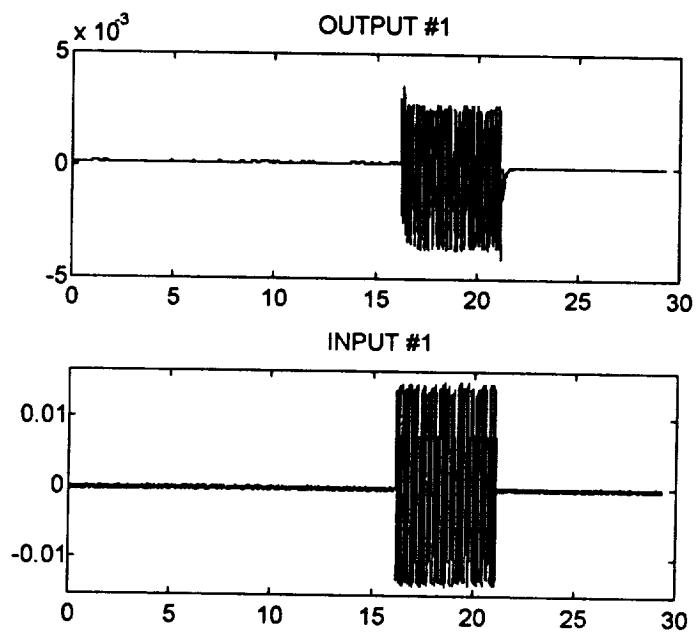
Figure A1. Shoulder Pitch I/O Data.
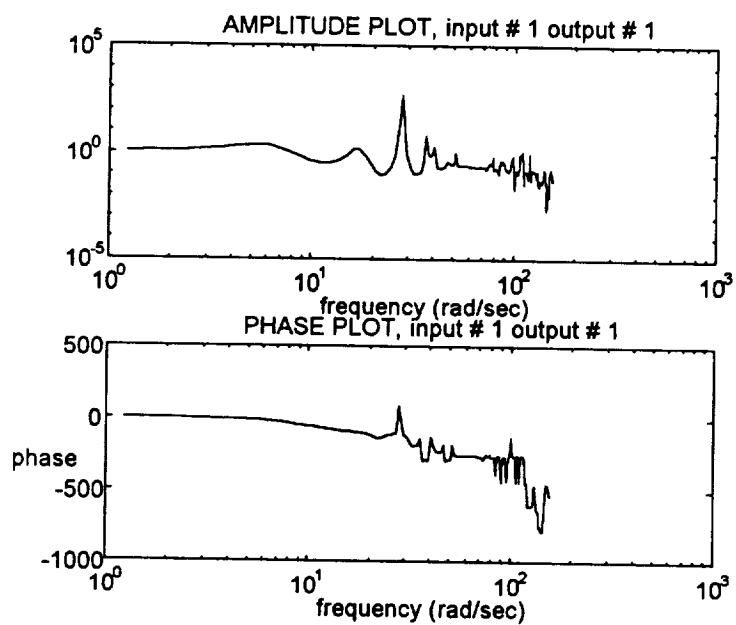
Figure A2. Shoulder Pitch Transfer Function Estimate.
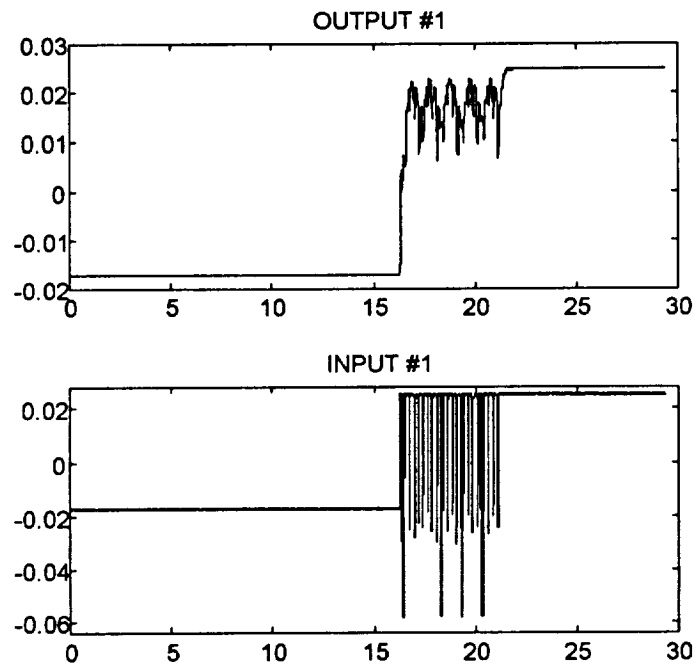
Figure A3. Shoulder Pitch PRBS Data.
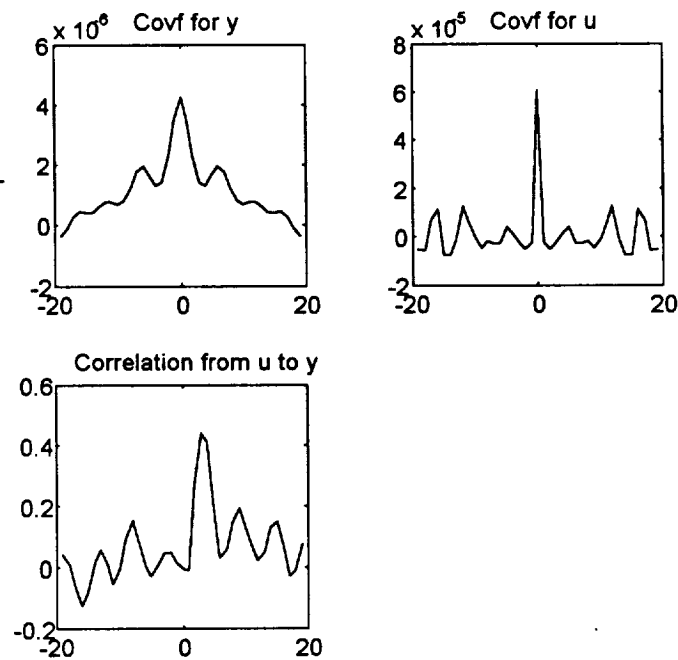
Figure A4. Shoulder Pitch Correlation Plots.

87
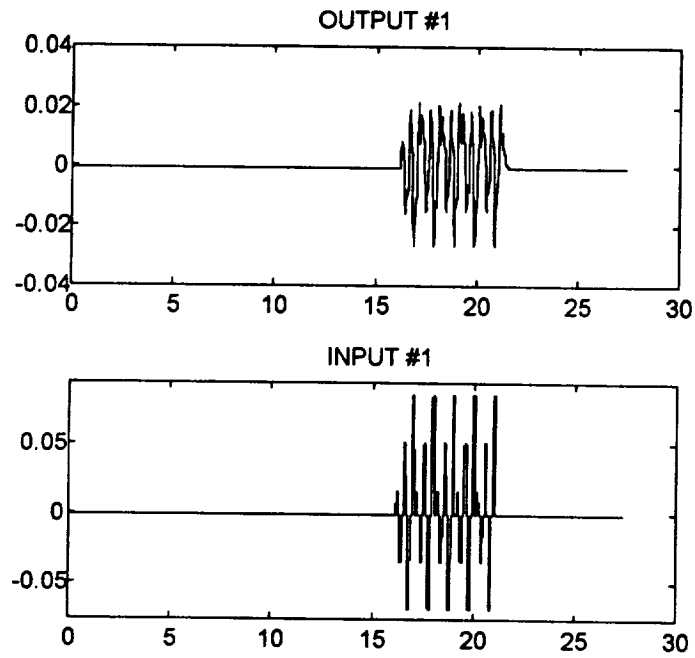
Figure A5. Shoulder Pitch Bipolar Ramping Pulse Data.
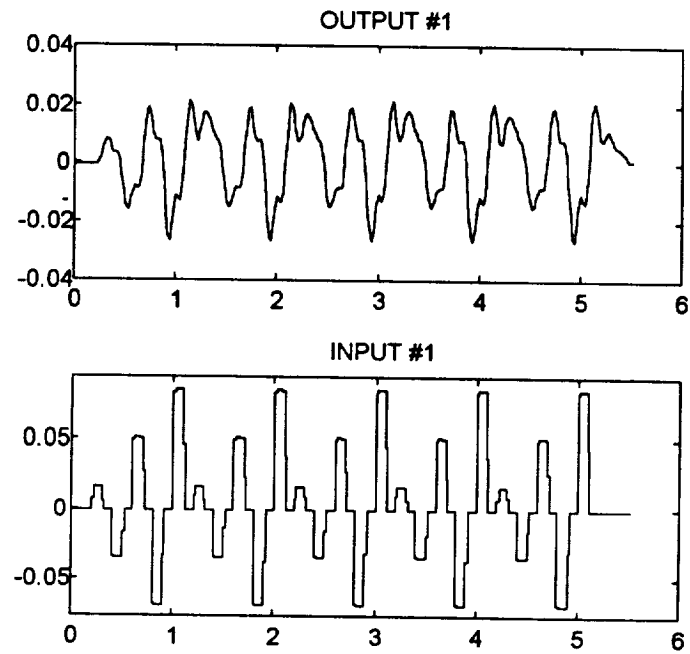
Figure A6. Shoulder Pitch BRP Activity.

88
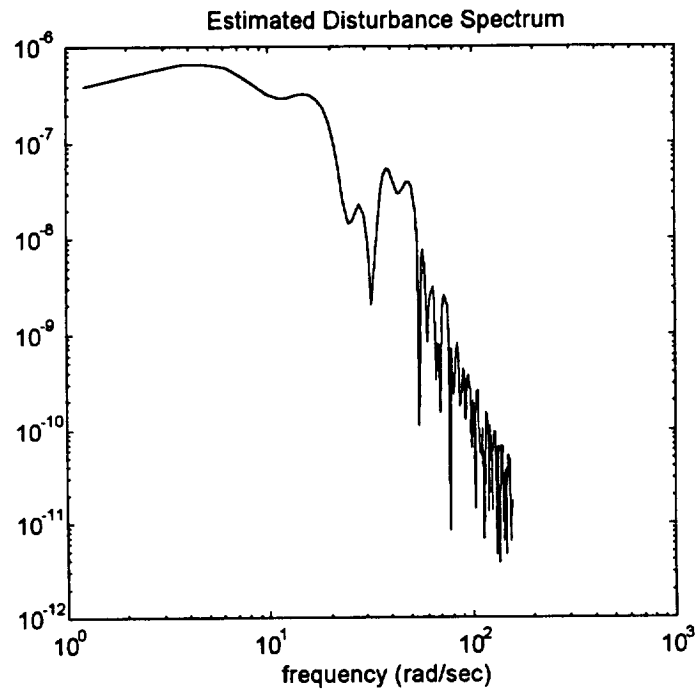
Figure A7. Shoulder Pitch Estimated Disturbance Spectrum.
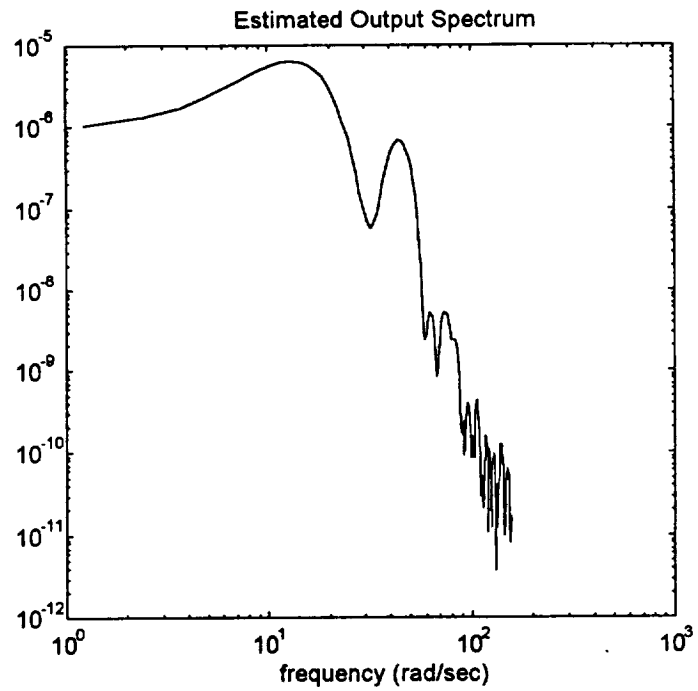
Figure A8. Shoulder Pitch Estimated Output Spectrum.
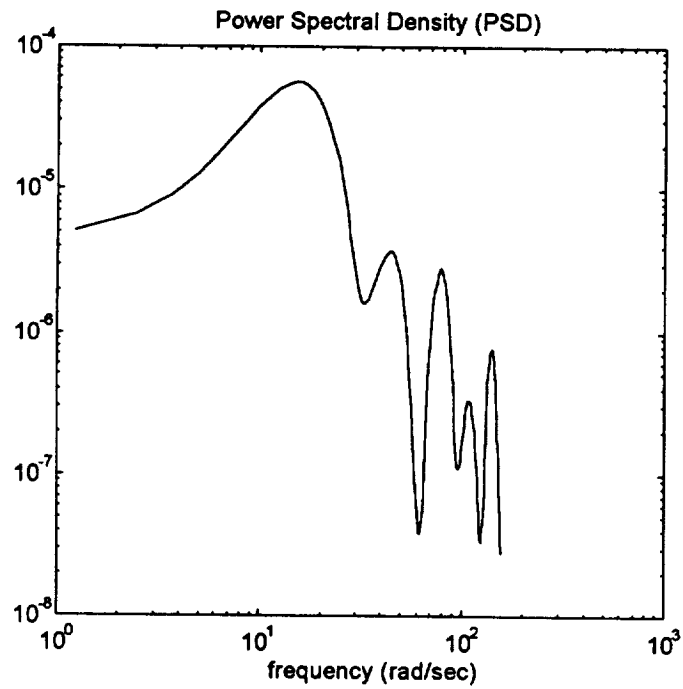
Figure A9. Shoulder Pitch Estimated Input Power Spectrum.
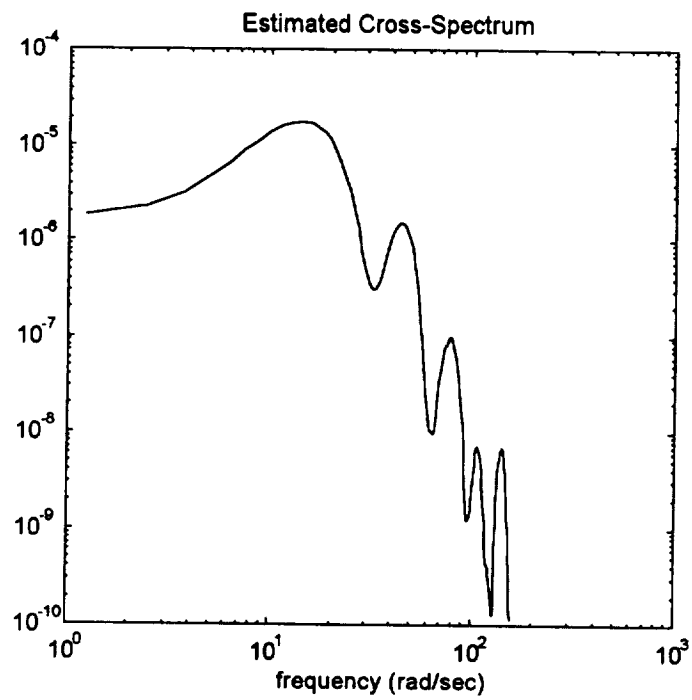
Figure A10. Shoulder Pitch Estimated Cross-Spectrum.
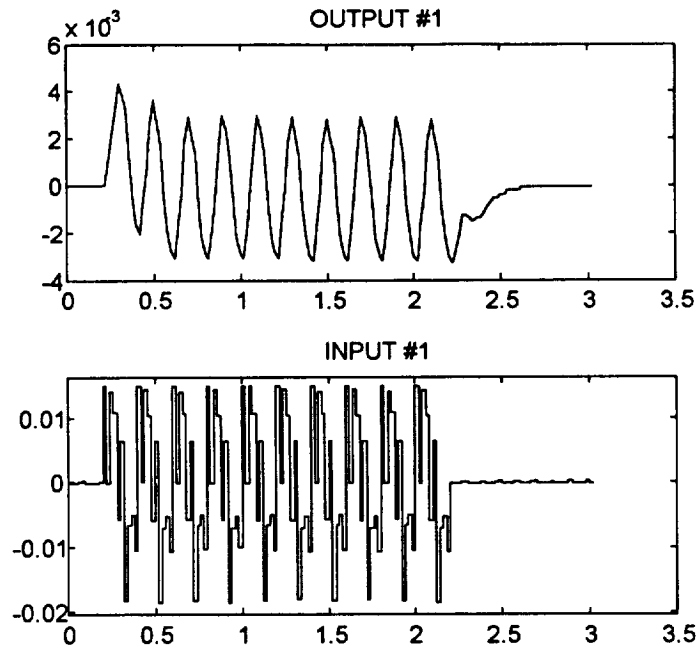
Figure A11. Shoulder Pitch Sum of Sinusoids Activity.
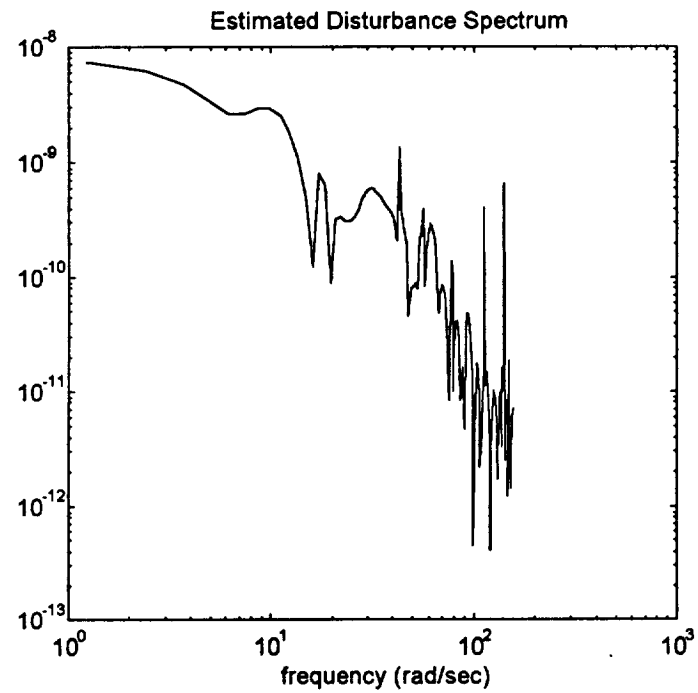
Figure A12. Shoulder Pitch Estimated Disturbance Spectrum.

91
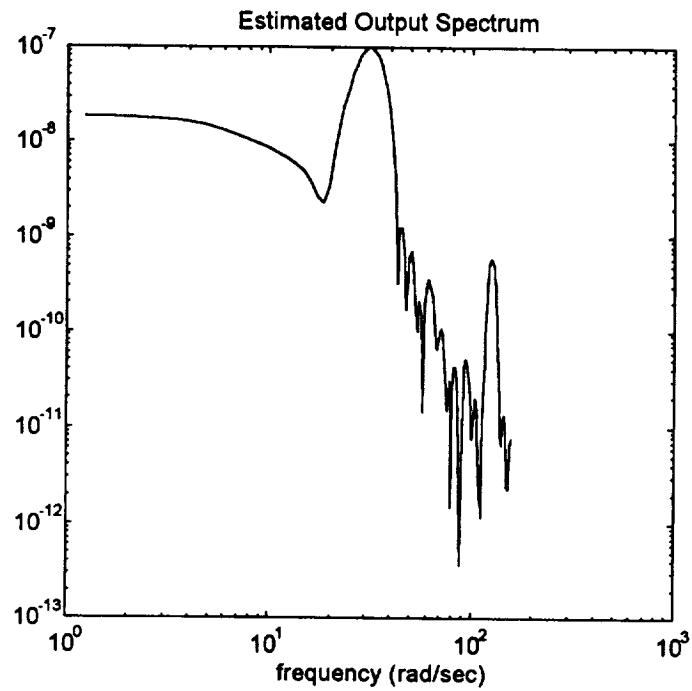
Figure A13. Shoulder Pitch Estimated Output Spectrum.
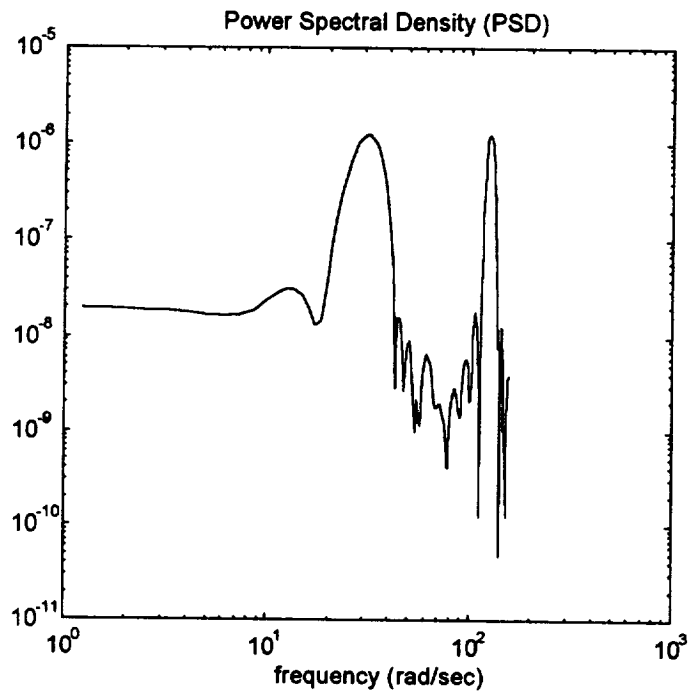
Figure A14. Shoulder Pitch Estimated Input Power Spectrum.
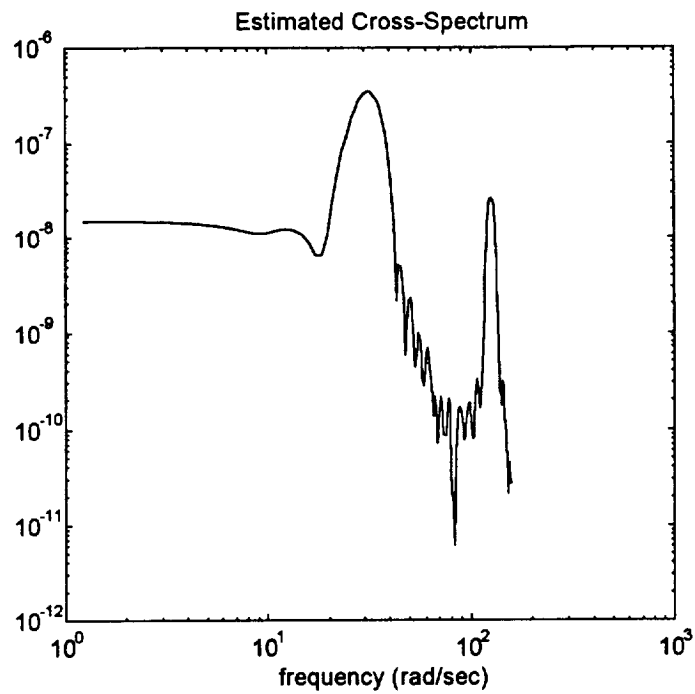
Figure A15. Shoulder Pitch Estimated Cross-Spectrum.
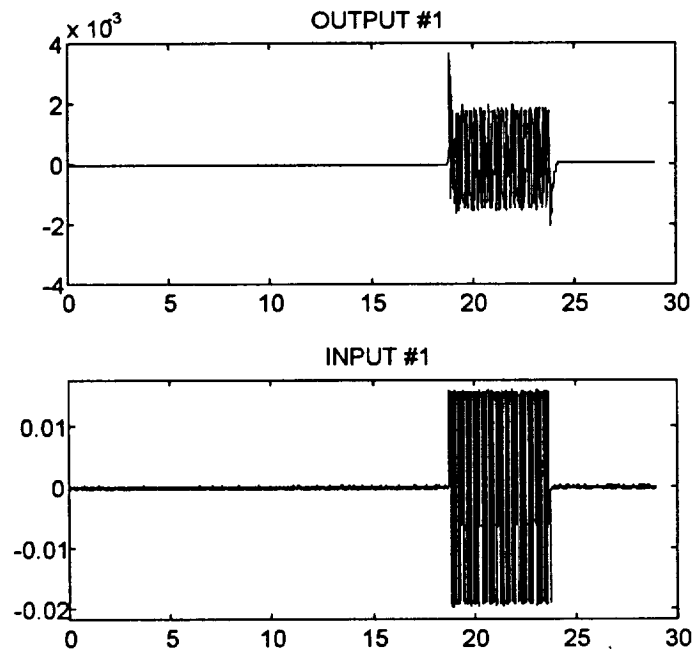
Figure A16. Elbow Pitch I/O Data.
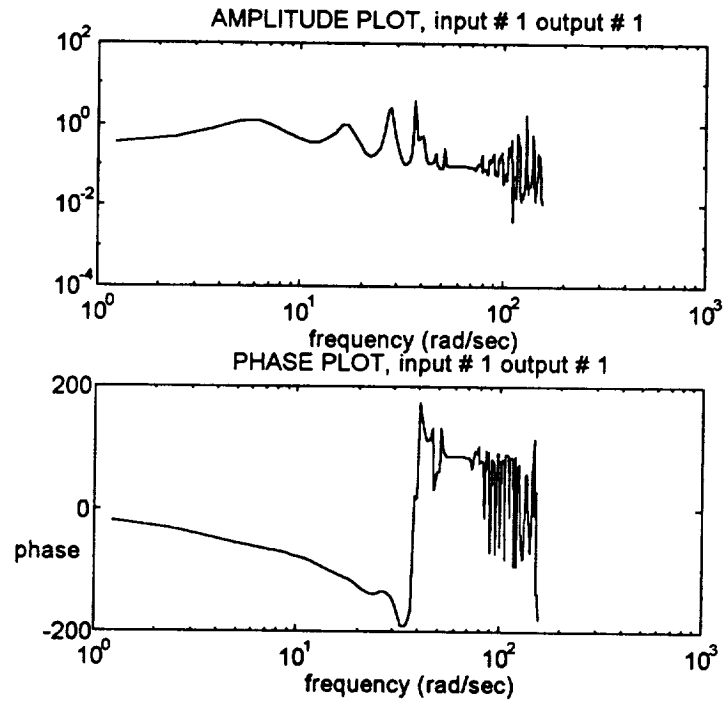
Figure A17. Elbow Pitch Transfer Function Estimate.
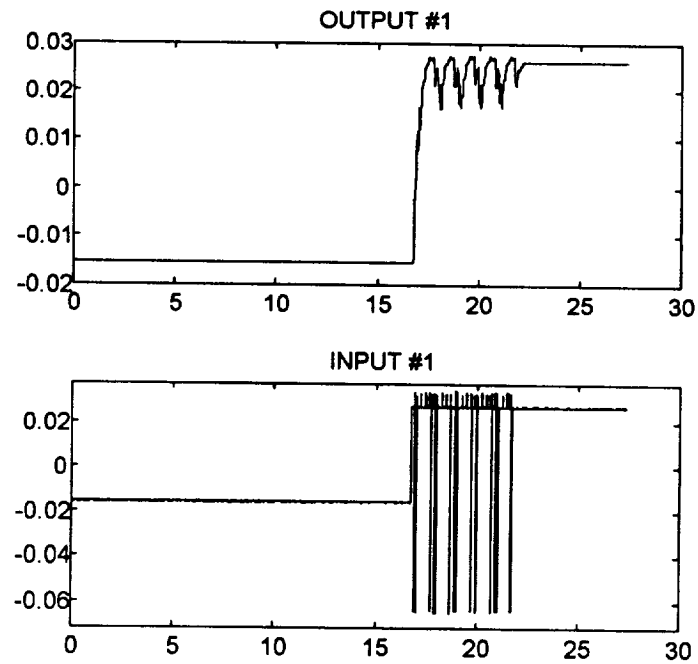
Figure A18. Elbow Pitch PRBS Data.
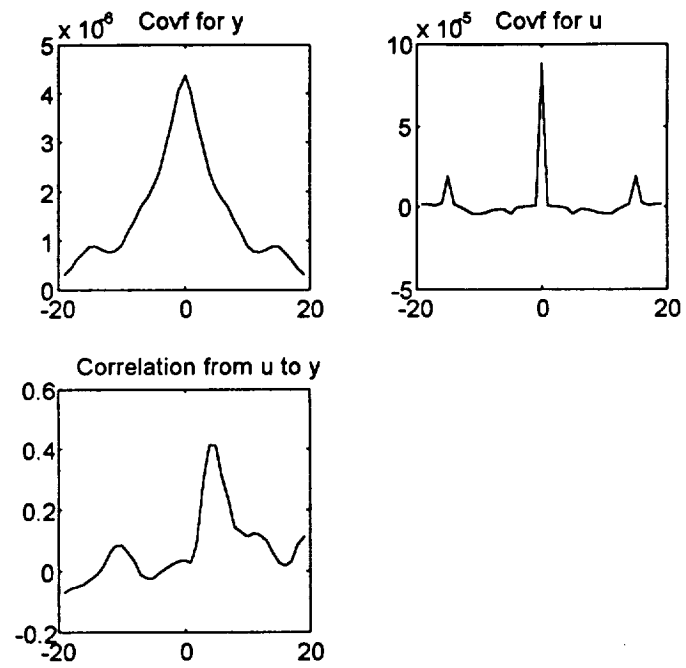
Figure A19. Elbow Pitch Correlation Plots.
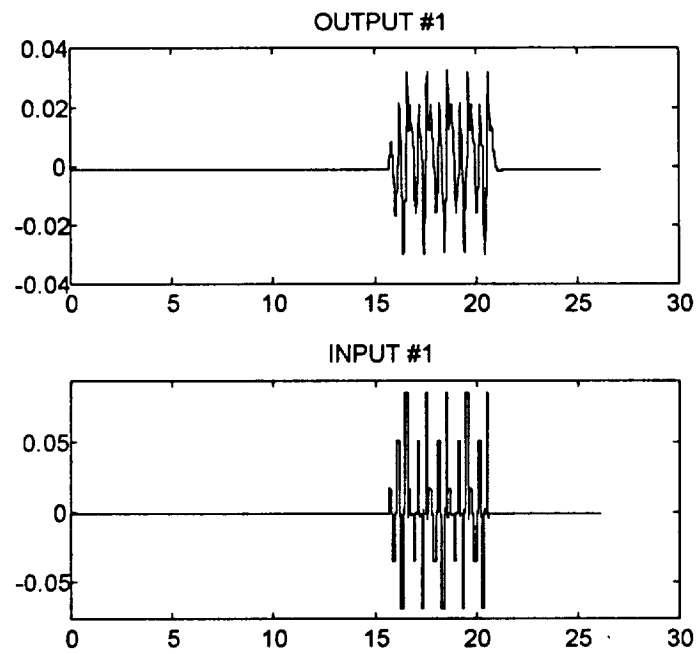
Figure A20. Elbow Pitch Bipolar Ramping Pulse Data.

Estimated Disturbance Spectrum
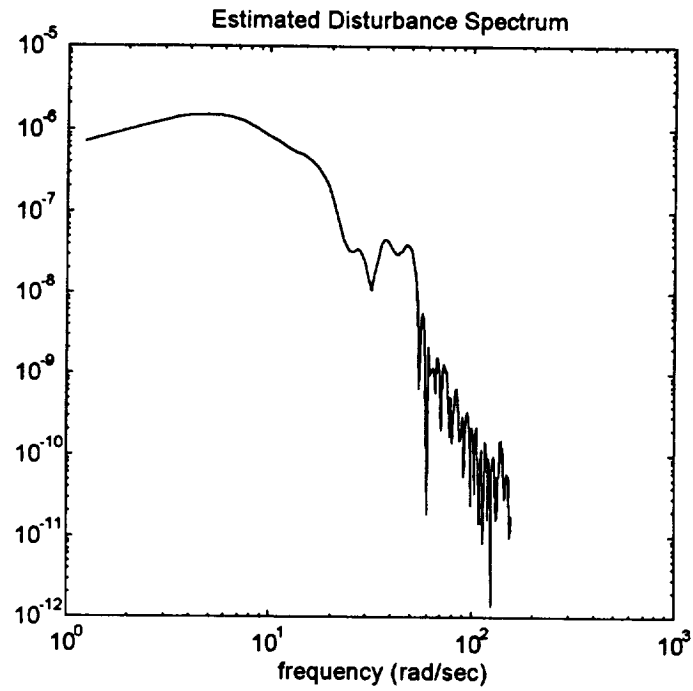
Figure A21. Elbow Pitch Estimated Disturbance Spectrum.

Estimated Output Spectrum
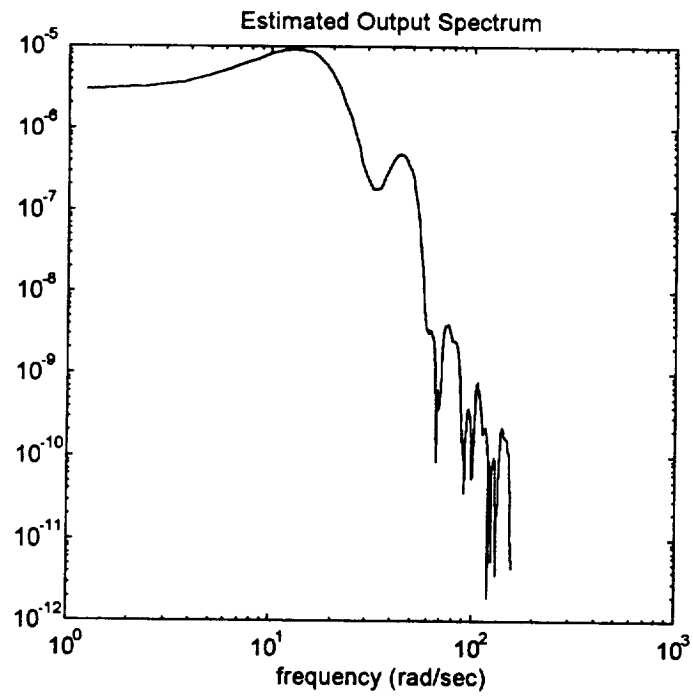
Figure A22. Elbow Pitch Estimated Output Spectrum.
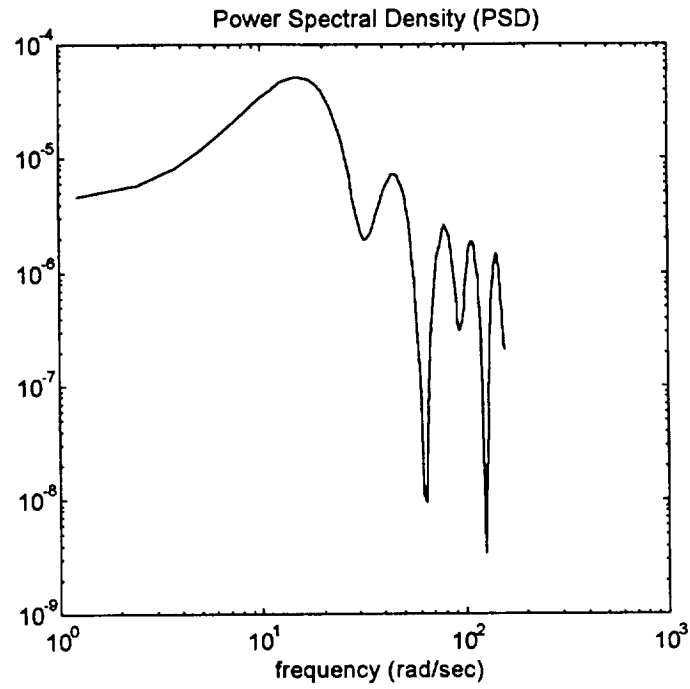
Figure A23. Elbow Pitch Estimated Input Power Spectrum.
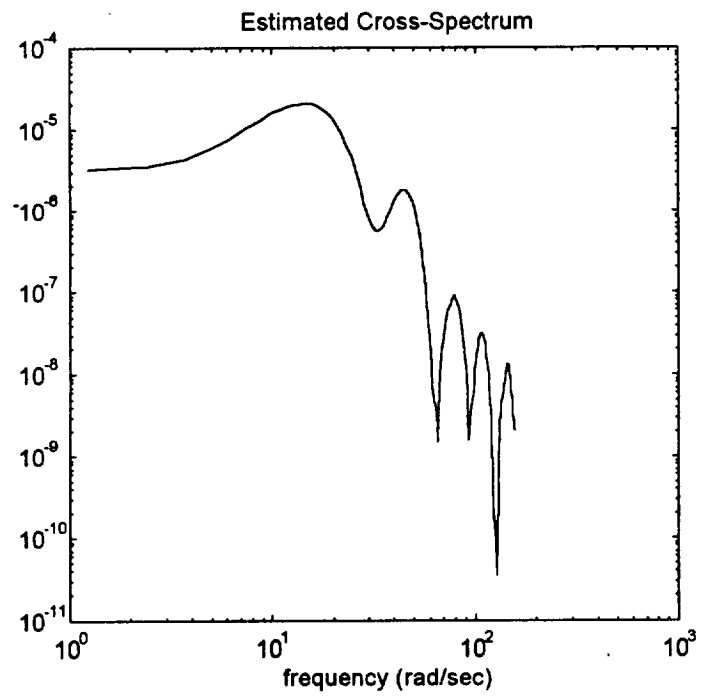
Figure A24. Elbow Pitch Estimated Cross-Spectrum.
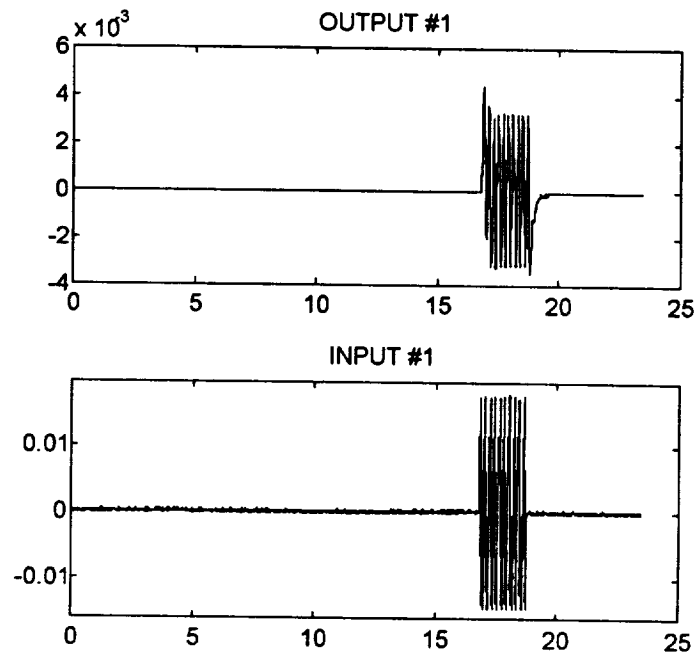
Figure A25. Elbow Pitch Sum of Sinusoids I/O Data.
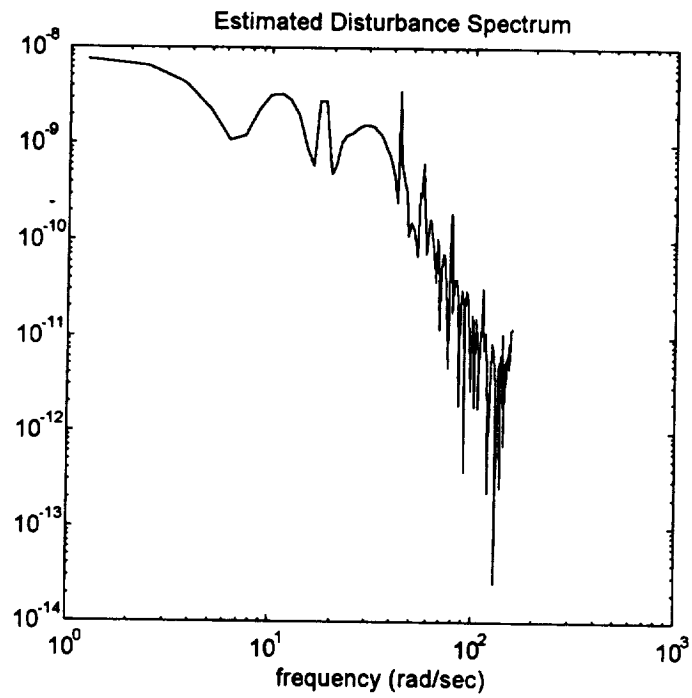
Figure A26. Elbow Pitch Estimated Disturbance Spectrum.
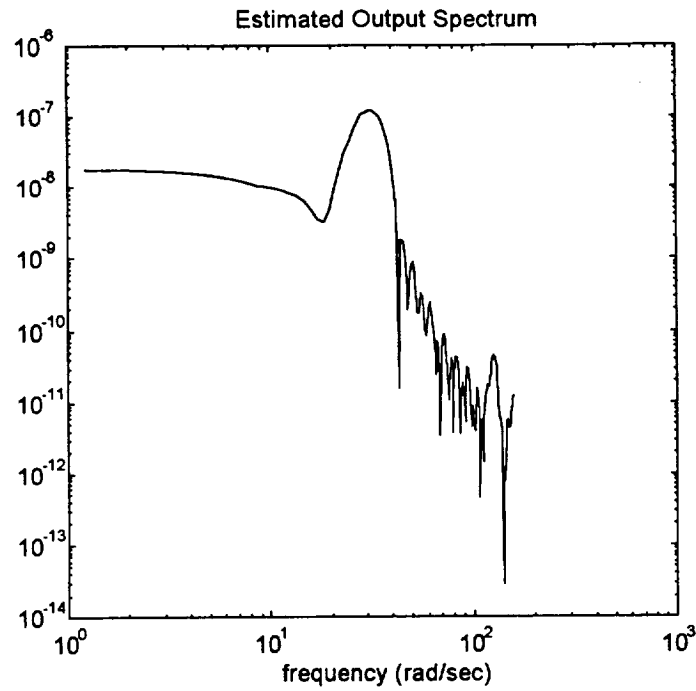
Figure A27. Elbow Pitch Estimated Output Spectrum.
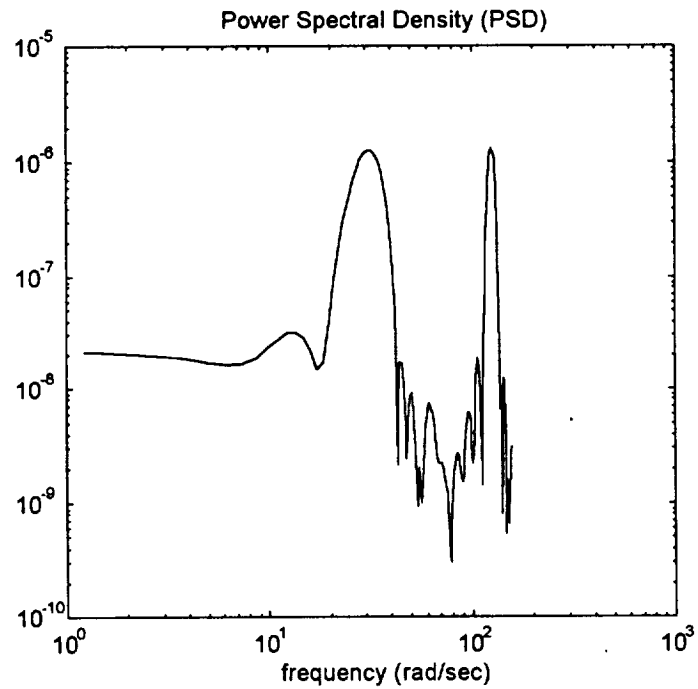
Figure A28. Elbow Pitch Estimated Power Spectrum.

99

Estimated Cross-Spectrum
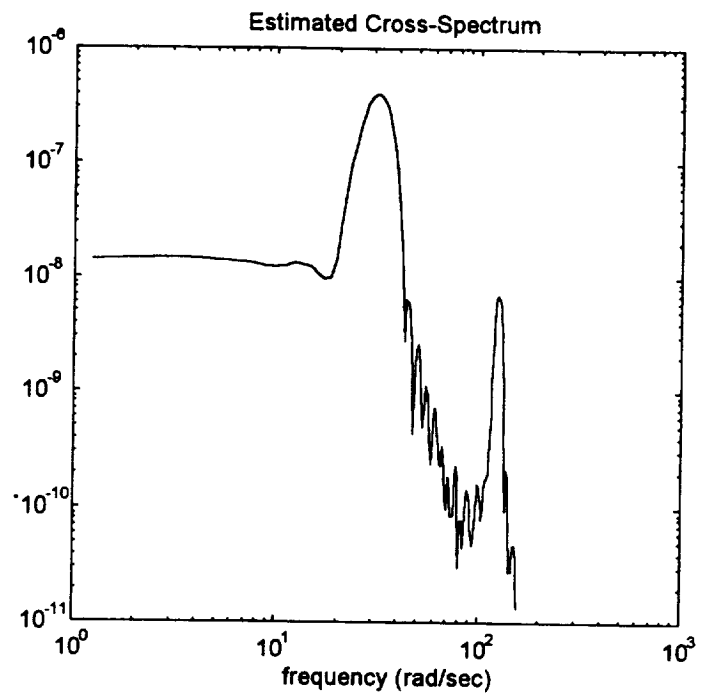
Figure A29. Elbow Pitch Estimated Cross-Spectrum.

A.2 Classical Parametric Plots
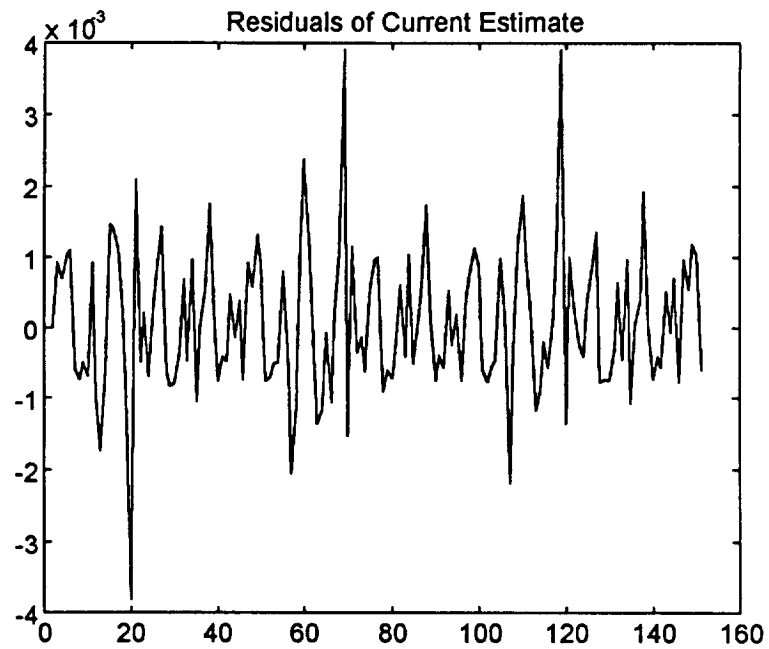
Figure A30. Shoulder Pitch ARMAX Residuals.
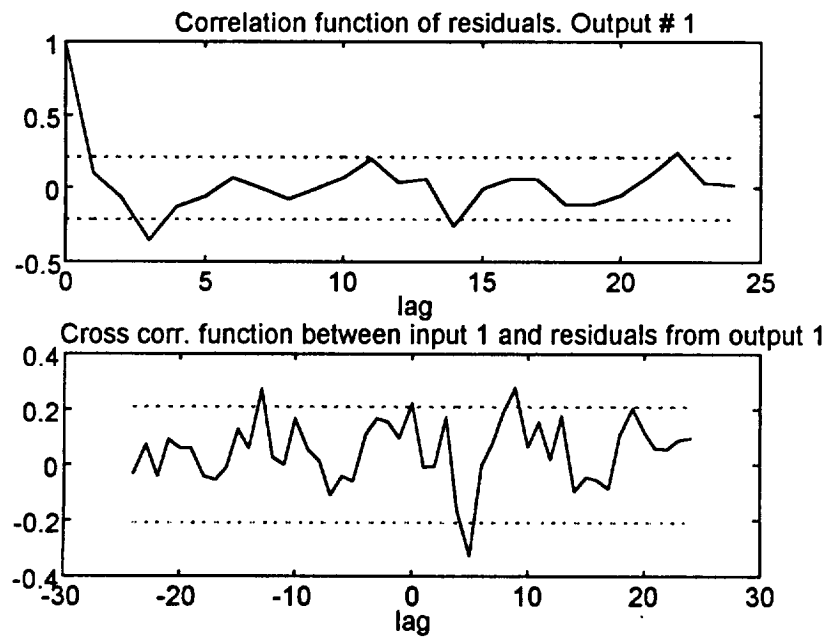
Figure A31. Shoulder Pitch ARMAX Residual Whiteness and Independence.
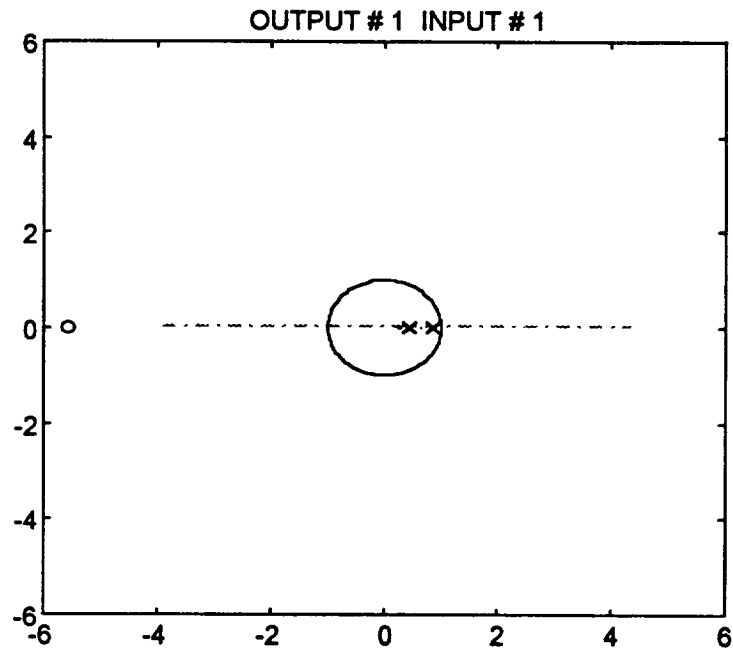
Figure A32. Shoulder Pitch ARMAX Pole-Zero Plot.
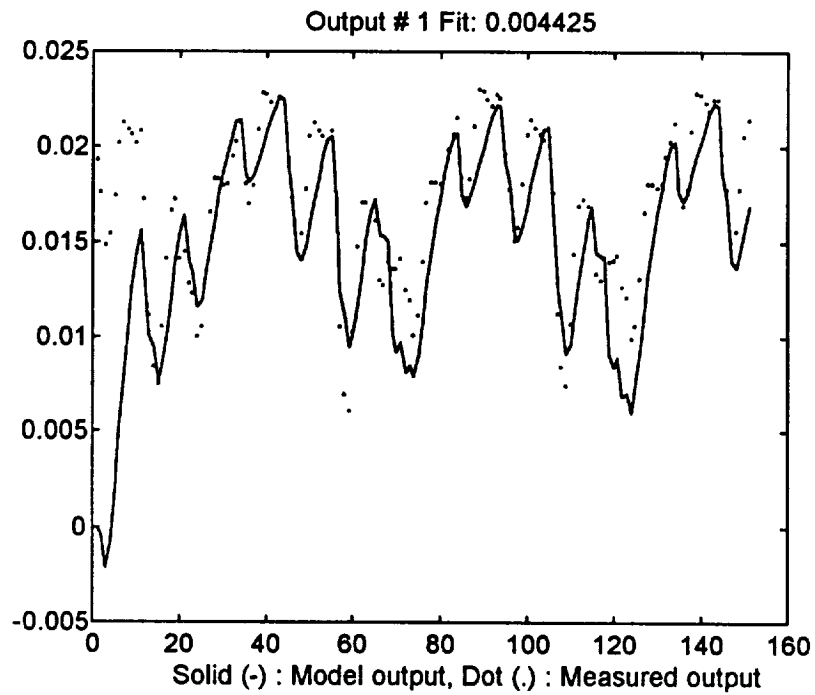
Figure A33. Shoulder Pitch ARMAX Output Comparison.

Output # 1 Fit: 0.002641

Solid (-) : Model output, Dot (.) : Measured output
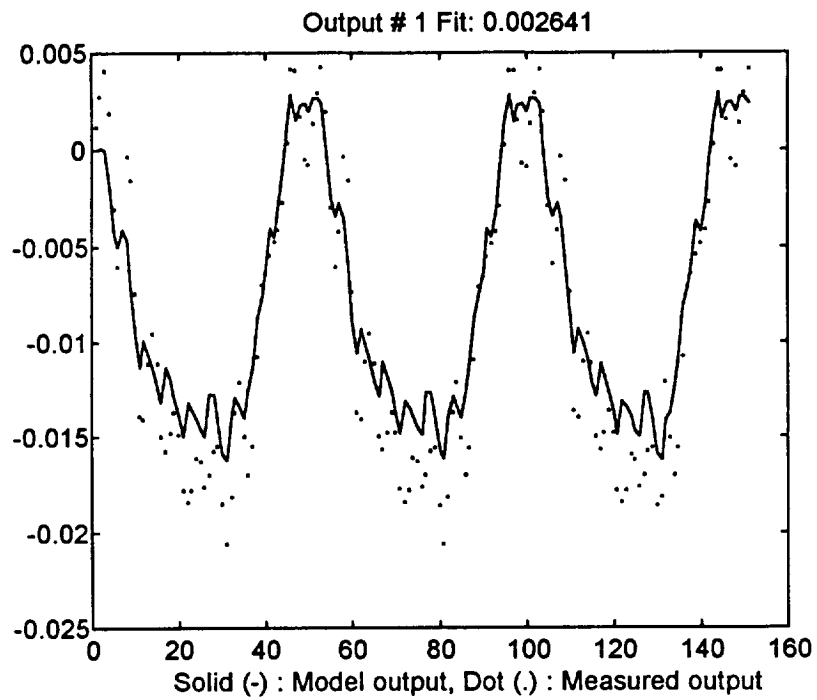
Figure A34. Shoulder Pitch ARMAX Cross-Validation.

Residuals of Current Estimate
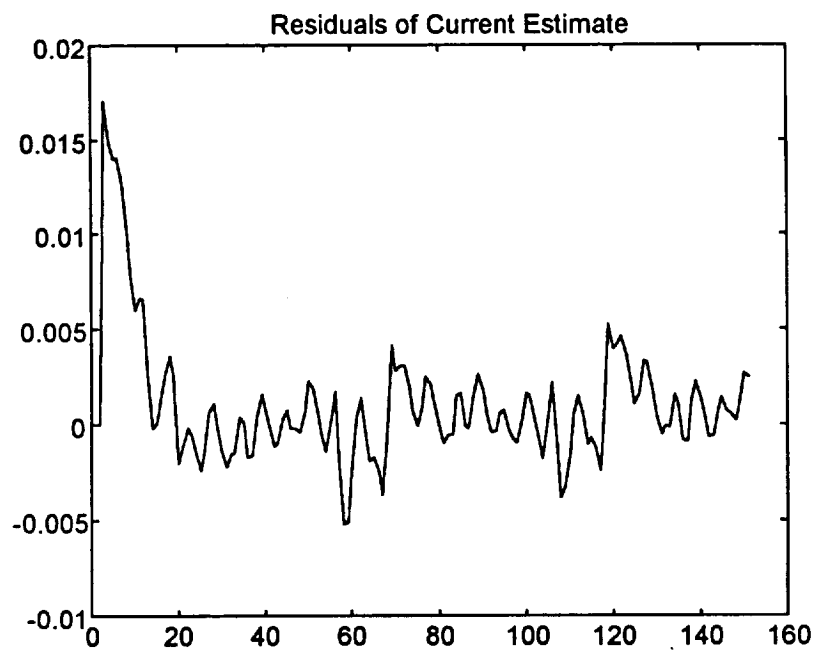
Figure A35. Shoulder Pitch OE Residuals.
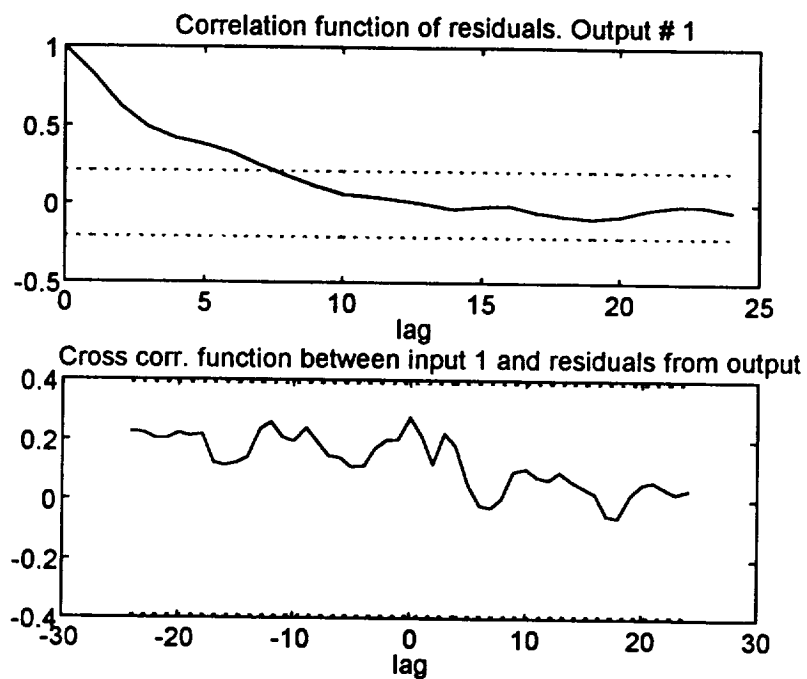
Figure A36. Shoulder Pitch OE Residual Whiteness and Independence.
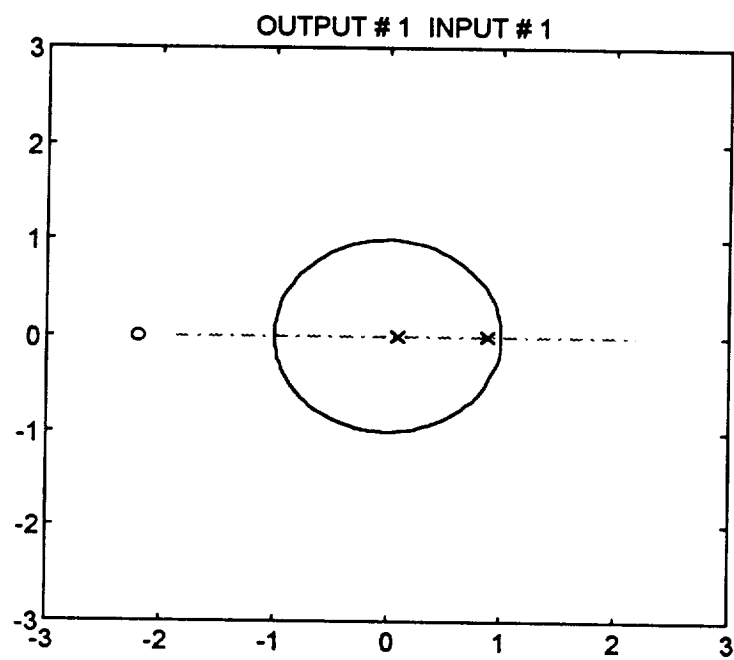
Figure A37. Shoulder Pitch OE Pole-Zero Plot.
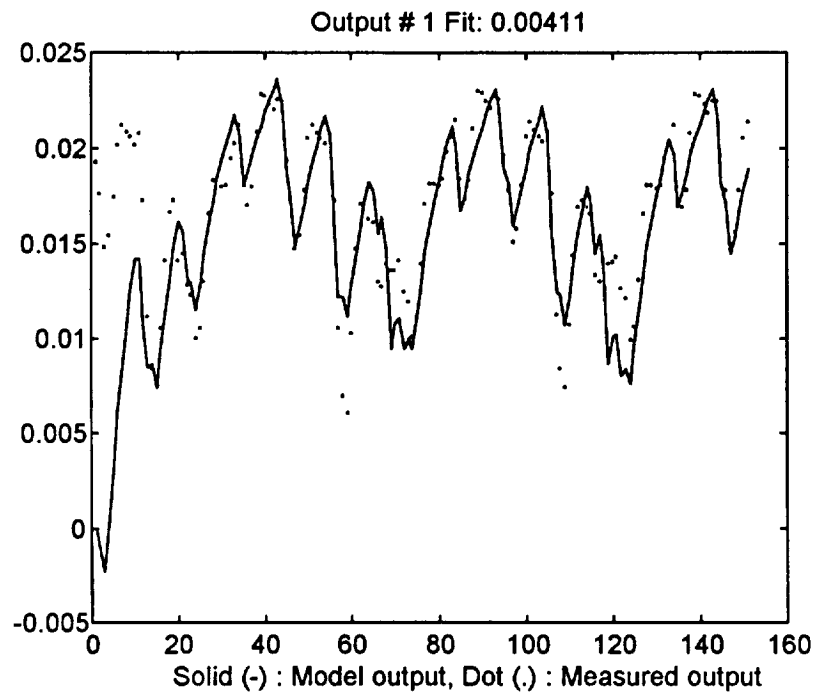
Figure A38. Shoulder Pitch OE Output Comparison.
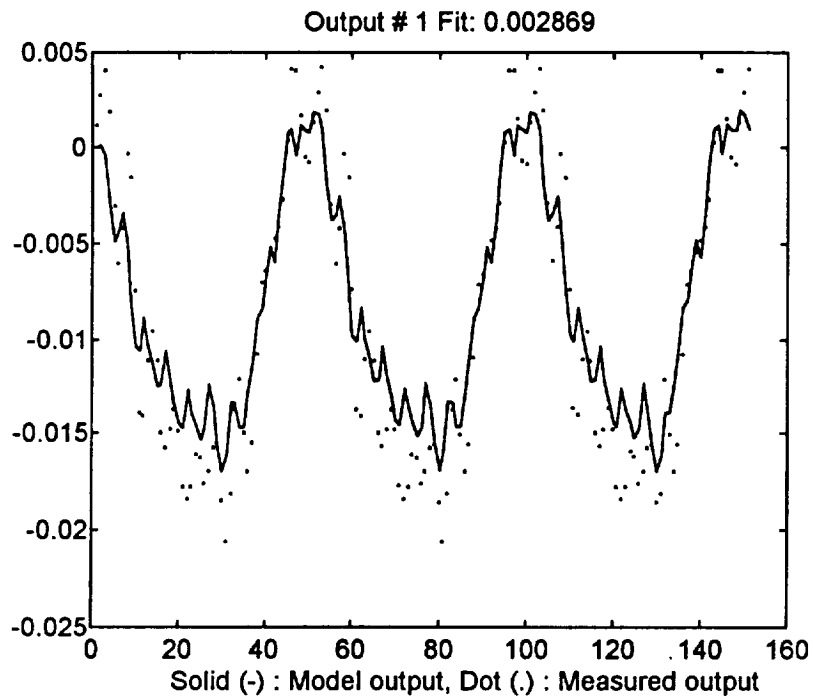
Figure A39. Shoulder Pitch OE Cross-Validation.

105
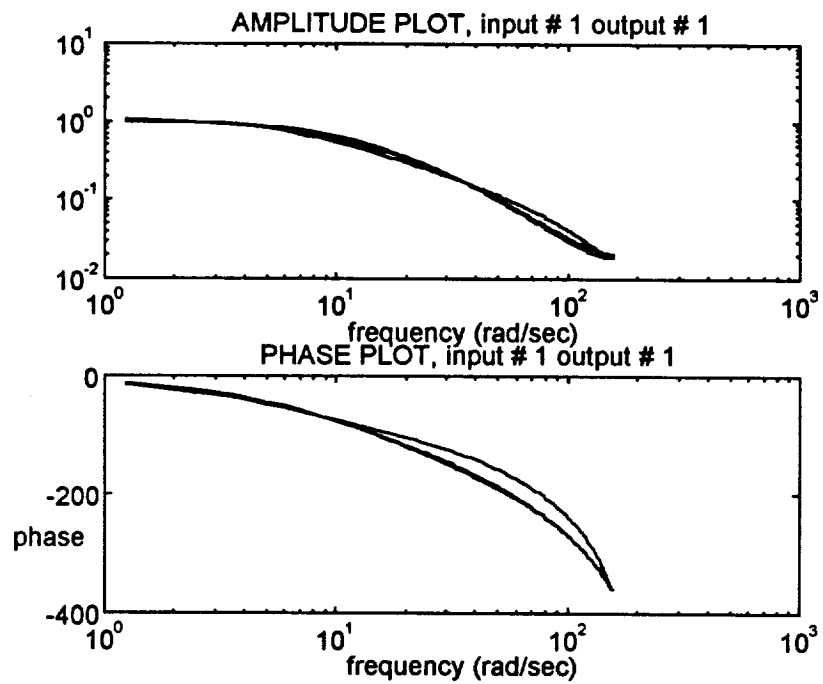
Figure A40. Bode Plots of the ARMAX, ARX, and OE Estimates.
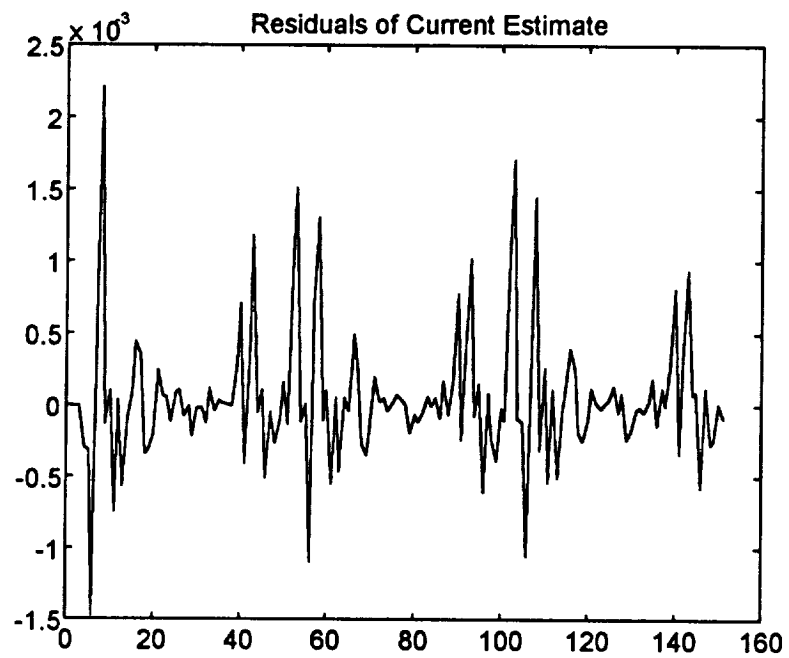
Figure A41. Elbow Pitch ARMAX Residuals.
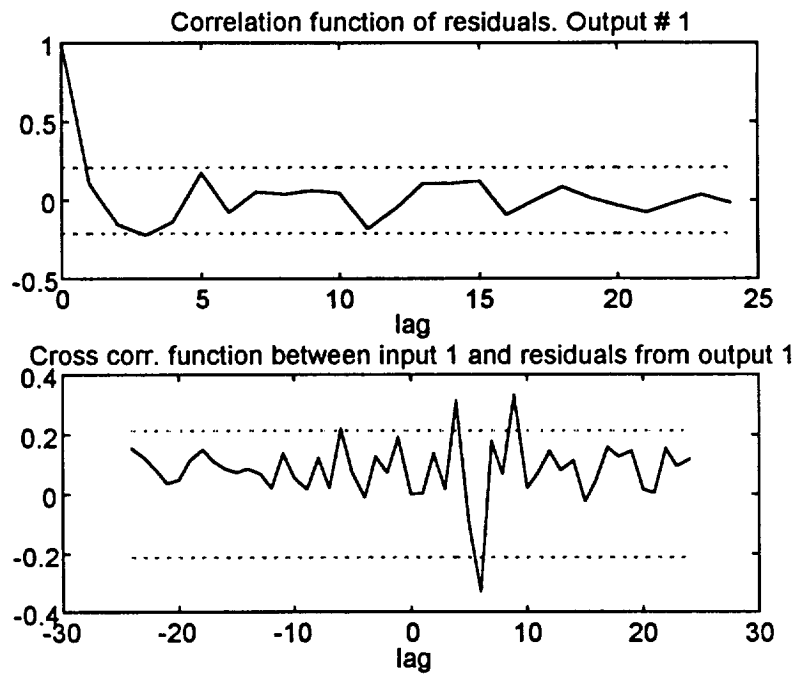
Figure A42. Elbow Pitch ARMAX Residual Whiteness and Independence.
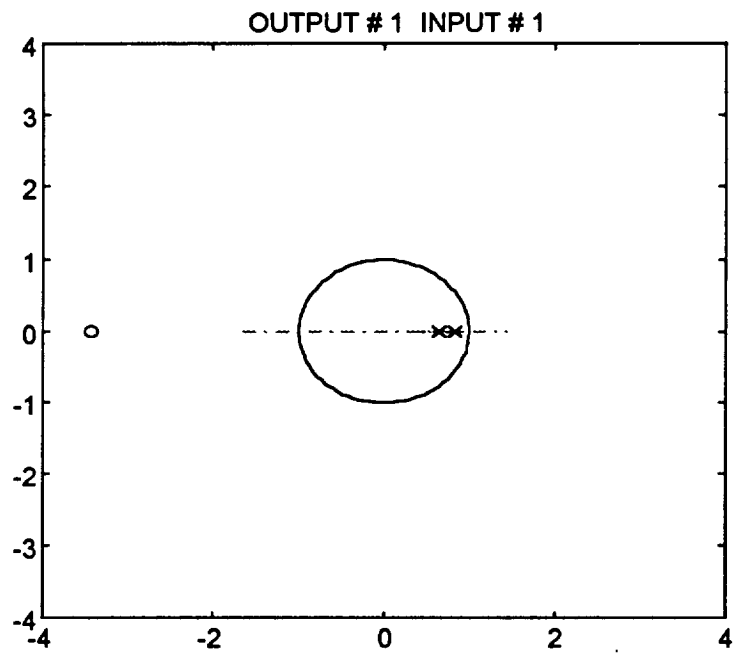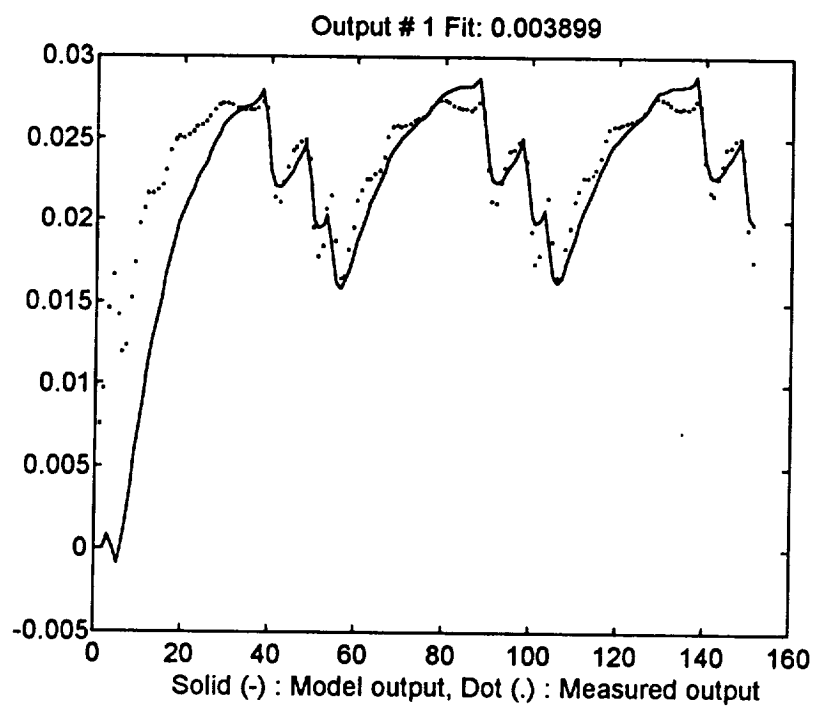

Figure A43. Elbow Pitch ARMAX Pole-Zero Plot.
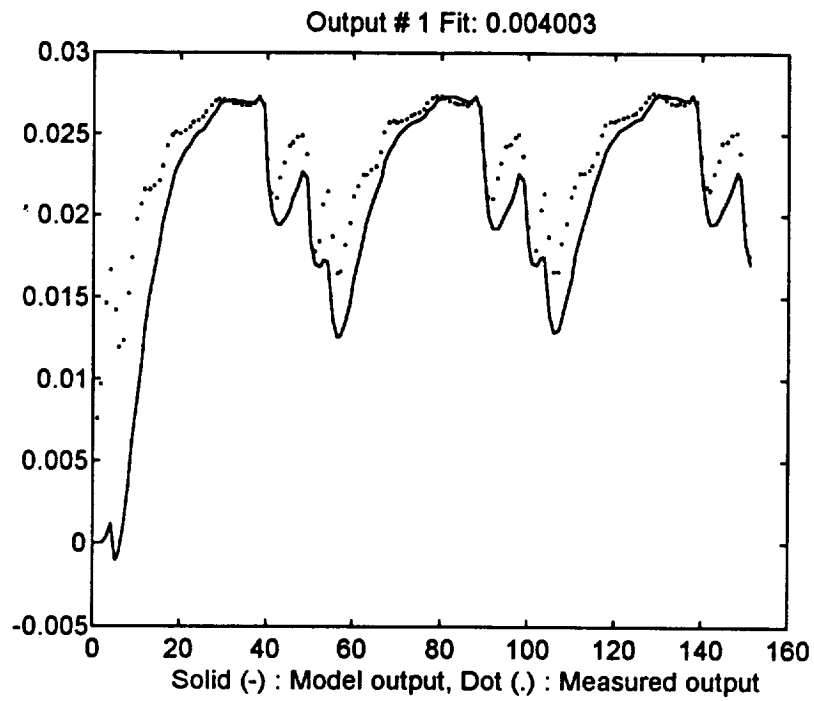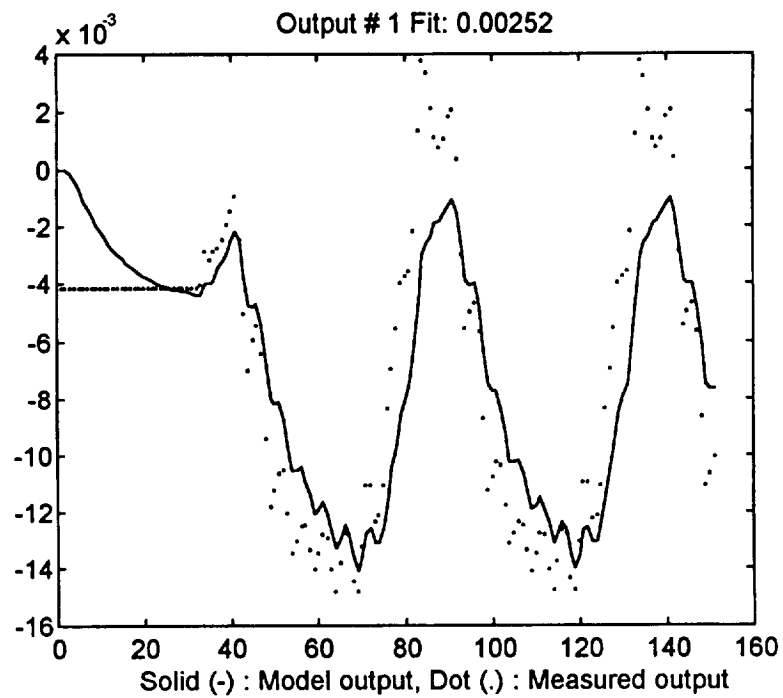
Figure A44. Elbow Pitch ARMAX Output Comparison.
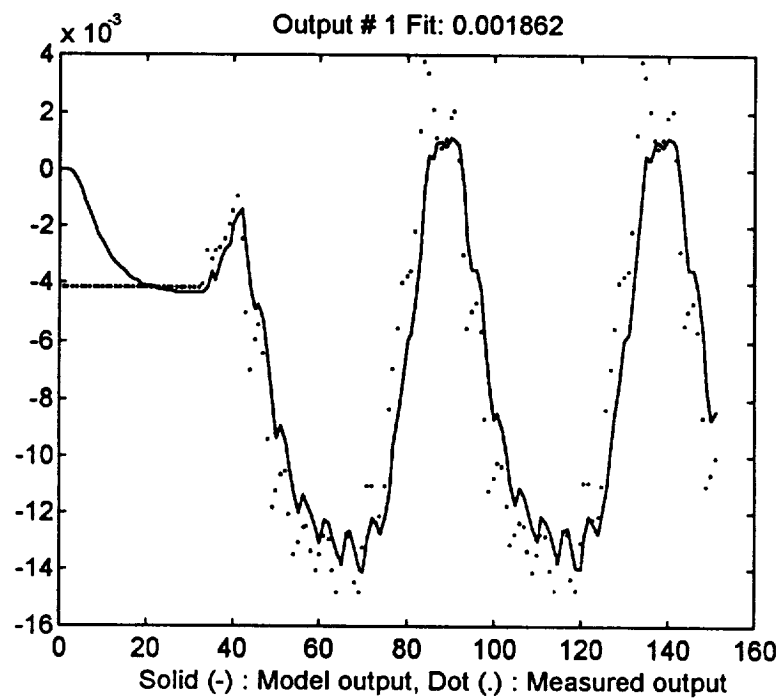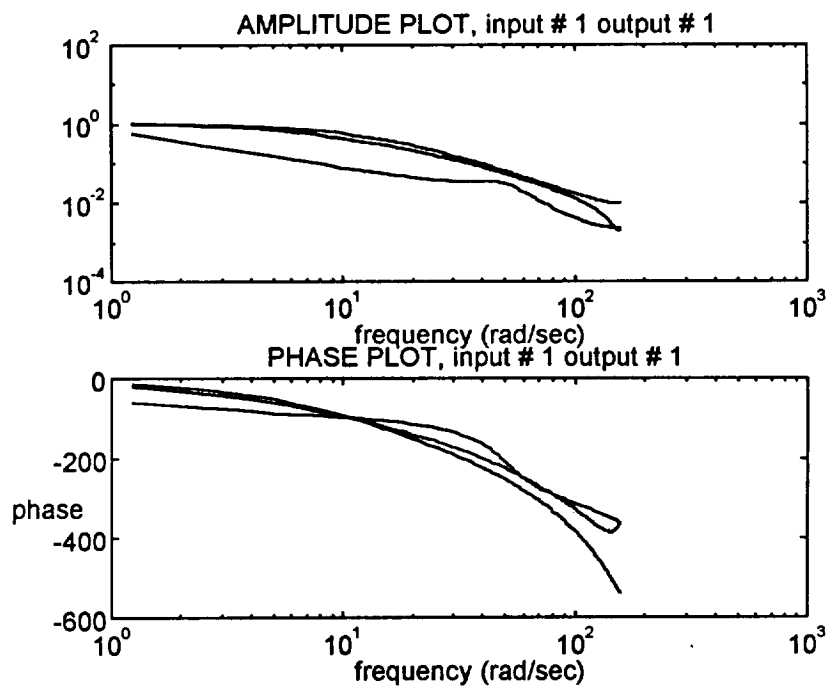

Figure A45. Elbow Pitch ARMAX Cross-Validation.
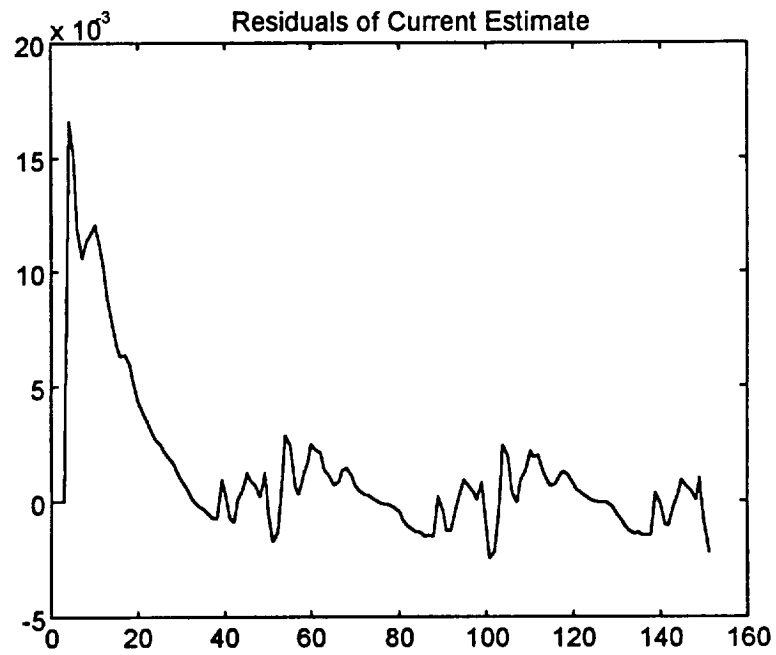
Figure A46. Elbow Pitch OE Residuals.
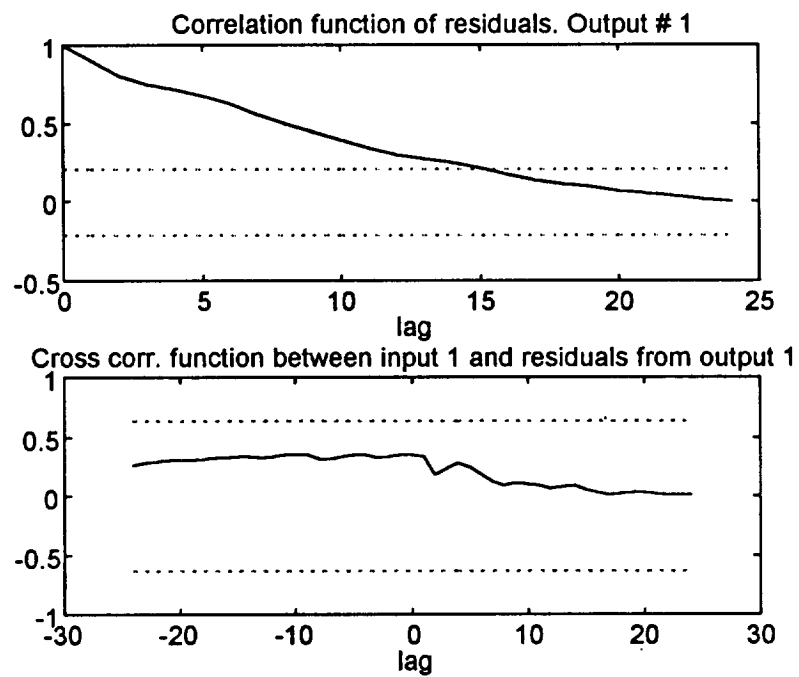
Figure A47. Elbow Pitch OE Residual Whiteness and Independence.
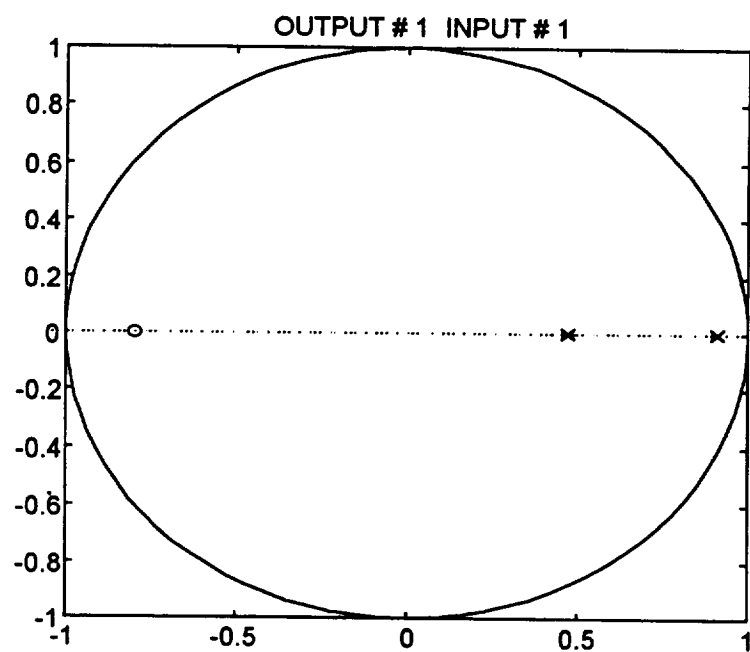
Figure A48. Elbow Pitch OE Pole-Zero Plot.

Solid (-) : Model output, Dot (.) : Measured output

Figure A49. Elbow Pitch OE Output Comparison.

110

Figure A50. Elbow Pitch OE Cross-Validation.

Figure A51. Bode Plots of the ARMAX, ARX, and OE Estimates.
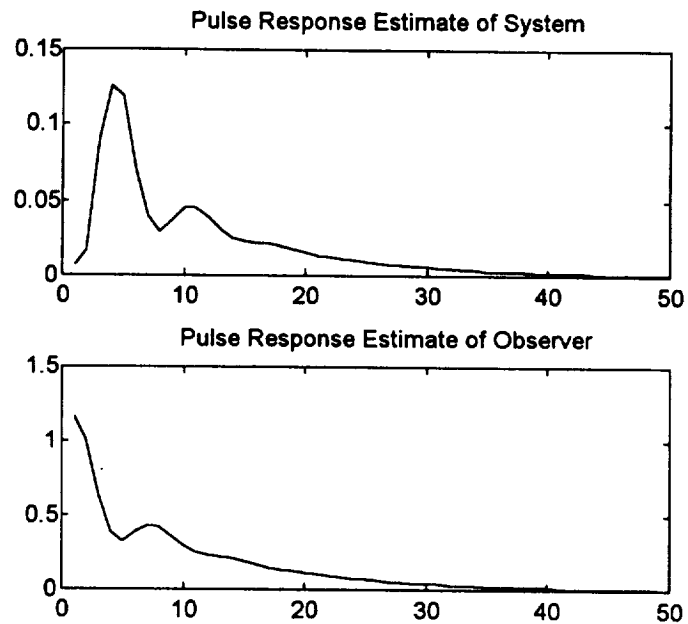
A.3   OKID Parametric Plots

Pulse Response Estimate of System

Pulse Response Estimate of Observer

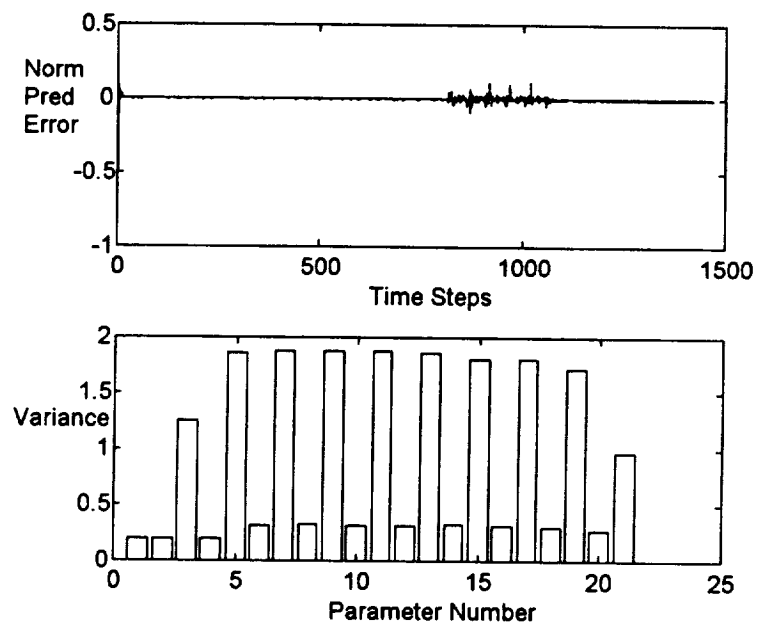Figure A52. Shoulder Pitch System and Observer Markov Parameters.

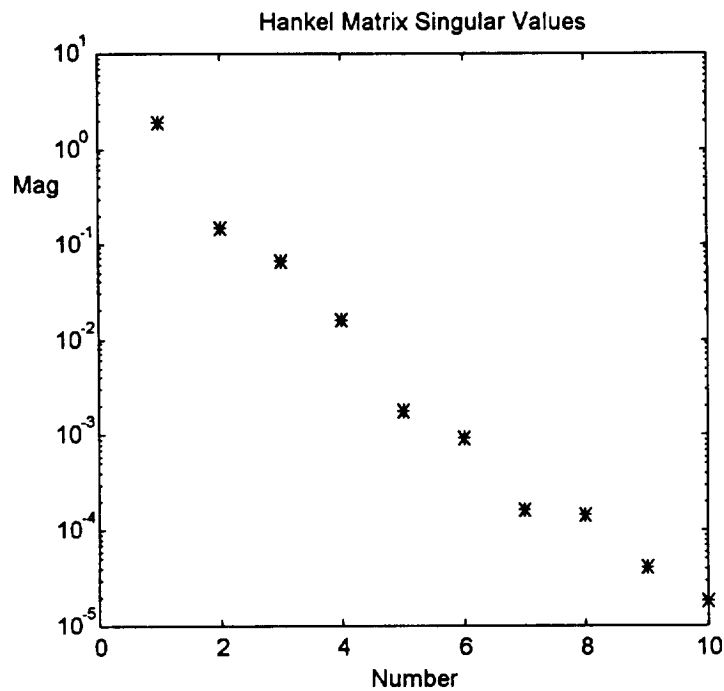Figure A53. Shoulder Pitch Output Prediction Errors.
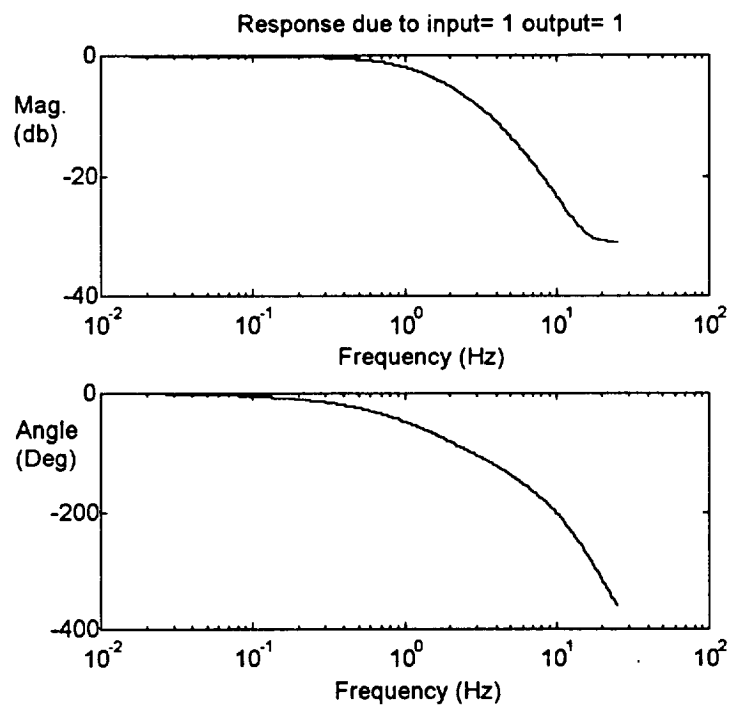
Figure A54. Shoulder Pitch Hankel Matrix.

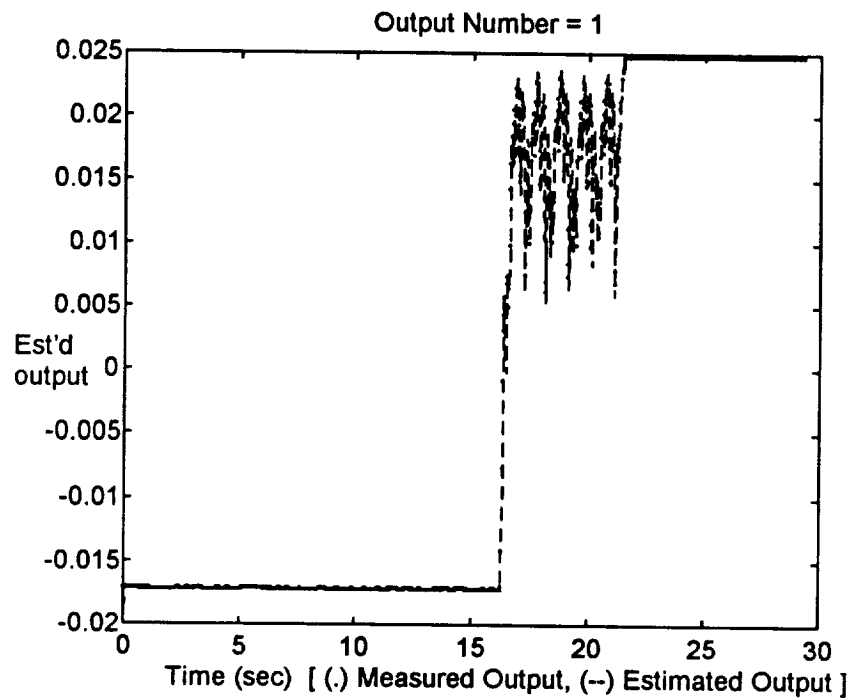Figure A55. Shoulder Pitch Bode Plots of State-Space Estimate.

113

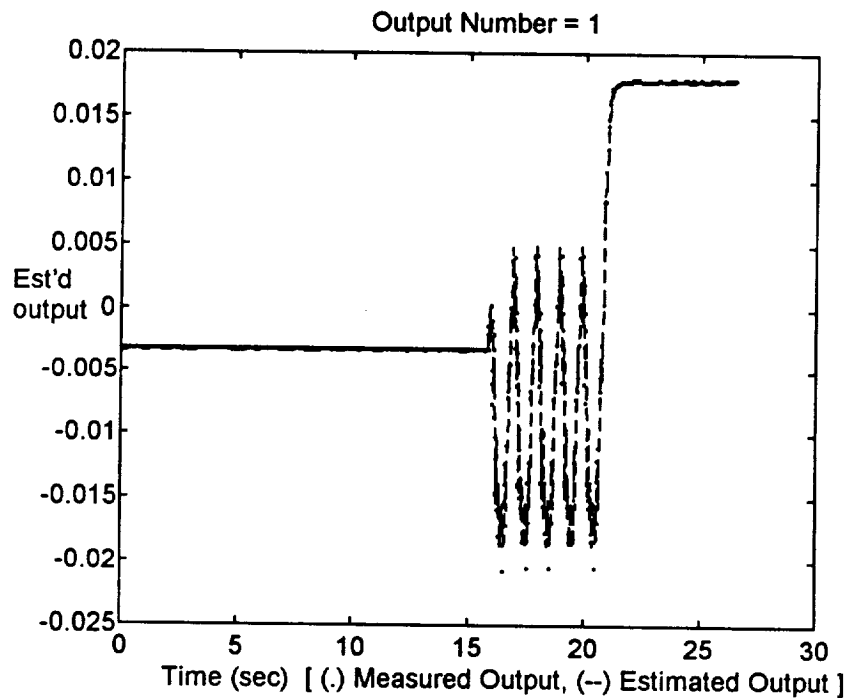Figure A56. Shoulder Pitch Predicted Versus Measured Output.

Figure A57. Shoulder Pitch Chirp Cross-Validation.

Pulse Response Estimate of System

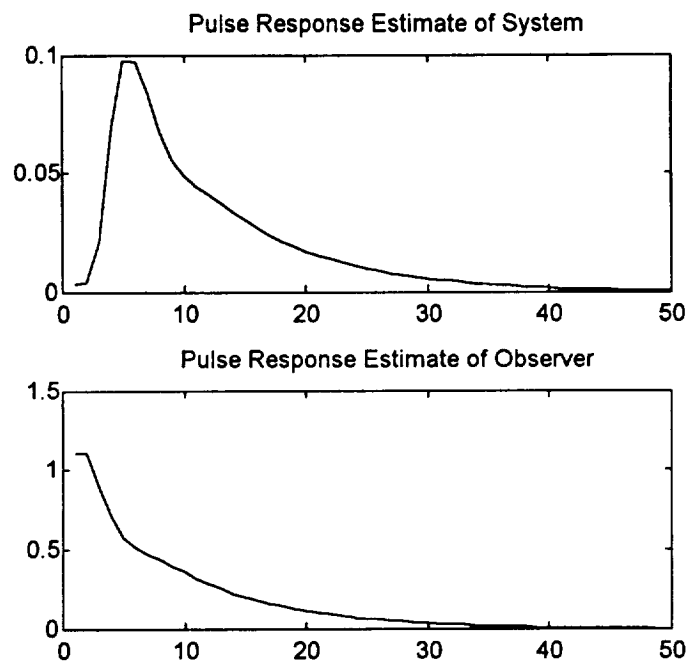## Pulse Response Estimate of Observer

Figure A58. Elbow Pitch System and Observer Markov Parameters.
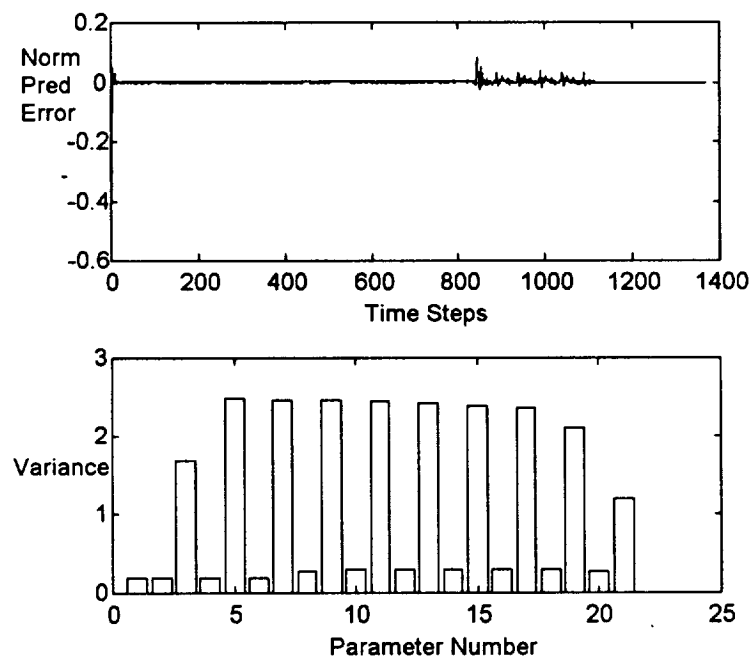

Figure A59. Elbow Pitch Output Prediction Errors.
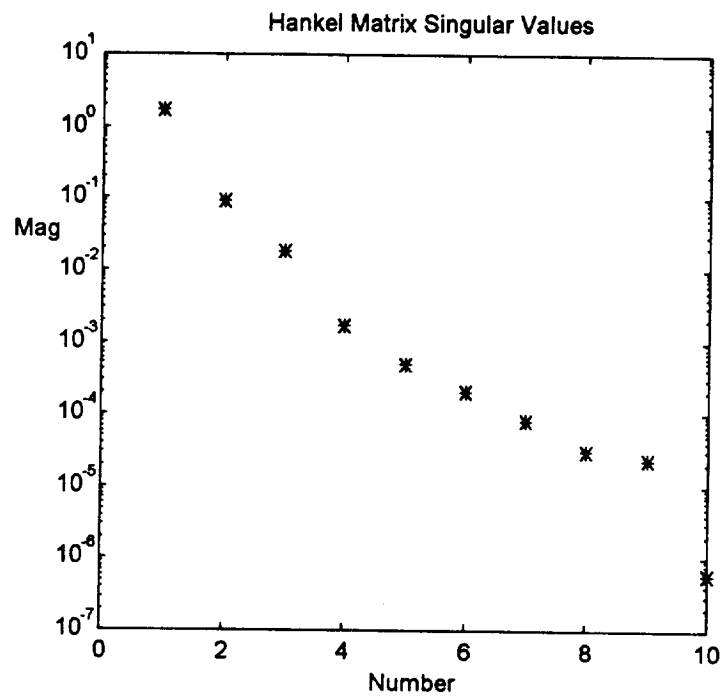
115
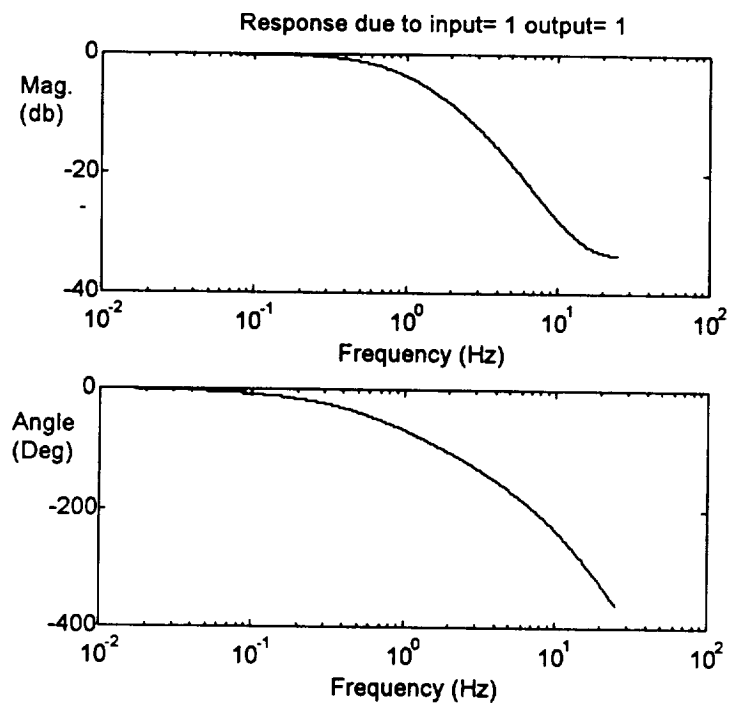
Figure A60. Elbow Pitch Hankel Matrix.

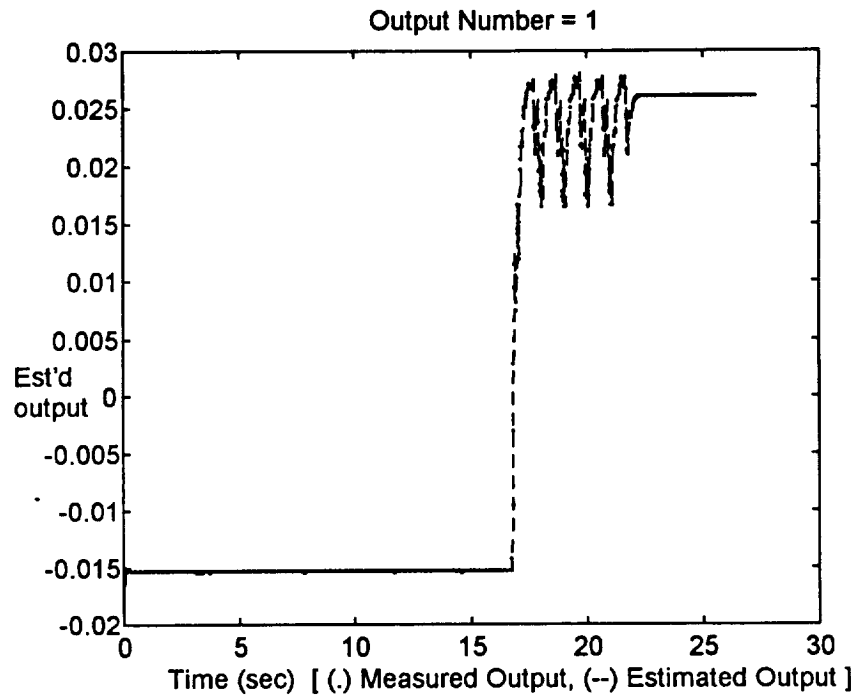Figure A61. Elbow Pitch Bode Plots of State-Space Estimate.

116

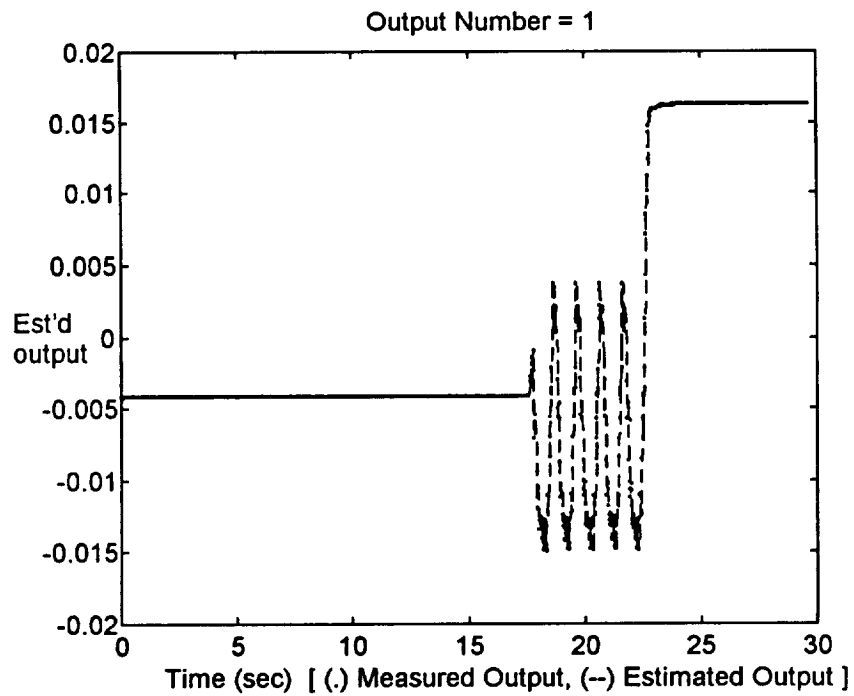Figure A62. Elbow Pitch Predicted Versus Measured Output.

Figure A63. Elbow Pitch Chirp Cross-Validation.

REPORT DOCUMENTATION PAGE

Public reporting burden for this collection of information is estimated to average 1 hour per response, including the time for reviewing instructions, searching existing data sources, gathering and maintaining the data needed, and completing and reviewing the collection of information. Send comments regarding this burden estimate or any other aspect of this collection of information, including suggestions for reducing this burden, to Washington Headquarters Services, Directorate for Information Operations and Reports, 1215 Jefferson Davis Highway, Suite 1204, Arlington, VA 22202-4302, and to the Office of Management and Budget, Paperwork Reduction Project (0704-0188), Washington, DC 20503.

1. AGENCY USE ONLY (Leave blank)	2. REPORT DATE	3. REPORT TYPE AND DATES COVERED
	September 1996	Technical Memorandum

4. TITLE AND SUBTITLE

Comparison of System Identification Techniques for the Hydraulic Manipulator Test Bed (HMTB)

5. FUNDING NUMBERS

233-03-03-02

6. AUTHOR(S)

A. Terry Morris

7. PERFORMING ORGANIZATION NAME(S) AND ADDRESS(ES)

NASA Langley Research Center
Hampton, VA 23681-0001

8. PERFORMING ORGANIZATION REPORT NUMBER

9. SPONSORING / MONITORING AGENCY NAME(S) AND ADDRESS(ES)

National Aeronautics and Space Administration
Washington, D.C. 20546-0001

10. SPONSORING / MONITORING AGENCY REPORT NUMBER

NASA TM-110279

11. SUPPLEMENTARY NOTES

12a. DISTRIBUTION / AVAILABILITY STATEMENT

Unclassified-Unlimited
Subject Category 63

12b. DISTRIBUTION CODE

13. ABSTRACT (Maximum 200 words)

In this thesis linear, dynamic, multivariable state-space models for three joints of the ground-based Hydraulic Manipulator Test Bed (HMTB) are identified. HMTB, housed at the NASA Langley Research Center, is a ground-based version of the Dexterous Orbital Servicing System (DOSS), a representative space station manipulator. The dynamic models of the HMTB manipulator will first be estimated by applying nonparametric identification methods to determine each joint's response characteristics using various input excitations. These excitations include sum of sinusoids, pseudorandom binary sequences (PRBS), bipolar ramping pulses, and chirp input signals. Next, two different parametric system identification techniques will be applied to identify the best dynamical description of the joints. The manipulator is localized about a representative space station orbital replacement unit (ORU) task allowing the use of linear system identification methods. Comparisons, observations, and results of both parametric system identification techniques are discussed.

The thesis concludes by proposing a model reference control system to aid in astronaut ground tests. This approach would allow the identified models to mimic on-orbit dynamic characteristics of the actual flight manipulator thus providing astronauts with realistic on-orbit responses to perform space station tasks in a ground-based environment.

14. SUBJECT TERMS

Hydraulic Manipulator Test Bed (HMTB), Dexterous Orbital Servicing System (DOSS), system identification, parameter estimation, model validation, space-station, manipulator, robotics, state-space realization, ground-based testbed

15. NUMBER OF PAGES

127

16. PRICE CODE

A07

17. SECURITY CLASSIFICATION OF REPORT	18. SECURITY CLASSIFICATION OF THIS PAGE	19. SECURITY CLASSIFICATION OF ABSTRACT	20. LIMITATION OF ABSTRACT
Unclassified	Unclassified		